The MOLLER Experiment
Measurement **O**f a **L**epton **L**epton **E**lectroweak **R**eaction

An Ultra-precise Measurement of the Weak Mixing Angle using Møller Scattering

An MIE proposal to
The United States Department of Energy

The MOLLER Collaboration

September 12, 2011

The MOLLER Collaboration

J. Benesch, P. Brindza, R.D. Carlini, J-P. Chen, E. Chudakov, S. Covrig, C.W. de Jager, A. Deur, D. Gaskell, J. Gomez, D.W. Higinbotham, J. LeRose, D. Mack, R. Michaels, B. Moffit, S. Nanda, G.R. Smith, P. Solvignon, R. Suleiman, B. Wojtsekhowski
Jefferson Lab

H. Baghdasaryan, G. Cates, D. Crabb, D. Day, M.M. Dalton, C. Hanretty, N. Kalantarians, N. Liyanage, V.V. Nelyubin, B. Norum, K. Paschke, M. Shabestari, J. Singh, A. Tobias, K. Wang, X. Zheng
University of Virginia

P. Decowski, S. Johnston, K.S. Kumar [Contact*], J. Mammei, L. Mercado, R. Miskimen, S. Riordan, J. Wexler
University of Massachusetts, Amherst

J. Birchall, M.T.W. Gericke, W.R. Falk, L. Lee, R. Mahurin, S.A. Page, W.T.H. van Oers, V. Tvaskis
University of Manitoba

V. Bellini, A. Giusa, F. Mammoliti, G. Russo, M.L. Sperduto, C.M. Sutera
INFN Sezione di Catania and Universita' di Catania

D.S. Armstrong, T.D. Averett, W. Deconinck, J. Katich, J.P. Leckey
College of William & Mary

K. Grimm, K. Johnston, N. Simicevic, S. Wells
Louisiana Tech University

L. El Fassi, R. Gilman, G. Kumbartzki, R. Ransome,
Rutgers University

J. Arrington, K. Hafidi, P.E. Reimer, J. Singh
Argonne National Lab

P. Cole, D. Dale, T.A. Forest, D. McNulty
Idaho State University

K. Aulenbacher, S. Baunack, F. Maas, V. Tioukine
Johannes Gutenberg Universitaet Mainz

W. Duvall, A. Lee, M. Pitt
Virginia Polytechnic Institute and State University

E. Fuchey, F. Itard, C. Muñoz Camacho
LPC Clermont, Université Blaise Pascal

J.H. Lee, P.M. King, J. Roche
Ohio University

E. Cisbani, S. Frullani, F. Garibaldi
INFN Gruppo Collegato Sanita' and Istituto Superiore di Sanita'

R. De Leo, L. Lagamba, S. Marrone
INFN, Sezione di Bari and University di Bari

F. Meddi, G.M. Urciuoli
Dipartimento di Fisica dell'Universita' la Sapienza and INFN Sezione di Roma

R. Holmes, P. Souder
Syracuse University

G. Franklin, B. Quinn
Carnegie Mellon University

C.A. Davis, W.D. Ramsay
TRIUMF

J.A. Dunne, D. Dutta

Mississippi State University

A.T. Katramatou, G. G. Petratos
Kent State University

A. Ahmidouch, S. Danagoulian
North Carolina A&T State University

S. Kowalski, V. Sulkosky
Massachusetts Institute of Technology

J. Napolitano, P. Stoler
Rensselaer Polytechnic Institute

O. Glamazdin, R. Pomatsalyuk
NSC Kharkov Institute of Physics and Technology

J. Erler
Universidad Autónoma de México

M.J. Ramsey-Musolf
University of Wisconsin, Madison

Yu.G. Kolomensky
University of California, Berkeley

K. A. Aniol
California State U.(Los Angeles)

J.W. Martin
University of Winnipeg

E. Korkmaz
University of Northern British Columbia

T. Holmstrom
Longwood University

S.F. Pate
New Mexico State University

G. Ron
Hebrew University of Jerusalem

D.T. Spayde
Hendrix College

P. Markowitz
Florida International University

F.R. Wesselmann
Xavier University of Louisiana

C. Hyde
Old Dominion University

F. Benmokhtar
Christopher Newport University

E. Schulte
Temple University

M. Capogni
Istituto Nazionale di Metrologia delle Radiazioni Ionizzanti ENEA and INFN Gruppo Collegato Sanita'

R. Perrino
INFN Sezione di Lecce

[*]kkumar@physics.umass.edu

Executive Summary

We present the physics case and experimental design for the MOLLER project, in which we propose to measure the parity-violating asymmetry A_{PV} in polarized electron-electron (Møller) scattering. In the Standard Model, A_{PV} is due to the interference between the electromagnetic amplitude and the weak neutral current amplitude, the latter being mediated by the Z^0 boson. A_{PV} is predicted to be ≈ 35 parts per billion (ppb) at our kinematics. Our goal is to measure A_{PV} to a precision of 0.73 ppb. The result would yield a measurement of the weak charge of the electron Q^e_W to a fractional accuracy of 2.3% at an average Q^2 of 0.0056 GeV^2.

The measurement is sensitive to the interference of the electromagnetic amplitude with new neutral current amplitudes as weak as $\sim\ 10^{-3} \cdot G_F$ from as yet undiscovered high energy dynamics. Such a level of sensitivity is unlikely to be matched by any experiment measuring a flavor- and CP-conserving process over the next decade, and results in a unique window to new physics at the multi-TeV scale in a manner complementary to direct searches at high energy colliders. Some examples of physics beyond the Standard Model to which our measurement extends sensitivity well beyond recent and ongoing low energy measurements include new Z' bosons, electron compositeness, supersymmetry and doubly charged scalars.

In the Standard Model, the Q^e_W measurement yields a determination of the weak mixing angle $\sin^2\theta_W$ with an uncertainty of $\pm 0.00026(\mathrm{stat}) \pm 0.00013(\mathrm{syst})$, similar to the accuracy of the single best such determination from high energy colliders. Thus, our result could potentially influence the central value of this fundamental electroweak parameter, a critical input to deciphering signals of any physics beyond the Standard Model that might be observed at the Large Hadron Collider (LHC).

The measurement would be carried out in Hall A at Jefferson Laboratory, where a 11 GeV longitudinally polarized electron beam would be incident on a 1.5 m liquid hydrogen target. Møller electrons (beam electrons scattering off target electrons) in the full range of the azimuth and spanning the polar angular range 5 mrad $< \theta_{lab} <$ 19 mrad, would be separated from background and brought to a ring focus $\sim$ 30 m downstream of the target by a spectrometer system consisting of a pair of toroidal magnet assemblies and precision collimators. The Møller ring would be intercepted by a system of quartz detectors; the resulting Cherenkov light would provide a relative measure of the scattered flux.

Longitudinally polarized electrons are generated via photoemission on a GaAs photocathode by circularly polarized laser light, enabling rapid polarization (helicity) reversal and suppression of spurious systematic effects. A_{PV} would be extracted from the fractional difference in the integrated Cherenkov light response between helicity reversals. Additional systematic suppression to the sub-ppb level would be accomplished by periodically reversing the sign of the physics asymmetry by three independent methods.

Simultaneously with data collection, the fluctuations in the electron beam energy and trajectory and its potential systematic effects on A_{PV} would be precisely monitored, active feedback loops would minimize beam helicity correlations, and detector response to beam fluctuations would be continuously calibrated. Background fractions and their helicity-correlated asymmetries would be measured by dedicated auxiliary detectors. The absolute value of Q^2 would be calibrated periodically using tracking detectors. The longitudinal electron beam polarization would be measured continuously by two independent polarimeter systems.

A strong collaboration with extensive experience in similar experiments is committed to the design, construction and deployment of the apparatus and to data collection and analysis. It is envisioned that construction and assembly will take three years, to be followed by three data collection periods with progressively improved statistical errors and systematic control over a subsequent three to four year period.

Contents

List of Figures **v**

List of Tables **viii**

1 Introduction **1**
- 1.1 Physics Context . . . 1
- 1.2 Definitions and Precision Goal . . . 2

2 Physics Motivation **3**
- 2.1 New Contact Interactions . . . 4
  - 2.1.1 Supersymmetry . . . 4
  - 2.1.2 Z′ Bosons . . . 5
  - 2.1.3 Doubly-Charged Scalars . . . 7
- 2.2 Precision Electroweak Measurements and $\sin^2\theta_W$ . . . 8

3 Experimental Design **10**
- 3.1 Polarized Beam . . . 11
- 3.2 Liquid Hydrogen Target . . . 12
- 3.3 Toroidal Spectrometer . . . 13
  - 3.3.1 Kinematical Considerations . . . 14
  - 3.3.2 Conceptual Design . . . 15
  - 3.3.3 Hybrid Coil Design . . . 16
- 3.4 Detectors . . . 16
  - 3.4.1 Main Integrating Detectors . . . 18
  - 3.4.2 Auxiliary Detectors . . . 20
  - 3.4.3 Tracking Detectors and Scanner . . . 20
- 3.5 Electronics and Data Acquisition . . . 21
  - 3.5.1 Rapid Helicity Flip . . . 21
  - 3.5.2 Integrating Electronics . . . 22
  - 3.5.3 Online Calibrations and Feedbacks . . . 22
- 3.6 Hall A Infrastructure . . . 23

4 Systematic Control **23**
- 4.1 Beam Fluctuations . . . 24
  - 4.1.1 Helicity-Correlated Beam Fluctuations . . . 24
  - 4.1.2 Beam Spot Size Differences . . . 25
- 4.2 Longitudinal Beam Polarization . . . 26
  - 4.2.1 Compton Polarimetry . . . 26
  - 4.2.2 Møller Polarimetry . . . 27
- 4.3 Transverse Beam Polarization . . . 28
- 4.4 Absolute Value of Q^2 . . . 29
- 4.5 Backgrounds . . . 29
  - 4.5.1 Elastic ep Scattering . . . 29
  - 4.5.2 Inelastic ep Scattering . . . 30
  - 4.5.3 Hadrons and Muons . . . 31
  - 4.5.4 Photons and Neutrons . . . 31

5 Beam Time Request and Run Goals 31
5.1 The Three Runs . . . 32
5.1.1 Run I . . . 32
5.1.2 Run II . . . 32
5.1.3 Run III . . . 33
5.2 Special Beam Considerations . . . 33
5.2.1 Transverse Polarization Running . . . 33
5.2.2 Wien Angle “Tweaks” . . . 33
5.2.3 The Double-Wien . . . 33
5.2.4 Beam Energy . . . 34

6 Collaboration 34
6.1 Subsystems . . . 34
6.2 Governance . . . 35

7 Research and Development Topics 35
7.1 Polarized Beam . . . 36
7.1.1 Polarized Laser Light . . . 36
7.1.2 Beamline Instrumentation . . . 36
7.1.3 Beam Transport . . . 36
7.2 Target Design . . . 37
7.3 Simulations and Software . . . 37
7.4 Spectrometer Design . . . 37
7.4.1 Toroid Design . . . 38
7.4.2 Collimation and Shielding . . . 38
7.5 Detector Design . . . 38
7.5.1 Quartz and Light Guide . . . 38
7.5.2 Mechanical Assembly . . . 39
7.5.3 Pion Background . . . 39
7.5.4 Tracking Detectors . . . 39
7.6 Polarimetry . . . 39
7.6.1 Compton Polarimetry . . . 39
7.6.2 Møller Polarimetry . . . 40

8 The MOLLER Project 41

9 Conclusions 41

A Polarized Beam 43
A.1 Polarized Electron Source . . . 43
A.2 Operational Experience . . . 43
A.3 Adiabatic Damping . . . 44
A.4 Slow reversals . . . 45
A.5 Requirements for 11 GeV . . . 46
A.5.1 Rapid Helicity Flip . . . 46
A.5.2 Measurement and Control of HCBAs . . . 47
A.5.3 Beam jitter and monitor resolution . . . 48
A.5.4 Position Feedback . . . 50

A.5.5 Beam spot-size asymmetry . . . 52
A.6 Strategy for control of HCBA . . . 52

B Detailed Discussion of the Hydrogen Target 54
B.1 Comparable Targets . . . 54
B.2 Target Parameters . . . 54
B.3 Density Variation . . . 55
B.4 Cell Design . . . 58
B.5 Refrigeration . . . 59
B.6 Qweak Target Experience and Expected MOLLER Performance . . . 60

C Toroidal Spectrometer 64
C.1 Hybrid Toroid Concept . . . 64
C.2 Detailed Description of Coil Design . . . 65
C.2.1 Conductor Layout . . . 65
C.2.2 Suggestions from the Magnet Advisory Committee . . . 66
C.2.3 Summary of Coil Specifications . . . 67
C.3 Simulated Properties of the Spectrometer . . . 68
C.3.1 Properties of the Idealized Hybrid Field . . . 68
C.3.2 Properties of the Actual Conductor Layout . . . 69

D Integrating Detector Considerations 74
D.1 Current-Mode Signal Magnitude . . . 74
D.2 Event-Mode Signal Magnitude . . . 74
D.3 Radiation Hardness . . . 74

E Electronics 76
E.1 The TRIUMF Electronics . . . 76
E.2 Performance . . . 77

F Compton Polarimetry 79
F.1 The Hall A Compton Polarimeter Baseline Upgrade . . . 79
F.2 Upgrades Beyond the Baseline . . . 80
F.2.1 Laser System . . . 81
F.2.2 Alternative Laser System . . . 83
F.2.3 Chicane Magnet Modification . . . 84
F.2.4 Photon Detection . . . 84
F.3 Systematic Uncertainties . . . 85
F.3.1 Sources of Correlated Error . . . 85
F.3.2 Systematic Errors for the Electron Detector . . . 86
F.4 Systematic Errors for the Photon Detector . . . 89
F.5 Summary of Compton Polarimetry . . . 90

G Møller Polarimetry 91
G.1 Møller Scattering . . . 91
G.2 Ways to Higher Accuracy . . . 91
G.3 Atomic Hydrogen Target . . . 93
G.3.1 Hydrogen Atom in Magnetic Field . . . 93
G.3.2 Storage Cell . . . 93

G.3.3 Gas Properties . . . 95
G.3.4 Gas Lifetime in the Cell . . . 95
G.3.5 Unpolarized Contamination . . . 96
G.3.6 Beam Impact on Storage Cell . . . 96
G.3.7 Beam RF Generated Depolarization . . . 96
G.3.8 Contamination by Free Electrons and Ions . . . 97
G.3.9 Application of the Atomic Target to Møller Polarimetry . . . 97
G.4 Møller Polarimeter in Hall C . . . 98

References 102

List of Figures

1 *Feynman diagrams for Møller scattering at tree level (reproduced from Ref. [6])* 2
2 $\gamma - Z$ *mixing diagrams and* W*-loop contribution to the anapole moment (reproduced from Ref. [6])* 3
3 *Relative shifts in the electron and proton weak charges due to SUSY effects. Dots indicate the range of allowed MSSM-loop corrections. The interior of the truncated elliptical regions give possible shifts due to R-parity violating (RPV) SUSY interactions, where (a) and (b) correspond to different assumptions on limits derived from first row CKM unitarity constraints.* 5
4 *90% C.L. exclusion regions for a 1.2 TeV* Z' (E_6 *gauge group) for MOLLER, Qweak and SOLID, assuming they obtain exactly the SM predictions. Also shown is the contour from the E158 result.* 7
5 *90% C.L. exclusion regions for a 1.2 TeV* Z' *from the* E_6 *gauge group for E158, and MOLLER, assuming the MOLLER central value is half-way between the E158 central value and the SM prediction.* 7
6 *Summary of* 1σ *bands from various precision measurements. The red (filled) ellipse is the 90% C.L. contour of all precision electroweak data. The colored regions are excluded by direct colliders searches. The strongest constraint on the width of the purple (dotted) contour* ($Q^2 \ll M_Z^2$ *measurements) is E158, while its shape and location are influenced by NuTeV [23, 24] (deep inelastic* ν*-scattering): large values of* M_H *are favored, similar to the* $A_{FB}(b)$ *band. In contrast,the* $A_{LR}(had)$ *and* M_W *bands favor very low values of* M_H *which are already ruled out by direct searches. The proposed* A_{PV} *measurement would dominate the future width and location of the dotted contour.* 8
7 *Current and proposed weak mixing-angle measurements vs. the energy scale* μ*. The three future measurements are located at appropriate* μ *values but the vertical locations are arbitrary. Note that the PDG value of* ν*-DIS has been adjusted from the published value.* 9
8 *Layout of the target, spectrometer and detectors.* 10
9 *The SLAC E158 target loop is shown; MOLLER proposes to use the same concept. Liquid flows clock-wise in the picture (downstream to upstream). The liquid-gas interface is just below the motor.* 12
10 *A CAD drawing of the SLAC E158 target chamber. The target loop is remotely movable 6 in in the vertical direction. A table containing optics targets can be moved in and out horizontally.* 12
11 Θ_{COM} *vs* E'_{lab} *for* $E_{beam} = 11$ *GeV, and* E'_{lab} *vs* θ_{lab} *are depicted by the two plots on the left. On the right is shown the proposed concept for the primary acceptance collimator, which is able to achieve 100% acceptance with judiciously chosen* ϕ*-sectors.* 14
12 *Projected radial coordinate of scattered Møller electron trajectories. Colors represent* θ_{lab} *(rad). The spectrometer coils (grey) and collimators (black) are overlaid.* 15
13 *Single hybrid coil with actual conductor layout, with 1/10 scale in the z direction.* 15
14 *Transverse distribution of Møller (black) and ep (red) electrons 28.5 m downstream of target* 17
15 *Radial distribution of Møller (black) and ep (red) electrons 28.5 m downstream of target.* . . 17
16 *Layout of the main integrating and tracking detectors. Elastically scattered electrons off target protons (blue) and electrons (green) are also shown.* 18

17 *Plan cutaway view, along with the main elastic Møller (green) and ep (blue) trajectories. The quartz detectors are color coded. The main Møller events predominantly hit the red quartz, while the elastic ep trajectories hit the yellow quartz. The blue and green detectors in between will be important to estimate the inelastic ep background correction; see Sec. 4.5.2. Note the two back-to-back red detectors that will simultaneously measure the flux of the Møller peak.* 18

18 *A perspective view of the integrating detector assembly* 19

19 *Proposed radial segmentation of the scattered electron flux, shown both in linear and log scale. The vertical lines correspond to the radial segmentation of the quartz detectors as shown in Fig. 17. The black, red and green curves are for electrons from Møller, elastic e-p and inelastic e-p scattering.* 30

20 *Band structure of GaAs, showing how circularly polarized laser light produces polarized electrons.* 43

21 *Schematic of the laser transport line that allows for rapid reversal of the electron beam polarization.* 44

22 *Beam position and differences, plotted for all* 27×10^6 *pairs of the HAPPEX-II analysis. Arithmetic means, widths, and centroid uncertainty due to random noise are shown. The systematic correlation to helicity was measured to be consistent with zero within the random beam noise. Gaussian fits are included for reference.* 45

23 *Schematic of the concept of the "Double-Wien" filter, which allows a full "slow" flip of the electron beam polarization with minimal disruption to the front end electron beam optics. The flip is accomplished by adjusting the second solenoid, without changing the settings of the two Wien rotators.* 47

24 *Typical position measurement resolutions from the Qweak experiment for 480 Hz window pairs for "stripline" beam position monitors. The residuals from a comparison of the measured beam position to the projected position from two upstream monitors are shown.* 49

25 *Typical X and Y position and angle difference distributions for 480 Hz window pairs from the Qweak experiment at 160* μ*A beam current. The RMS values from the Gaussian fits are the random beam noise ("jitter") in these parameters.* 50

26 *Typical intensity asymmetry and energy difference distributions for 480 Hz window pairs from the Qweak experiment at 160* μ*A beam current. The RMS values from the Gaussian fits are the random beam noise ("jitter") in these parameters.* 51

27 *Target density fluctuation widths versus helicity flip frequency from recent* Q_{weak} beam studies. 58

28 *E158-type target cell design. Note that the fluid flow (left to right) is opposite the electron beam direction (right to left).* 59

29 *CFD simulations of a E158-type cell in nominal conditions.* 60

30 *Qweak target performance: density fluctuation widths versus beam current from recent* Q_{weak} *measurements. The blue points are measured data. The red curve is a fit to the data. The green curve is another fit, providing a measure of the uncertainties.* 61

31 *CFD study of film boiling at the aluminum windows: window heat flux for three experiments (G0, Qweak and MOLLER). The blue points are the convective part of the heat flux, which is mainly responsible for the film boiling. The red points are the total heat flux. The first (red) data point shows the threshold for film boiling.* 62

32 *Schematic of the hybrid toroid design concept.* 64

33 *Layout of individual conductors within the allowed space at low radius (trapezoidal shapes) in TOSCA for 0.1819 inch OD square conductor (a). Diagram showing the layout for 0.2294 inch OD square conductor, color-coded and labeled by how they are wound in individual "double-pancakes" (b).* 65

34 *Conceptual model of a single hybrid coil, with the segments labeled for reference (a). Model of the actual conductor layout in TOSCA (red) overlayed with the blocky model used for simulation and production of the maps (orange) (b).* 66

35 *Hybrid toroid with no z scaling. Conceptual design for magnet supports also shown.* 67

36 *Møller electrons in the z=28.5 m plane in cylindrical coordinates (radius vs. azimuthal angle ϕ). The detected particles are colored according to which detector they hit, red for the detector in the center of the open sector, blue for the detector in the center of the closed sector and green for the detector which straddles the open and closed sector. On the right is the rate of Møller electrons detected as function of ϕ_{wrap}, the azimuthal angle from the center of the nearest open sector.* 69

37 *Rate of Mott electrons detected as function of Q^2, the square of the four momentum transfered in the scattering. Color convention from Fig. 36.* 69

38 *Rate of Møller electrons as a function of E'_{vert}, the energy of the scattered electron immediately after the interaction (left), and θ_{lab}, the scattering angle in the laboratory frame (right). Color convention from Fig. 36.* 70

39 *Plot comparing the B_x component of the magnetic field (T) vs. z (cm) of the conceptual hybrid (red) and the TOSCA version (black) of the conceptual hybrid for a radius of 15 cm for different bins in ϕ.* 71

40 *Plots showing the progression of changes in the ϕ_{wrap} (left) and θ_{lab} (right) distributions from the conceptual field (top). The conceptual field was first verified using TOSCA (second row) and then the actual conductor layout which was presented at the Magnet Advisory Committee was developed (third row). The default field (bottom) is the result of optimization of the conductor layout which takes into account the suggestions from the Magnet Advisory Committee. Color convention from Figure 36.* 72

41 *Plots comparing the radial (left) and θ_{cm} (right) distributions of the conceptual field (top) and the field for the actual conductor layout (bottom). Color convention from Figure 36.* . . 73

42 *Possible front-end signals assuming a 5.5 GHz event rate and 10 photoelectrons per event. The photomultiplier gain is set to deliver 6 μA to the 1 MΩ current to voltage preamplifier.* . 76

43 *TRIUMF current-to-voltage preamplifier for the Qweak experiment.* 77

44 *TRIUMF VME-based digital integrator for the Qweak experiment.* 78

45 *Schematic of the Hall A Compton polarimeter. Figure from [46].* 79

46 *Energy spectrum of synchrotron radiation penetrating lead shielding of thickness listed. Plot on left shows unmodified chicane magnets, plot on right shows energy spectrum for proposed magnetic shims which reduce the field for the bend radiating into the Compton photon detector acceptance. Note the different horizontal scales between the plots.* 85

47 *The cross-section and asymmetry plotted versus Compton scattered photon energy for the Hall A polarimeter at 11 GeV.* 87

48 *The layout of the Hall A Møller polarimeter in it present configuration. The planned upgrade for 12 GeV includes lifting of the detector box to compensate for a smaller deflection in the dipole.* 93

49 *A sketch of the storage cell.* 94

50 *Simulated spectra of the transitions on the axis of the hydrogen trap with the maximum field of 8.0 T. The density of atoms depends on the field as $exp(-\mu_e B/kT)$. The two curves show $\frac{1}{N}dN/d\nu_{ad}$ and $\frac{1}{N}dN/d\nu_{bc}$ - the relative number of atoms which can undergo $|a\rangle \rightarrow |d\rangle$ and $|b\rangle \rightarrow |c\rangle$ transitions at the given frequency, per one GHz. The resonant structure of the spectral function of the beam-induced electromagnetic field is shown as a set of vertical bars, 499 MHz apart.* 97

51 *Relative magnetization vs. temperature for a pure iron foil driven to magnetic saturation (from [73]). The iron foil used in the Hall C Møller polarimeter is normally at room temperature with no active cooling.* . . . 99

52 *Results of polarization measurements taken in Hall C using the second generation kicker magnet impinging on a 1 μm thick iron foil strip target. Measurements were made at beam currents up to 40 μA. Higher currents were not accessible to due to beam losses from the deflected electron beam. Control measurements at 2 μA were not stable, so these measurements cannot be used to prove 1% precision at high currents.* . . . 100

53 *Schematic of the operating mode of the new kicker magnet to be installed for* Q_{Weak}*. The beam is kicked 1-2 mm in about 1 μs and remains stationary on the Møller target for 1 to several μs.* . . . 100

54 Results of 2006 electron source beat-frequency mode tests. The bottom plot shows the polarization measurements with the beam current controlled using the laser power directly; in the middle plot, the current was reduced using the chopper slit (high current from the photocathode); the top plot shows the current reduced using the beat-frequency technique described in the text. . . . 101

List of Tables

1 *Nominal design parameters for the proposed A_{PV} measurement. Note that some of the design parameters will change at the few percent level as the design is further optimized.* . . 11

2 *Design parameters of the MOLLER Liquid Hydrogen Target* 13

3 *Summary of the coil parameters. The size of the conductor is 0.2294" (square) with a water-cooling hole of 0.128" (ID, round) and 0.08 mm of insulation (0.04 mm half-lapped).* 16

4 *Summary of projected fractional statistical and systematic errors.* 23

5 *Goals for first order corrections from electron beam helicity correlations* 24

6 *Shown are various parameters for several parity experiments, including HAPPEX I, E158, and HAPPEX II-p, that are published, HAPPEX III and PREx, the results of which are available, and QWeak, that is ongoing. Also shown are PREx-II, recently approved, and MOLLER. The second and third columns show the actual measured or projected asymmetries and statistical errors. The fourth column shows the actual or projected error associated with corrections for helicity-correlated beam-parameters. The remaining columns indicate actual or projected limits on helicity-correlated beam parameter differences.* 25

7 *Goals for systematic errors for the Hall A Compton polarimeter at 11 GeV. Topics marked * are a common systematic error between the photon and electron analyses, while the other are largely independent between the detector systems.* 27

8 *A list of systematic errors quoted for the Møller polarimeters in Hall C [39] and in Hall A. The present Hall C configuration is assumed. For Hall A, the first column shows the warm-magnet configuration used prior to 2010, the second column shows the results achieved with the the high-field target, Hall C style upgrade, while the last column shows the expectations for the polarimeter, equipped with an atomic hydrogen target. The regular, low beam current operation is assumed for all, but the last column, which is for operations at high beam currents, but less than $< 100\ \mu A$.* 28

9 *Summary of the Estimated Beam Time (75 μA, $P_e = 80\%$).* 32

10 *Proposed MOLLER project funding profile. Estimates include 40% contingency.* 41

11 *Cost highlights of the MOLLER project. Estimates* **do not** *include contingency. The estimates are actual year dollars based on the profile shown on Table 10. The estimates shown include JLab overhead.* 42

12 *Møller LH_2 target and beam nominal parameters.* 55

13 *Liquid hydrogen targets for parity violation experiments. The first group represents actual operating targets, while the last one is a target under design.* 56

14 *Parameters for the PMT signals from the quartz detector with the largest flux.* 75

15 *Comparison of various sources of noise assuming the signals of Figure 42. "Beam on" shot noise is equivalent to counting statistics. The electronic noise is based on tests with TRIUMF electronics built for the Qweak experiment. The electronic noise alone is negligible compared to counting statistics. A null test with a noiseless battery could be made to $\leq 10^{-9}$ (one ppb) in a day.* 78

16 *Goals for systematic errors for the Hall A Compton polarimeter at 11 GeV. Topics marked * are a common systematic error between the photon and electron analyses, while the other are largely independent between the detector systems.* 82

1 Introduction

1.1 Physics Context

The SU(2)$_L$×U(1)$_Y$ gauge structure within the Standard Model, which gives rise to electroweak interactions, has been subject to stringent tests over more than three decades of precision measurements. Consistency has been achieved at $\sim 0.1\%$, a level of precision where "hard" electroweak radiative corrections involving the top quark, the massive vector bosons, and their scalar interactions, become manifest. No compelling signature for an inconsistency has been found to date, with direct access to center of mass energies of order 200 GeV in $\mathrm{e^+e^-}$ collisions at CERN's LEP ring, of order 1 TeV in the hard scattering of partons in $\mathrm{p\bar{p}}$ collisions at Fermilab's Tevatron, and most recently with the newest data with access to several TeV at CERN's LHC.

Nevertheless, compelling theoretical arguments, input from cosmological observations, and the discovery of neutrino mass strongly motivate the continued exploration of the multi-TeV scale. Direct searches at colliders, where one looks for as yet unobserved new interaction amplitudes at the highest possible center of mass energies, are an essential component of this endeavor. However, an equally important part of the package to determine the full extent of validity of the electroweak theory involves indirect probes, where one looks for deviations from theoretical predictions at much lower center of mass energies.

Classic examples of discoveries that played central roles using indirect probes are the observation of parity-violation in nuclear beta decay, the observation of weak-electromagnetic interference in lepton-quark deep inelastic scattering, and the agreement between direct and indirect determinations of the mass of the top quark. The more recent result of the $(g-2)_\mu$ anomaly is perhaps the harbinger of a program in search of the "New Standard Model". Remarkably, the next generation of viable projects in such a program requires critical input from nuclear theory as well as measurement techniques pioneered by nuclear experimentalists.

In this document, we present the MOLLER experiment, a new measurement that would build on the concept of indirect probes. We propose to measure the parity-violating asymmetry in the scattering of longitudinally polarized electrons off unpolarized electrons, using the upgraded 11 GeV beam in Hall A at Jefferson Laboratory, to an overall fractional accuracy of 2.3%. Such a measurement would constitute more than a factor of five improvement in fractional precision over the only other measurement of the same quantity by the E158 experiment at SLAC [1]. The electron beam energy, luminosity and stability at Jefferson Laboratory are uniquely suited to carry out such a measurement, making it feasible to achieve a new benchmark in sensitivity to probe the validity of the electroweak theory at the multi-TeV scale.

There are two primary reasons why the proposed measurement represents a compelling new opportunity:

- New neutral current interactions are best parameterized model-independently at low energies by effective four-fermion interactions via the quantity Λ/g, where g characterizes the strength and Λ is the scale of the new dynamics. The proposed A_{PV} measurement is sensitive to interaction amplitudes as small as 1.5×10^{-3} times the Fermi constant, G_F, which corresponds to a sensitivity of $\Lambda/g = 7.5$ TeV. This would be *the* most sensitive probe of new flavor and CP-conserving neutral current interactions in the leptonic sector until the advent of a linear collider or a neutrino factory.

- Within the Standard Model, weak neutral current amplitudes are functions of the weak mixing angle $\sin^2\theta_W$. The two most precise independent determinations of $\sin^2\theta_W$ differ by 3 standard deviations. While the world average is consistent with other electroweak measurements and constraints on the Higgs boson mass M_H, choosing one or the other central value ruins this consistency and implies very different new high-energy dynamics. The proposed A_{PV} measurement, which would achieve a sensitivity of $\delta(\sin^2\theta_W) = \pm 0.00029$, is the only method available in the next decade to directly address this issue at the same level of precision and interpretability.

The 2007 NSAC long range planning exercise and its associated report [2] comprehensively described the opportunities presented by new sensitive indirect probes such as MOLLER, and how they fit into the subfield of Fundamental Symmetries. The SLAC E158 A_{PV} result was highlighted as one of the important accomplishments of the subfield in the previous 7 years. As also highlighted in the report, one of the overarching questions that serves to define this subfield is: "What are the unseen forces that were present at the dawn of the universe but disappeared from view as the universe evolved?". To address this question and as part of the third principal recommendation, significant new investments were advocated.

The list included investment for equipment and infrastructure for two new parity-violating electron scattering projects that would use the upgraded 11 GeV beam at Jefferson Laboratory. These two projects, named MOLLER and SOLID, have since been formally proposed and reviewed by JLab's Program Advisory Committee (PAC). In January 2010, a Director's review of the MOLLER project was carried out, chaired by C. Prescott. The review committee strongly endorsed the physics goals of the project and urged JLab to begin preparations to support the development of the experiment. In January 2011, the PAC was assigned the task of grading all approved JLab upgrade experiments in the Fundamental Symmetries category. The MOLLER project received the highest rating and was allocated its full beamtime request of 344 PAC days. This document presents the case to receive primary funding for MOLLER from the Department of Energy.

1.2 Definitions and Precision Goal

Polarized electron scattering off unpolarized targets provides a clean window to study weak neutral current interactions. These experiments measure an asymmetry defined by

$$A_{PV} = \frac{\sigma_R - \sigma_L}{\sigma_R + \sigma_L} \quad , \tag{1}$$

where σ_R (σ_L) is the scattering cross-section using incident right (left) handed electrons. A non-zero asymmetry constitutes parity nonconservation, dominated at $Q^2 \ll M_Z^2$ by the interference between the weak and electromagnetic amplitudes [3].

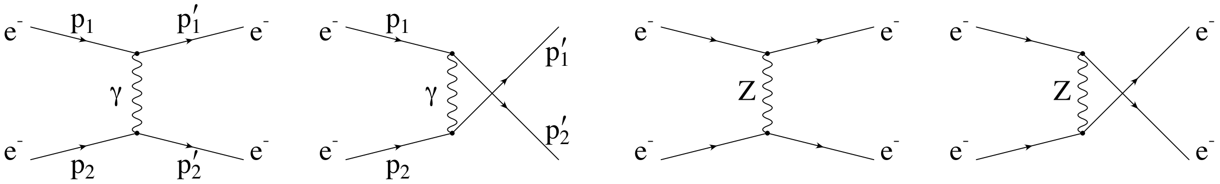

Figure 1: *Feynman diagrams for Møller scattering at tree level (reproduced from Ref. [6])*

The leading order Feynman diagrams relevant for Møller scattering, involving both direct and exchange diagrams that interfere with each other, are shown in Fig. 1. The total unpolarized cross section, dominated by photon exchange, is given by

$$\frac{d\sigma}{d\Omega} = \frac{\alpha^2}{2mE}\frac{(3+\cos^2\theta)^2}{\sin^4\theta} = \frac{\alpha^2}{4mE}\frac{1+y^4+(1-y)^4}{y^2(1-y)^2}, \tag{2}$$

where α is the fine structure constant, E is the incident beam energy, m is the electron mass, θ is the scattering angle in the center of mass frame, $y \equiv 1 - E'/E$ and E' is the energy of one of the scattered electrons. The parity-violating asymmetry A_{PV}, due to the interference between the photon and Z^0 boson exchange diagrams in Fig. 1, is given by [4]

$$A_{PV} = mE\frac{G_F}{\sqrt{2}\pi\alpha}\frac{4\sin^2\theta}{(3+\cos^2\theta)^2}Q^e_W = mE\frac{G_F}{\sqrt{2}\pi\alpha}\frac{2y(1-y)}{1+y^4+(1-y)^4}Q^e_W \tag{3}$$

where Q^e_W (proportional to the product of the electron's vector and axial-vector couplings to the Z^0 boson) is the weak charge of the electron. The electroweak theory prediction at tree level in terms of the weak mixing angle is $Q^e_W = 1 - 4\sin^2\theta_W$; this is modified at the 1-loop level [5, 6, 7] and becomes dependent on the energy scale at which the measurement is carried out, *i.e.* $\sin^2\theta_W$ "runs". It increases by approximately 3% compared to its value at the scale of the Z^0 boson mass, M_Z; this and other radiative corrections reduce Q^e_W to 0.0469 ± 0.0006, a $\sim 40\%$ change of its tree level value of ~ 0.075 (when evaluated at M_Z).

The prediction for A_{PV} for the proposed experimental design is ≈ 35 parts per billion (ppb) and our goal is to measure this quantity with a statistical precision of 0.73 ppb and thus achieve a 2.3% measurement of Q^e_W. The reduction in the numerical value of Q^e_W due to radiative corrections leads to increased fractional accuracy in the determination of the weak mixing angle, $\sim 0.1\%$, comparable to the two best such determinations from measurements of asymmetries in Z^0 decays in the e^+e^- colliders LEP and SLC.

2 Physics Motivation

In this section we elaborate on the two primary motivation bullets itemized in the introduction. An important point to note is that, at the proposed level of measurement accuracy of A_{PV}, the Standard Model (SM) calculation must be carried out with full treatment of one-loop radiative corrections and leading two-loop corrections. "Hard" radiative corrections involving the massive vector bosons at the loop level modify the tree-level prediction quite significantly [5]. The dominant effect comes from the "$\gamma - Z$ mixing" diagrams depicted in Fig. 2 [6]. Subsequently, the theoretical error from extrapolation to the Q^2 of the measurement was reduced significantly [7]. An accurate calculation of the Standard Model prediction for A_{PV} must take into account the detailed kinematic acceptance of the final apparatus to account for other Q^2 and $y-$dependent terms in the radiative corrections [8].

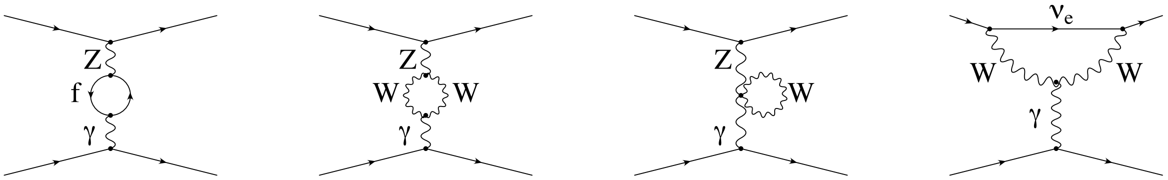

Figure 2: *$\gamma-Z$ mixing diagrams and W-loop contribution to the anapole moment (reproduced from Ref. [6])*

The fact that the proposed measurement provides such a sensitive probe of TeV-scale dynamics is a consequence of a very precise experimental goal ($\sim 10^{-3} \bullet G_F$), the energy scale of the reaction ($Q^2 \ll M_Z^2$), and the ability within the electroweak theory to provide quantitative predictions with negligible theoretical uncertainty. Remarkably, the proposed measurement is the only practical way to measure a purely leptonic amplitude at $Q^2 \ll M_Z^2$ at the proposed level of precision in the foreseeable future at any existing or planned facility worldwide.

2.1 New Contact Interactions

A fairly general and model-independent way to quantify the effects of new high-energy dynamics in low-energy processes is to express the resulting new amplitudes in terms of contact interactions among leptons and quarks. Specializing here to vector and axial-vector interactions between electrons and/or positrons, such an interaction Lagrangian takes the form [9]:

$$\mathcal{L}_{\mathrm{e_1 e_2}} = \sum_{i,j=L,R} \frac{g_{ij}^2}{2\Lambda^2} \bar{e}_i \gamma_\mu e_i \bar{e}_j \gamma^\mu e_j, \tag{4}$$

where $e_{L/R} = \frac{1}{2}(1 \mp \gamma_5)\psi_e$ are the usual chirality projections of the electron spinor, Λ is the mass scale of the contact interaction, $g_{ij} = g_{ij}^*$ are coupling constants, and $g_{RL} = g_{LR}$.

For the proposed measurement with 2.3% total uncertainty (and no additional theoretical uncertainty) the resulting sensitivity to new 4-electron contact interaction amplitudes can be expressed as:

$$\frac{\Lambda}{\sqrt{|g_{RR}^2 - g_{LL}^2|}} = \frac{1}{\sqrt{\sqrt{2} G_F |\Delta Q_W^e|}} \simeq \frac{246.22 \text{ GeV}}{\sqrt{0.023 Q_W^e}} = 7.5 \text{ TeV}. \tag{5}$$

For example, models of lepton compositeness are characterized by strong coupling dynamics. Taking $\sqrt{|g_{RR}^2 - g_{LL}^2|} = 2\pi$ shows that mass scales as large as $\Lambda = 47$ TeV can be probed, far beyond the center of mass energies of any current or planned high energy accelerator. This allows electron substructure to be studied down to the level of 4×10^{-21} m.

The best current limits on contact interaction scales come from the high-energy collider data of LEP 2 and the Tevatron, where the latter is sensitive to new interactions involving quarks. The strongest constraints on the coefficients in Eqn. (4) come from LEP 2. We emphasize, however, that the parity-conserving cross-sections and forward-backward asymmetries studied at LEP 2 are only sensitive to g_{RL}^2 and the combination $g_{RR}^2 + g_{LL}^2$. Making the additional assumption that the former (latter) is vanishing, the combination of all four LEP 2 experiments corresponds to sensitivities of $\Lambda/\sqrt{g_{RR}^2 + g_{LL}^2} = 4.4$ TeV ($\Lambda/g_{RL} = 5.2$ TeV), while LEP 2 is blind to the parity-violating combination $g_{RR}^2 - g_{LL}^2$ probed by A_{PV}.

Thus, the proposed measurement would greatly extend the current sensitivity of 4-electron contact interactions, both qualitatively and quantitatively[1]. Using Eqn. (5), it is also straightforward to examine its reach in specific models, and compare the sensitivity to other low-energy precision electroweak observables [10]. We discuss three examples in the following: supersymmetry, Z' bosons and doubly-charged scalars. The latter two scenarios have been recently analyzed specifically for the case of Møller scattering [11].

2.1.1 Supersymmetry

At the level of sensitivity probed, the proposed measurement could be influenced by radiative loop effects of new particles predicted by the Minimal Supersymmetric Standard Model (MSSM). The impact on the weak charges of the electron and the proton $Q_W^{e,p}$ have been analyzed in detail [12]. Here, we reproduce the results from a recent review [13]. In Fig. 3, the dots on the right hand side show the results of a random scan over a set of MSSM parameters whose values are consistent with current precision measurements and search limits. Generally speaking, there is a modest increase in the effects at larger values of the MSSM parameter $\tan\beta$ (the ratio of vacuum expectation values of the model's two Higgs scalars) or if one of the superpartner masses is relatively light. The allowed loop contributions to Q_W^e can be as large as $+8\%$ which, given our projected error bar, would constitute a deviation of 3.5 σ.

---

[1] Our proposed measurement is also complementary to new physics searches via the Electric Dipole Moment (EDM) of the electron which is modified only if the new interactions violate CP symmetry.

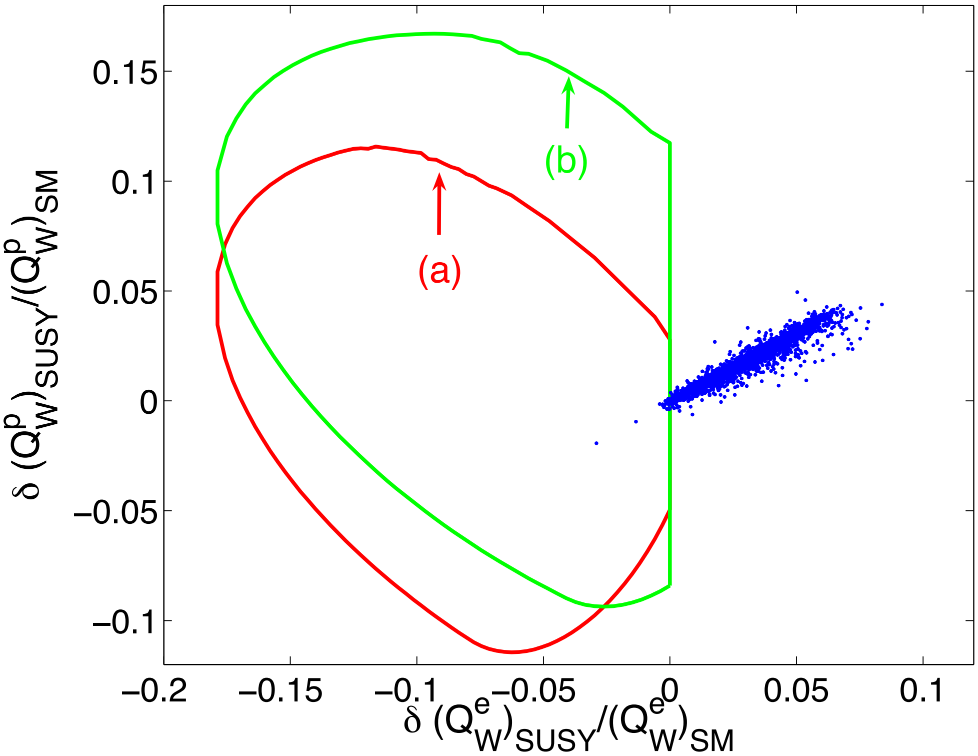

Figure 3: *Relative shifts in the electron and proton weak charges due to SUSY effects. Dots indicate the range of allowed MSSM-loop corrections. The interior of the truncated elliptical regions give possible shifts due to R-parity violating (RPV) SUSY interactions, where (a) and (b) correspond to different assumptions on limits derived from first row CKM unitarity constraints.*

If the assumption of R-parity conservation is relaxed (RPV), tree-level interactions could generate even larger deviations in Q_W^e. The left-hand side of Fig. 3 shows the allowed region in the parameters Q_W^e and Q_W^p after constraints from low-energy precision data have been taken into account. In this case, relative deviations from the Standard Model value of Q_W^e of up to -18% are allowed, a shift of almost 8 σ. The predicted correlations between the approved 4% Q_W^p measurement and our proposed Q_W^e measurement will provide tighter constraints than either measurement alone, another example of complementarity between precision electroweak experiments.

It should be emphasized that if nature is indeed supersymmetric, the sign of the relative shift in Q_W^e would, if large enough, distinguish between R-parity conserving (RPC) and RPV versions of SUSY. The difference is not academic, since RPC would imply that the lightest supersymmetric particle is stable and therefore an obvious candidate for the non-baryonic dark matter which is needed to understand galactic-scale dynamics. On the other hand, RPV would imply that neutrinos are Majorana particles. A 5% effect in Q_W^e interpreted as arising from RPV SUSY would generate a one-loop contribution to the neutrino mass of the order of 1 eV, comparable to current bounds.

2.1.2 Z′ Bosons

Many theories of new TeV-scale dynamics predict the existence of new, super-massive Z' bosons with masses in the TeV range. The proposed A_{PV} measurement would see a a statistically significant deviation in many models that predict Z' bosons in the 1 to 2 TeV mass range. In the following we identify the chiral Z' couplings times $U(1)'$ charges to right-handed and left-handed electrons with g_{RR}^2 and g_{LL}^2, and we also identify Λ with the Z' mass, $M_{Z'}$. For example, for the so-called Z_χ boson appearing in $SO(10)$ Grand

Unified Theories one predicts

$$\sqrt{|g_{RR}^2 - g_{LL}^2|} = \sqrt{\frac{4\pi\alpha}{3\cos^2\theta_W}} \approx 0.2,$$

implying that Z_χ bosons with masses up to about 1.5 TeV could affect the proposed measurement. Similarly, the Z_{LR} boson appearing in left-right symmetric models couples with strength

$$\sqrt{|g_{RR}^2 - g_{LL}^2|} = \sqrt{\frac{\pi\alpha}{\cos^2\theta_W(1 - 2\sin^2\theta_W)}} \approx 0.24,$$

corresponding to a 1.8 TeV reach for this boson. Updating the analysis in reference [14] we obtain the current bound $M_{Z_\chi} > 1.16$ TeV and $Z_{LR} > 1.02$ TeV at 95% CL.

The LHC will be able to probe the region from 1 to 5 TeV, which is currently unexplored by any direct or indirect measurement. However, extracting the detailed properties of the Z' such as its width, chiral couplings to SM fermions etc. will be difficult for $M_{Z'} \gtrsim 2$ TeV. In the 1-2 TeV range, good discrimination between various models will become possible with a large integrated luminosity sample ($\gtrsim$ 100 fb^{-1}, see for example [15]). In the following, we approach the analysis under the following scenario: that the LHC has found new physics in their data analysis that is consistent with a new spin-1 gauge boson with $M_{Z'} = 1.2$ TeV, which is above current lower bounds from experiments.

In such a scenario, the importance of off-peak LHC data as well as low-energy precision EW data to completely disentangle all of the chiral Z' couplings to SM particles has been emphasized [16]. The impact of new constraints from the proposed A_{PV} measurement and a very large integrated luminosity LHC data sample ($1\ \mathrm{ab}^{-1}$) was demonstrated explicitly for the Z_χ and Z_{LR} models. It was found that MOLLER would provide an important constraint such that a combined analysis with LHC data would allow for an independent determination of the left- and right-handed leptonic Z' couplings and make it thus possible to distinguish between models.

A more comprehensive analysis of the MOLLER sensitivity to TeV-scale Z's has recently been carried out [17] for a fairly large class of family-universal models contained in the E_6 gauge group. While models with full E_6 unification are already excluded by existing precision electroweak data, the Z' bosons in these models with the same electroweak charges to SM particles are still motivated because they also arise in many superstring models as well as from a bottom-up approach [18]. That approach imposes the cancellation of gauge and mixed gauge-gravitational anomalies in supersymmetric extensions of the SM together with a set of fairly general requirements such as allowing the SM Yukawa couplings, gauge coupling unification, chirality (to protect all fields from acquiring very large masses), a solution [19, 20] to the μ-problem [21], and the absence of fractional electric charges and dimension-4 proton decay.

The MOLLER reach for a 1.2 TeV Z' from this model class, assuming the value predicted by the SM is measured, along with the current region excluded by E158, is shown in Fig. 4. These models are spanned by two parameters α and β in the range $\pm\pi/2$. $\alpha = 0$ corresponds to the E_6 models considered for example in Ref. [11], while $\alpha \neq 0$ can be interpreted as non-vanishing kinetic mixing, assuming that this kinetic mixing has been undone by field re-definitions. $\beta = 0$ correspond to $SO(10)$ models, which include models based on left-right symmetry.

On the other hand, if MOLLER measures a central value consistent with E158, then a clear violation of the SM would be established at more than 5σ. It is interesting to explore the consequences of such a scenario combined with the abovementioned LHC 1.2 TeV resonance observation. Kaluza-Klein gravitons in models with large extra dimensions can mimic the topology of a Z' at the LHC. However, contributions of such gravitons to the proposed A_{LR} measurement are highly suppressed. Further, no Z' from the abovementioned model class can explain such a MOLLER deviation either. In this scenario, this entire class of Z' models as well as Kaluza-Klein gravitons would be ruled out as candidates for the underlying theory to explain the two anomalies simultaneously.

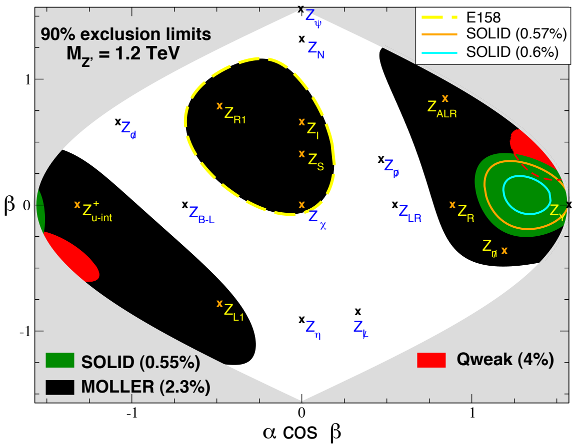

Figure 4: *90% C.L. exclusion regions for a 1.2 TeV Z' (E_6 gauge group) for MOLLER, Qweak and SOLID, assuming they obtain exactly the SM predictions. Also shown is the contour from the E158 result.*

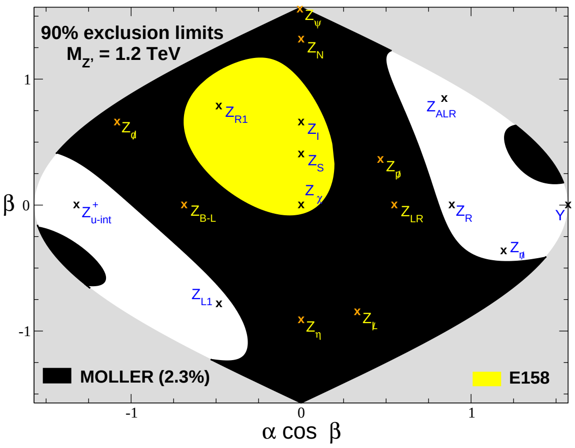

Figure 5: *90% C.L. exclusion regions for a 1.2 TeV Z' from the E_6 gauge group for E158, and MOLLER, assuming the MOLLER central value is half-way between the E158 central value and the SM prediction.*

Finally, we can ask what would be the consequence if MOLLER measured a value half-way between the SM value and the E158 central value. Then, a certain region of parameter space in this class of Z' models would be favored, as shown in Fig. 5. Thus, the combination of potential MOLLER and LHC anomalies would point to a small list of Z' models, whose effects on other precision EW observables can then be further explored at LHC and elsewhere.

2.1.3 Doubly-Charged Scalars

Doubly charged scalars naturally arise in extended Higgs sector models that contain complex triplet representations of SU(2). The left-right symmetric model, for example, contains two such triplets – Δ_L and Δ_R – that transform under $\mathrm{SU}(2)_L$ and $\mathrm{SU}(2)_R$ respectively. The doubly-charged components of both triplets, $\delta^{++}_{L,R}$ can couple to two charged leptons:

$$\mathcal{L}^{\delta^{++}}_{\text{matter}} \sim h^{ij}_L\, \delta^{++}_L \bar{\ell}^C_i P_L \ell_j + h^{ij}_R\, \delta^{++}_R \bar{\ell}^C_i P_R \ell_j + \text{h.c.} \tag{6}$$

where ℓ_i denotes a charged lepton of generation i. The Møller scattering process is unique among lepton scattering observables to be sensitive to the $s-$channel exchange 4-electron amplitude that violates lepton number by 2 units (two analogous expressions LL and RR):

$$\mathcal{M}^{\text{PV}} \sim \frac{|h^{ee}_L|^2}{2M^2_{\delta_L}} \bar{e_L}\gamma_\mu e_L \bar{e_L}\gamma^\mu e_L \quad . \tag{7}$$

Gauge and matter interactions involving the $\delta^{++}_{L,R}$'s can also lead to contributions to neutrinoless double-beta decay processes and charged lepton flavor violating processes such as $\mu \to e$ conversion [22]. In general, these processes can put severe limits on these possible new amplitudes, but in the latter case only in models predicting unsuppressed off-diagonal charged lepton couplings $h^{\mu e}_{L,R}$. Neutrinoless double-beta decay gives much weaker constraints for the Δ_L triplet because its vacuum expectation value is constrained to be smaller than a few GeV from electroweak precision data (the ρ parameter).

The amplitude in Eqn. (7) shows that the Δ_L model is equivalent to a contact interaction with $\Lambda = M_{\delta_L}$, $|g^2_{LL}| = |h^{ee}_L|^2/2$, and $g_{RR} = g_{LR} = 0$. The proposed A_{PV} measurement would therefore lead to the most stringent probe of the left-handed charged scalar and its coupling to electrons, with a reach of

$$\frac{M_{\delta_L}}{|h_L^{ee}|} \sim 5.3 \text{ TeV},$$

significantly above the LEP 2 constraint of about 3 TeV.

2.2 Precision Electroweak Measurements and $\sin^2\theta_W$

The weak mixing angle $\sin^2\theta_W$ has played a central role in the development and validation of the electroweak theory, especially testing it at the quantum loop level, which has been the central focus of precision electroweak physics over the past couple of decades. To develop the framework, one starts with three fundamental experimental inputs characterizing, respectively, the strength of electroweak interactions, the scale of the weak interactions, and the level of photon-Z^0 boson mixing.

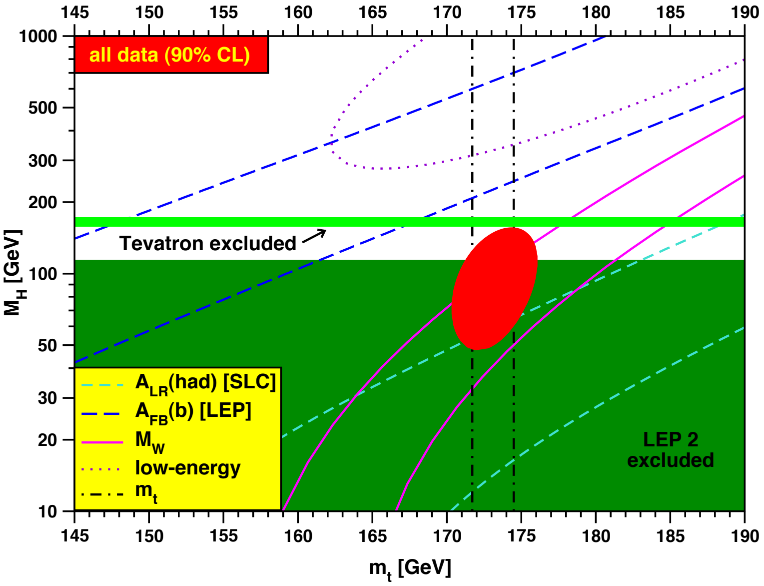

Figure 6: *Summary of* 1σ *bands from various precision measurements. The red (filled) ellipse is the 90% C.L. contour of all precision electroweak data. The colored regions are excluded by direct colliders searches. The strongest constraint on the width of the purple (dotted) contour (*$Q^2 \ll M_Z^2$ *measurements) is E158, while its shape and location are influenced by NuTeV [23, 24] (deep inelastic* ν*-scattering): large values of* M_H *are favored, similar to the* $A_{FB}(b)$ *band. In contrast,the* $A_{LR}(had)$ *and* M_W *bands favor very low values of* M_H *which are already ruled out by direct searches. The proposed* A_{PV} *measurement would dominate the future width and location of the dotted contour.*

The three fundamental inputs are chosen to be α (from the e$^\pm$ anomalous magnetic moment), G_F (from the muon lifetime) and M_Z (from the LEP Z^0 line-shape). Precise theoretical predictions for other experimental observables at the quantum-loop level can be made if experimental constraints on the strong coupling constant and heavy particle masses, such as M_H and the top quark mass, m_t, are also included.

Precision measurements of the derived parameters such as the W boson mass M_W, and the weak mixing angle $\sin^2\theta_W$ are then used to test the theory at the level of electroweak radiative corrections. Consistency (or lack thereof) of various precision measurements can then be used to constrain the one unknown mass in the Standard Model, *i.e.* M_H, and search for indications of physics beyond the Standard Model.

Global analyses of all precision data have constrained the Standard Model Higgs boson to be within a relatively narrow mass window: 55 GeV $\leq M_H \leq$ 135 GeV at 90% C.L.. Further, direct searches at colliders require that the Higgs boson be heavier than 114.4 GeV at 95% C.L. from LEP200 [25]. In addition, Tevatron data exclude the region from 158 GeV $\leq M_H \leq$ 173 GeV at 95% C.L. [26]. The most precise inputs to the indirect limit come from precision $\sin^2\theta_W$ measurements from various asymmetry observables in the production and decay of Z bosons, as well as M_W measurements from real W production.

While there is no significant conflict between direct and indirect limits on M_H, it is instructive to study the "pull" of individual measurements, as depicted in Fig. 6. Various measurements of M_W are mutually consistent and the purple (solid) lines shows the 1σ allowed band of the grand average. With the constraint from the direct measurement of m_t from Fermilab (dot-dashed vertical black lines in Fig. 6), it can be seen that the M_W band points to a low M_H, almost (but not quite) in disagreement with the direct exclusion limit.

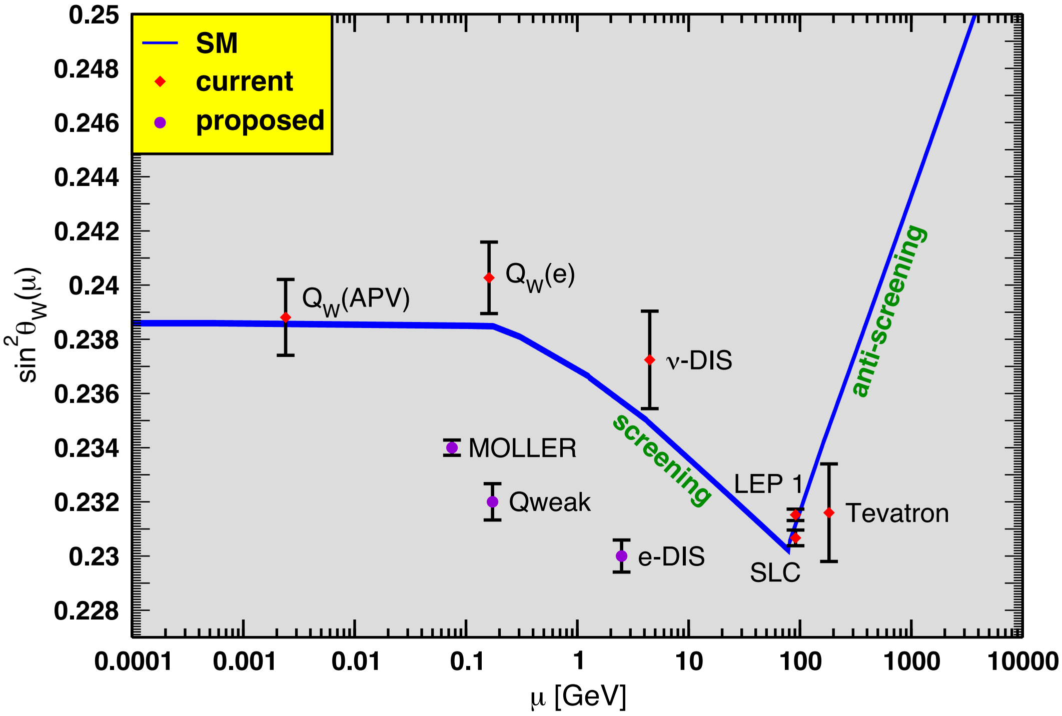

Figure 7: *Current and proposed weak mixing-angle measurements vs. the energy scale μ. The three future measurements are located at appropriate μ values but the vertical locations are arbitrary. Note that the PDG value of ν-DIS has been adjusted from the published value.*

The blue and green dashed lines respectively, are the constraints from the most precise single determinations of $\sin^2\theta_W$: the left-right asymmetry in Z production at SLC (A_{LR}(had)) and the forward-backward asymmetry in Z decays to b-quarks ($A_{\mathrm{FB}}(b)$ [LEP]) [27]. It can be seen that the M_H constraints from these two measurements are quite different [28]. On the one hand, A_{LR}(had)) indicates a very small M_H which is already ruled out by direct searches. On the other hand, $A_{\mathrm{FB}}(b)$ [LEP] indicates a very large M_H and is in tension with constraints from all indirect measurements (solid red ellipse). The proposed measurement would constrain $\sin^2\theta_W$ with similar accuracy to the abovementioned two Z resonance measurements, and thus could potentially influence the world average of this fundamental electroweak parameter.

The purple dotted contour in the figure is the current constraint from low-energy measurements. It currently favors large values of M_H, albeit with low precision. The proposed measurement would dominate the equivalent future contour, strongly influencing the sensitivity to as yet undiscovered super-weak interactions at the TeV scale, in contrast to measurements on the Z^0 resonance, as discussed in the previous section.

A convenient way to track various electroweak measurements is to use $\sin^2\theta_W$ as a bookkeeping parameter. As mentioned earlier, $\sin^2\theta_W$ "runs" due to electroweak radiative corrections, as shown in Fig. 7. Apart from the proposed measurement and the two Z^0 resonance measurements discussed above, various published and proposed measurements at different energy scales are also shown.

In conclusion, it is evident that a third determination of the weak mixing angle with similar precision to the two most precise high-energy collider determinations discussed above and depicted in Fig. 6 would have a major impact on our view of the data. It could also guide particle phenomenology along the correct path to interpret indications of physics beyond the Standard Model that might be observed at the LHC.

3 Experimental Design

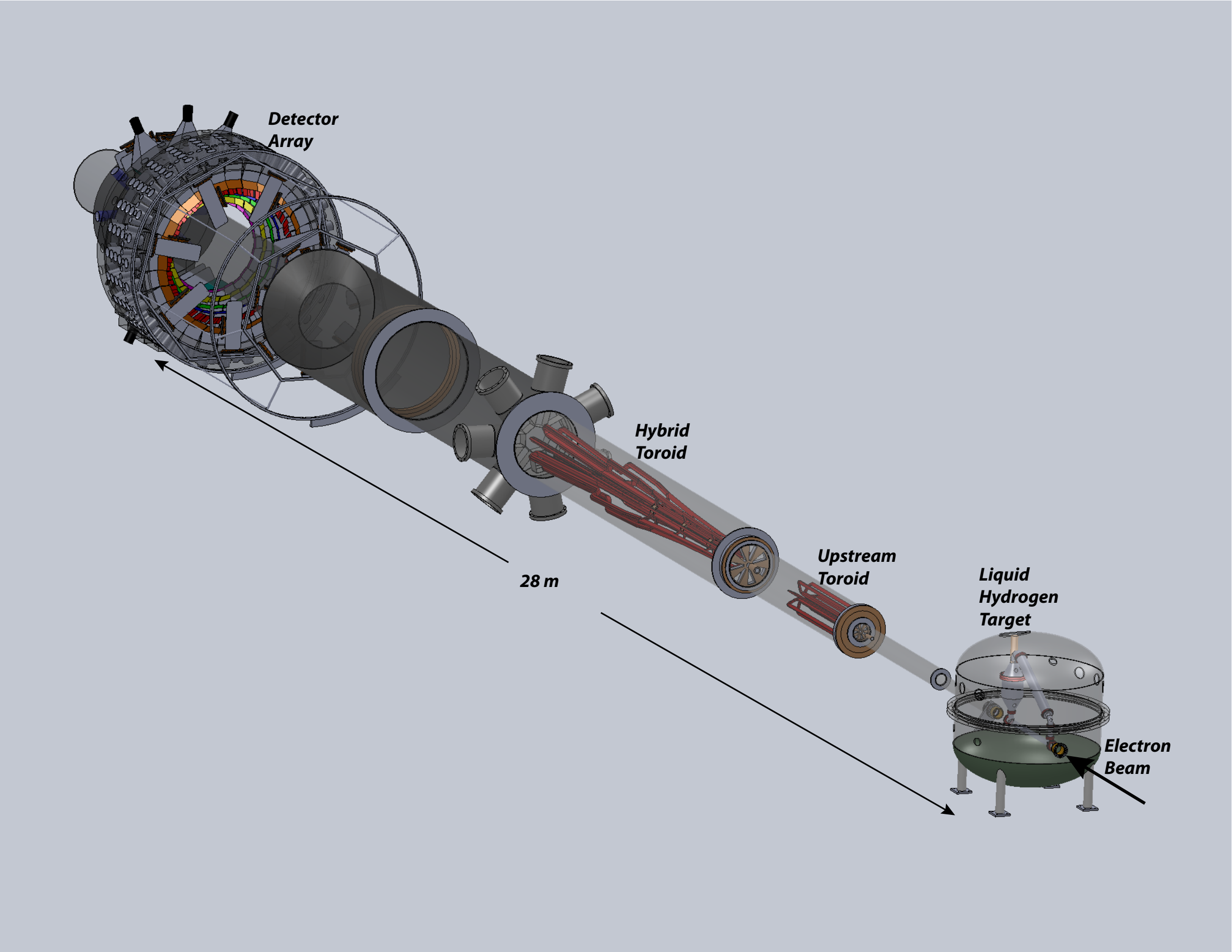

Figure 8: *Layout of the target, spectrometer and detectors.*

A CAD-generated rendition of the layout of the MOLLER apparatus to be placed in Hall A at JLab is shown in Fig. 8. In this section, we provide an overview of the experimental design and discuss the main

Table 1: *Nominal design parameters for the proposed A_{PV} measurement. Note that some of the design parameters will change at the few percent level as the design is further optimized.*

Parameter	Value
E [GeV]	$\approx$ 11.0
E' [GeV]	1.8 - 8.8
θ_{cm}	46°-127°
θ_{lab}	0.23°-1.1°
$< Q^2 >$ [GeV^2]	0.0056
Maximum Current [μA]	85
Target Length (cm)	150
ρ_{tgt} [g/cm^3] (T= 20K, P = 35 psia)	0.0715
Max. Luminosity [cm^{-2} sec^{-1}]	$3.4 \cdot 10^{39}$
σ [μBarn]	$\approx$ 40
Møller Rate [GHz]	$\approx$ 135
Statistical Width(2 kHz flip) [ppm/pair]	$\approx$ 83
Target Raster Size [mm]	5 x 5
ΔA_{raw} [ppb]	$\approx$ 0.6
Background Fraction	$\approx$ 0.08
P_{beam}	$\approx 85\%$
$< A_{pv} >$ [ppb]	$\approx$ 35
$\Delta A_{stat}/ < A_{expt} >$	2.1%
$\delta(\sin^2 \theta_W)_{stat}$	0.00026

subsystems. We start by listing the main experimental parameters in Table 1. Many of the technical choices are driven by the requirement to measure a very small parity-violating asymmetry, and consequently the need to measure the scattered electron flux at an unprecedentedly high rate. The MOLLER design is grounded on the extensive experience gained by the collaboration from completed high flux integrating parity-violation measurements such as MIT-Bates ^{12}C [29], SAMPLE [30], HAPPEX [31] and SLAC E158 [1] as well as ongoing projects such as PREX [32] and Qweak [33].

3.1 Polarized Beam

The polarized electron beam is created using a technology first developed at SLAC to enable the original parity-violating electron scattering experiment [34]: laser-induced photoemission from a GaAs wafer. The circular polarization of the laser light, controlled by the polarity of the voltage across a Pockels cell [2], determines the sign of the longitudinal polarization of the emitted electron bunch, thus facilitating rapid helicity reversal of the electron beam. Time “windows” are generated in the electron bunch train at a frequency of 1.92 kHz, with the sign of the beam’s longitudinal polarization in each window assigned on a pseudo-random basis (with a set pattern of 32 windows optimized to eliminate 60 Hz noise). The design of the apparatus is based on a maximum beam intensity of 85 μA.

Nearby time windows of opposite helicity form window-pairs. The time-averaged responses of beam position monitors characterize the beam trajectory and energy for each window. The monitoring instrumen-

---

[2] The Pockels cell is a birefringent crystal whose phase retardation is directly proportional to the applied potential difference; $\sim \pm 2.5$ kV is required to produce $\pm\pi/4$ retardation for a wavelength of $\sim$ 800 nm.

tation has to be precise enough so that the relative cross section (except for statistical fluctuations) is stable over nearby time windows at the level one part in 10^5, after beam fluctuations are regressed out. Therefore, beam properties must be measured window by window with high precision and further, the variance of window pair differences must be small. Specifically, the beam centroid fluctuations must be tracked with precision at the level of a few microns, and should be stable to $\sim$10's of microns, at 1 kHz[3].

Averaged over the entire data collection period, the beam trajectory must remain unchanged with respect to the sign of the electron beam polarization at the sub-nanometer level in order to keep beam-related false asymmetry corrections at the 1 ppb level. It will be necessary to use a "slow reversal" of beam helicity to further cancel systematic errors to the 0.1 ppb level, from sources such as residual electronics cross-talk and higher-order effects such as potential helicity-dependent variations in the beam spot size. These considerations are discussed in Sec. 4.1 and in App. A.

3.2 Liquid Hydrogen Target

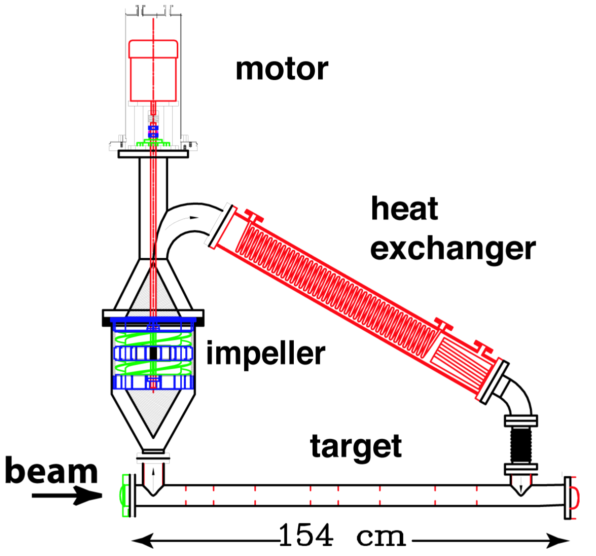

Figure 9: *The SLAC E158 target loop is shown; MOLLER proposes to use the same concept. Liquid flows clock-wise in the picture (downstream to upstream). The liquid-gas interface is just below the motor.*

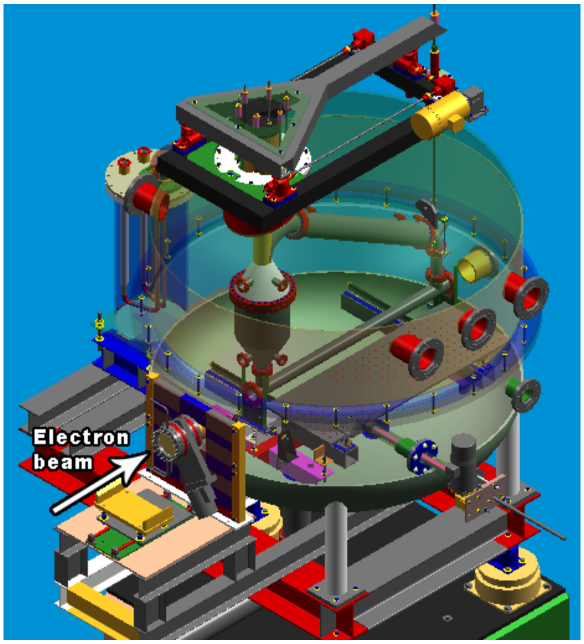

Figure 10: *A CAD drawing of the SLAC E158 target chamber. The target loop is remotely movable 6 in in the vertical direction. A table containing optics targets can be moved in and out horizontally.*

After acceleration to 11 GeV, the electron beam will impinge on a liquid hydrogen (LH_2) target. Hydrogen is the ideal source of target electrons for two reasons. First, it provides the greatest electron target thickness for the least radiation length. Secondly, the irreducible backgrounds are confined to radiative electron-proton elastic and inelastic scattering, which are relatively well-understood. Scattering off other nuclei would include radiative elastic scattering ($\propto Z^2$), breakup channels and scattering off neutrons, which would introduce significant systematic errors due to unknown and potentially large electroweak couplings.

In order to achieve the necessary rate, more than 10 g/cm^2 of LH_2 is needed, making the target about 150 cm long, which in turn requires a cryogenic target system capable of handling a heat load of $\sim$ 5 kW

---

[3] This does not include 60 Hz noise, since data will be collected in time-slots phased to 60 Hz.

Table 2: *Design parameters of the MOLLER Liquid Hydrogen Target*

Parameter	Value
nominal cell length [cm]	150
target thickness [gm/cm^2]	10.72
radiation length [%]	17.5
p [psia]	35
T [K]	20
target power [kW]	5

from the beam. This is far larger than the typical ~ 1 kW targets that are routinely in use and about twice as large as the recently commissioned target for the Qweak experiment.

The preliminary assessment is that the E158 target cell is a good starting point for the design of the high power target required for MOLLER. Figure 9 shows the E158 target loop containing the main target cell, impeller, hydrogen motor and heat exchanger. The hydrogen flowed against the beam direction. The target loop was housed in a scattering chamber (Fig. 10) which also contained a table with auxiliary targets, with the capability to move both remotely, the main target loop in the vertical and the table in the horizontal direction. The target chamber also serves as a secondary containment vessel for hydrogen, which satisfied a major safety concern for E158. The final design of the MOLLER target will make use of computational fluid dynamics (CFD), a key recent development which has been validated by the successful operation of the Qweak target.

Table 2 shows the main parameters of the target. From the physics point of view, the most important design consideration is suppression of density fluctuations at the timescale of the helicity flip rate, which can ruin the statistical reach of the flux integration technique. Preliminary estimates based on operational experience with the Qweak target suggest that density variation can be maintained at $\lesssim 26$ ppm at 1.92 kHz, corresponding to 5% excess noise. A plan for adequate target cooling at the JLab site has been formulated. All the considerations raised in this subsection are discussed in detail in App. B.

3.3 Toroidal Spectrometer

The experimental configuration downstream of the target is quite novel due to some remarkable features of the Møller scattering process. The topology of interest in the 2-electron system is in the vicinity of $\Theta_{COM} = 90^\circ$. However, the acceptance in the highly boosted laboratory frame is at extremely forward angles (θ_{lab} between 5 and 20 mrad) because the COM energy for a 11 GeV electron scattering off a target electron is 106 MeV. It also implies that scattered electrons in the laboratory frame between 2 and 8.5 GeV must be selected, a very large fractional momentum bite.

In addition, the measurement needs as much rate as possible and we must therefore accept scattered electrons over the full range of the azimuthal angle ϕ, which would make the rate of more than 150 GHz available. At this high rate, the only practical solution is to integrate the detector response of each window, eliminating dangerous dead-time systematics. This so-called flux-integration technique requires that Møller-scattered electrons be focused into a region otherwise free of background. All of the above considerations have led us to a unique solution involving two back-to-back toroids, one them conventional (albeit long and quite skinny) and one quite novel. Collimation is a very important issue in such a system.

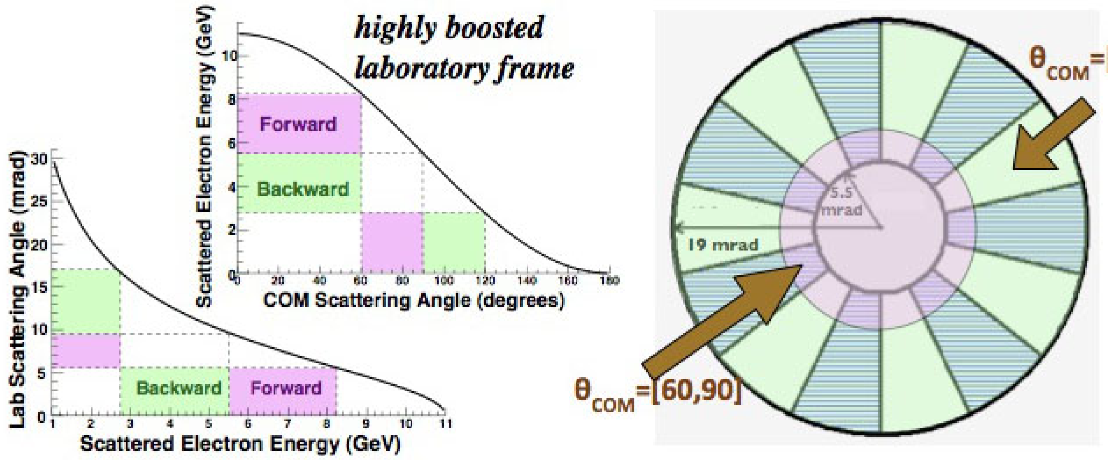

Figure 11: Θ_{COM} *vs* E'_{lab} *for* $E_{beam} = 11$ *GeV, and* E'_{lab} *vs* θ_{lab} *are depicted by the two plots on the left. On the right is shown the proposed concept for the primary acceptance collimator, which is able to achieve 100% acceptance with judiciously chosen* ϕ*-sectors.*

3.3.1 Kinematical Considerations

In the COM frame, the maximum asymmetry, the minimum differential cross-section and the maximum figure of merit occurs at $\Theta_{COM} = 90°$. A driving principle in the spectrometer design is to maximize acceptance for Møller scattering events in the full ϕ range and a large Θ range centered around $\Theta_{COM} = 90°$. This implies accepting a significant fraction of forward ($\Theta_{COM} < 90°$) and backward ($\Theta_{COM} > 90°$) Møller-scattered electrons. A nice feature of Møller scattering is the energy-angle correlation: there is a one-to-one correspondence between Θ_{COM} and the laboratory frame scattered electron energy E'_{lab}. The energy-angle correlation also implies that there is a one-to-one correspondence between E'_{lab} and θ_{lab}. These features are depicted in the two plots on the left of Fig. 11.

The proposed design aims to accept *all* (forward and backward) Møllers in the range $60° \leq \Theta_{COM} \leq 120°$, which implies that one must accept scattered electrons over a wide range of momenta. Thus, θ_{lab} and E'_{lab} ranges for forward Møllers are 5.5 to 9.5 mrad and 5.5 to 8.25 GeV respectively, and the corresponding ranges for backward Møllers are 9.5 to 17 mrad and 2.75 to 5.5 GeV. This is depicted by the colored regions in the two plots on the left of Fig. 11.

We have found a way to get 100% azimuthal acceptance with a toroidal geometry which is specific to identical particle scattering. This is depicted in Fig. 11 on the right, which shows the primary acceptance collimator concept (situated 6 m downstream of the target along the beam axis). The idea is to accept both forward and backward Møllers in each ϕ bite, by accepting particles between $5.5 \leq \theta_{lab} \leq 17$ mrad. Since we are dealing with identical particles, those that are accepted in one ϕ bite also represent all the statistics available in the ϕ bite that is diametrically opposed $(180° + \phi)$. In the figure, each clear ϕ sector is diametrically opposed by a shaded region, which would be shielded from the target and can be used to house magnet coils without any loss of acceptance. The arrows point to regions that contain the two Møller electrons from the same events. In principle, any odd number of coils configured uniformly in ϕ would work; in the following, we describe our current design which contains 7 coils.

3.3.2 Conceptual Design

We itemize the principal requirements of the spectrometer/collimator system:

- Full azimuthal acceptance for Møller electrons in the momentum range between 2.5 and 8.5 GeV.
- Clean separation from the primary background of elastic and inelastic electron-proton scattering.
- Placement of detectors out of the line-of-sight of the target.
- Clean channel for the degraded beam and the bremsstrahlung photons to the beam dump.
- Minimization of soft photon backgrounds by designing a "two-bounce" system via judiciously placed collimators.

As discussed earlier, the selected Møller electrons represent a significant range in lab angle and energy and emerge from a very long (1.5 m) target. Minimizing background rates to an acceptable level requires bringing these very different trajectories, from a large region of phase space, into a tight radial focus separated from the majority of the principal backgrounds. The solution is a combination of two toroidal magnets which together act in a non-linear way on the charged particle trajectories. The first is a conventional toroid placed 6 m downstream of the target and the second, a novel hybrid toroid placed between 10 and 16 m downstream of the target. Each of the two toroidal fields is constructed out of seven identical coils uniformly spaced in the azimuth.

The action of the spectrometer can conceptually be divided into a radial and an azimuthal part. In the radial dimension, the successful interaction of the two magnets is key. The total $Bd\ell$ of the first magnet is small and thus the effect on the high-energy, low-angle Mollers is small. More importantly, the lowest energy, highest angle Møller electrons are bent even further away from the beamline, allowing these particles to skirt the strongest field in the second magnet.

The hybrid toroid is in some sense the heart of the spectrometer concept. It is designed so that particles at different radial distances from the beam feel *very* different integral $Bd\ell$. This allows the hard, low angle Mollers to be bent strongly to the radial focal position while the soft, high angle particles are merely 'tickled' into place. This concept can best be seen in Fig. 12.

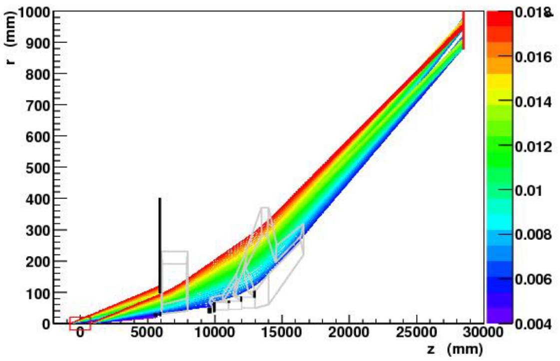

Figure 12: *Projected radial coordinate of scattered Møller electrons trajectories. Colors represent θ_{lab} (rad). The spectrometer coils (grey) and collimators (black) are overlaid.*

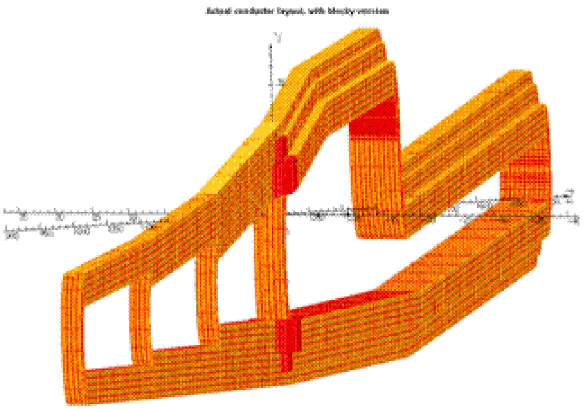

Figure 13: *Single hybrid coil with actual conductor layout, with 1/10 scale in the z direction.*

Table 3: *Summary of the coil parameters. The size of the conductor is 0.2294” (square) with a water-cooling hole of 0.128” (ID, round) and 0.08 mm of insulation (0.04 mm half-lapped).*

Mechanical Properties			Electrical Properties	
L_{turn} (m)		15, 13, 11, 9	R_{coil}	0.741 Ω
# turns		20, 8, 12, 36	V_{coil}	285 V
weight_{coil} (lbs)		555	I_{wire}	384 A
Magnetic forces (lbs)	F_r	-3000	P_{magnet}	765 kW
	F_ϕ	0	$\vec{J}$	1551 A/cm^2
	F_z	-50	Field Integral	1.1 T·m

In the azimuthal dimension, the lower energy electrons are strongly defocussed by radial fields in the hybrid toroid and bend around into the regions behind the blocked portions of the primary acceptance collimator. By the time the electrons reach the detector plane 28.5 m from the target, the full range of azimuthal angles is populated by Møller electrons. The effect of this behavior is that the energy distribution of detected electrons changes along the azimuth. This azimuthal segmentation provides a variety of additional ways to understand the detector response, the modeling of the spectrometer optics and the estimates of the background fraction.

3.3.3 Hybrid Coil Design

In order to achieve the field configuration needed to focus the large range of electron scattering angles and momenta, each coil in the hybrid toroid has four current return paths, as shown in Fig. 13. The upstream parts of the magnet have lower currents because they have fewer turns, with the fourth, most downstream part of the magnet having the full amount of the current (see Table 3). This optimizes the field seen by the lowest angle scattered electron tracks to ensure that the Møller and elastic e-p electrons have sufficient radial separation so that only the Møller electrons (which have a lower momentum) see the full field in the most downstream part of the magnet. The current return paths are also optimized to focus the largest angle (lowest momentum) Møller tracks so that they only experience field for a short distance in the magnet, which results in a negative curvature in the downstream part of the coil. The details of the conceptual design, Monte Carlo studies and preliminary studies of the mechanical design are presented in App. C

3.4 Detectors

The toroidal spectrometer will focus the Møller electrons $\approx$ 28 m downstream of the target center onto a ring of $\approx$ 1 m radius and $\approx$ 10 cm thickness. As can be seen in Fig. 14 which shows the transverse distribution of the scattered electron flux at the detector plane from a Monte Carlo simulation, both the Møller electrons (black points) as well as the more rigid electrons from elastic electron-proton scattering (red points) form rings; the latter ring is at a smaller radius of $\approx$ 70 cm. The primary acceptance collimator is divided into seven sectors uniformly distributed in the azimuth, covering exactly one-half the azimuth as described in Sec. 3.3 above.

Due to azimuthal defocusing in the magnets however, the Møller electrons populate the full range of the

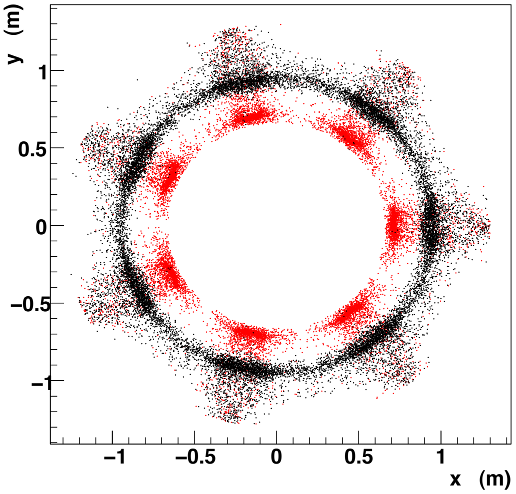

Figure 14: *Transverse distribution of Møller (black) and ep (red) electrons 28.5 m downstream of target*

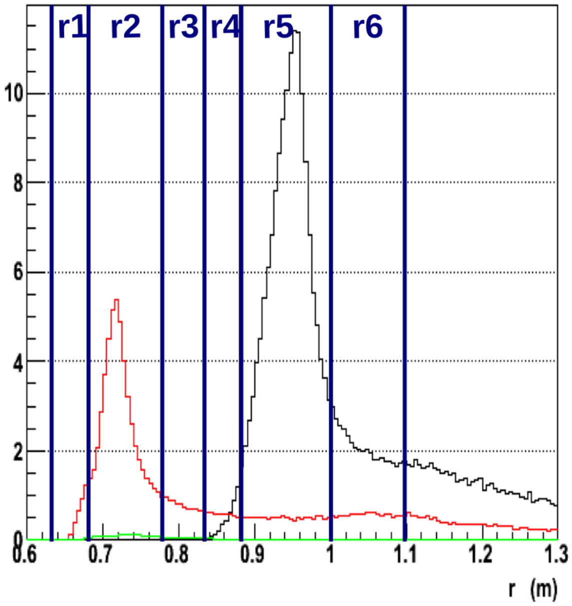

Figure 15: *Radial distribution of Møller (black) and ep (red) electrons 28.5 m downstream of target.*

azimuth at the detector plane. It can be seen in Fig. 14 that stiffer tracks from electron-proton scattering at smaller radii do not defocus as much; gaps can be seen in the azimuthal distribution interspersed with areas of high density. Nevertheless, in the event distribution one can identify separate Møller and "ep" peaks along any radial cut, as shown explicitly in Fig. 15. The figures demonstrate that a detailed understanding of the signal, background fraction and spectrometer optics requires detector segmentation in both in the radial and azimuthal dimensions; the six radial bins chosen are explicitly shown in Fig. 15.

For the primary A_{PV} measurement, the detector response will be integrated over the duration of each helicity window to measure the scattered flux. The detectors must measure the relative flux in the nominal acceptance, contribute negligible noise relative to the counting statistics of the signal, and be radiation-hard. Because the tail of all radiative electron-proton elastic and inelastic processes results in an important systematic correction, the detector must also be able to measure these background electrons in *several* bins so trends in yield and asymmetry can be compared to simulations. The detector must be insensitive to soft backgrounds, minimize cross-talk between adjacent radial bins with widely different asymmetries, and not possess large biases between electron tracks which impact the detectors at different positions and angles. Additionally, event-mode acquisition at much lower beam currents for systematic studies is also required.

The ideal detector material is artificial fused silica (henceforth "quartz"), since it is radiation-hard, and has negligible scintillation response. As we describe in the following, the region between a radius of 0.6 to 1.1 m will be populated by a series of detectors with radial and azimuthal segmentation. These detectors will measure A_{PV} for Møller scattering and equally important, also for the irreducible background processes of elastic and inelastic electron proton scattering.

Quartz detectors at very forward angle will monitor window to window fluctuations in the scattered flux for diagnostic purposes. Lead-glass detectors placed behind the main Møller ring detectors and shielding, combined with two planes of gas electron multipliers (GEMs) will measure hadronic background dilutions and asymmetries. Finally, three planes of GEM tracking detectors will be inserted periodically at very low current to track individual particles during calibration runs to measure the detailed shapes of all the charged particle trajectories.

An overview of the main detector systems is shown in Fig. 16. We will describe various components in the following subsections.

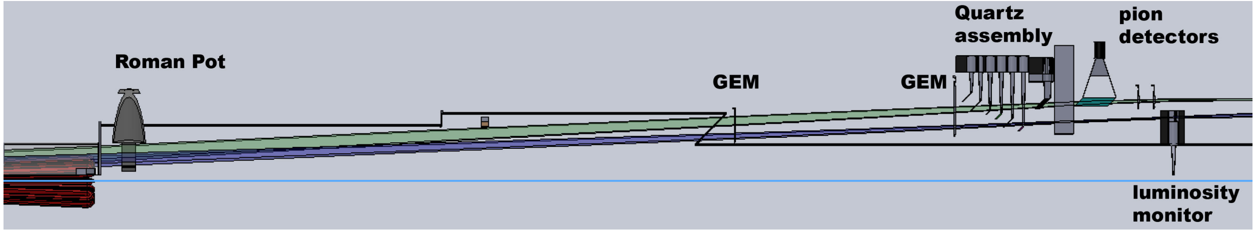

Figure 16: *Layout of the main integrating and tracking detectors. Elastically scattered electrons off target protons (blue) and electrons (green) are also shown.*

3.4.1 Main Integrating Detectors

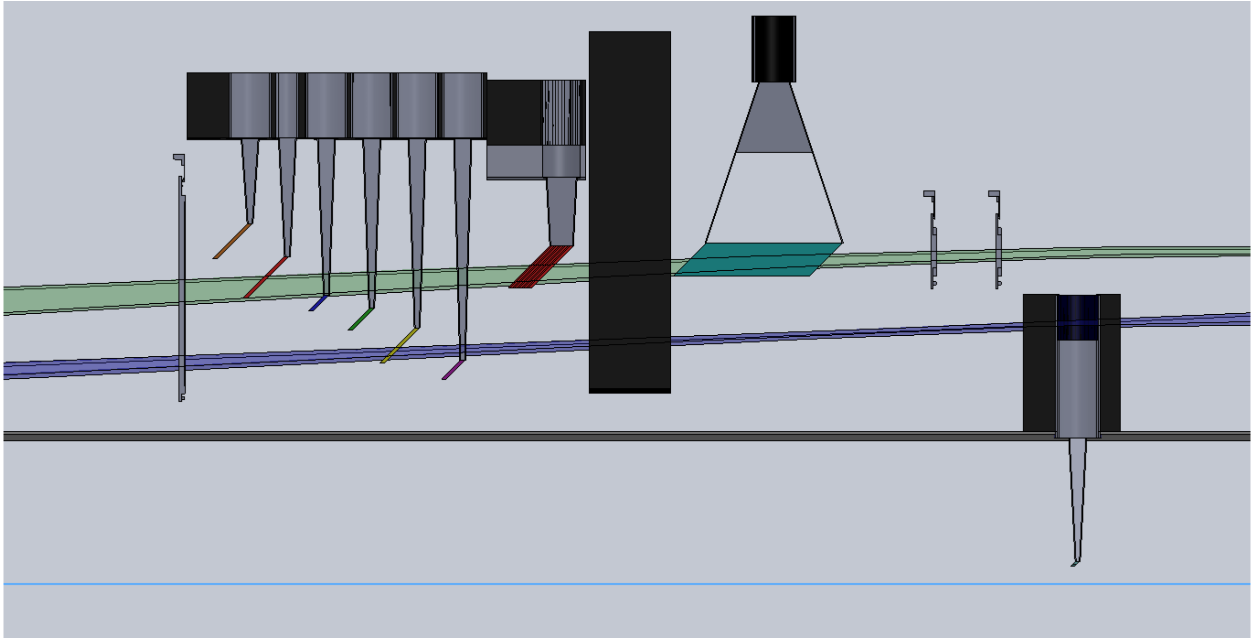

Figure 17: *Plan cutaway view, along with the main elastic Møller (green) and ep (blue) trajectories. The quartz detectors are color coded. The main Møller events predominantly hit the red quartz, while the elastic ep trajectories hit the yellow quartz. The blue and green detectors in between will be important to estimate the inelastic ep background correction; see Sec. 4.5.2. Note the two back-to-back red detectors that will simultaneously measure the flux of the Møller peak.*

The scattered electrons will be intercepted, after they exit the vacuum, by a set of thin quartz plates arranged radially as shown in Fig. 17. Each plate is angled with respect to the electron trajectories such that it is aligned with a section of the electrons' Cherenkov cones, allowing a significant number of photons to traverse along the quartz and exit the end of the plate along the outer radius.

The quartz thickness along the beam direction is optimally around 1 cm. A thinner detector does not produce enough photoelectrons while a thicker detector would have unacceptably large Landau tails, ruining the average RMS of the photoelectron distribution for single electrons [35]. The total number of photoelectrons exiting the quartz for a single electron is significantly enhanced by additional photons that undergo total internal reflection. The photons are directed along a light guide to a photomultiplier tube, whose integrated response is a measure of the scattered electron flux [36].

The six radial bins (shown explicitly in Fig. 15) have been optimized to measure the main Møller scattering asymmetry as well as the asymmetries in the scattered electrons from the background processes of elastic and inelastic scattering from target protons. A discussion of this optimization can be found in Sec. 4.5. Azimuthal segmentation is also useful since defocusing due to radial fields in the toroidal spectrometer results in a correlation between azimuthal angle and E'. Each azimuthal sector defined by one of the toroids is therefore further divided into 4 sub-sectors, so that there are 28 total azimuthal channels at each radial bin.

Having sufficient photoelectrons and having the maximum possible azimuthal segmentation is critical for the main Møller "peak" radial bin (red). The azimuthal segmentation is therefore finer by a factor of 3, for a total of 84 channels. Some additional considerations regarding these main integrating detectors are discussed in App. D. Additionally, a "shower-max" quartz/tungsten sandwich detector will provide a second independent measurement of the flux in the main Møller "peak". This detector will be less sensitive to soft photon and charged hadron backgrounds. Figure 18 shows how radial and azimuthal segmentation is achieved with a compact mechanical construction.

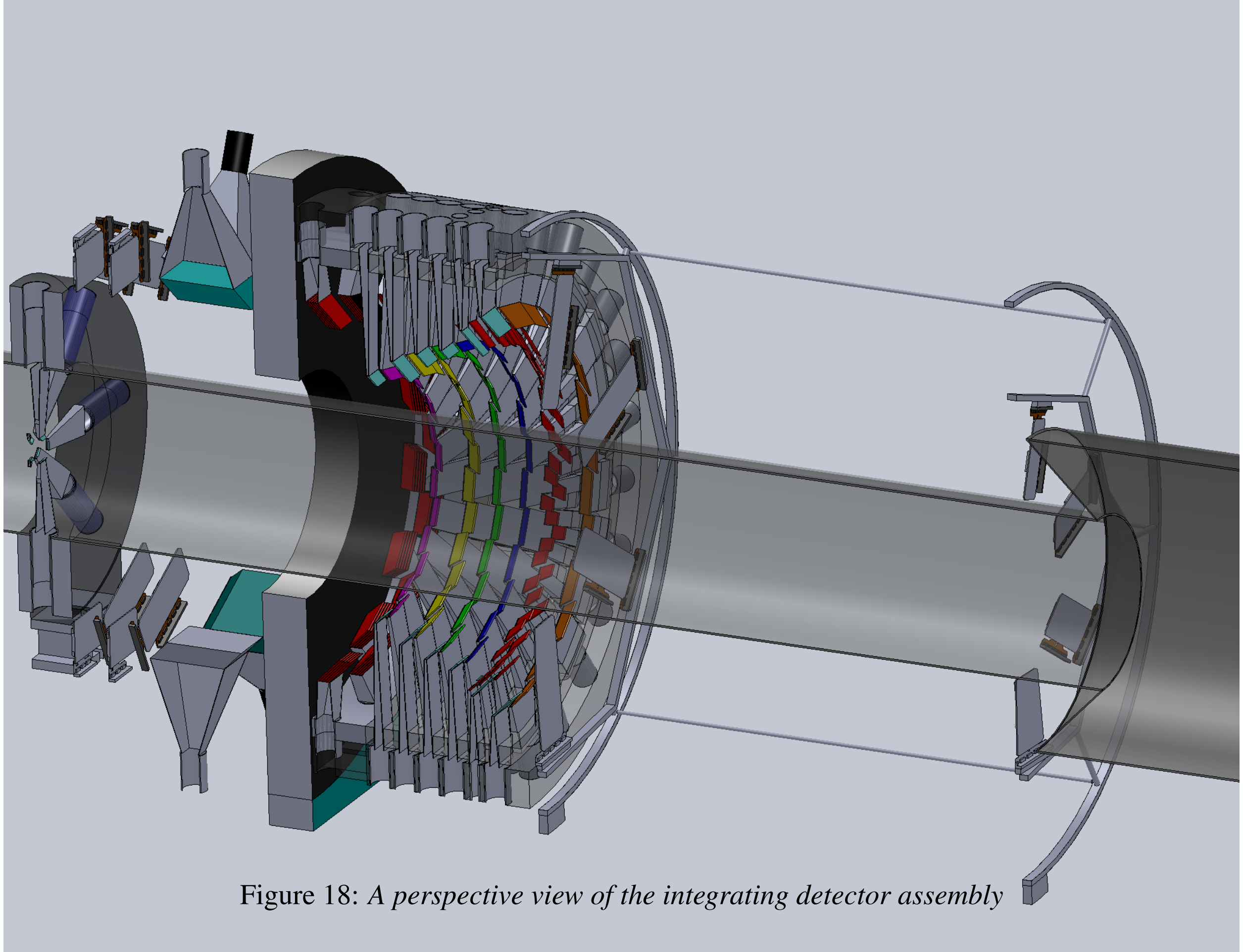

Figure 18: *A perspective view of the integrating detector assembly*

3.4.2 Auxiliary Detectors

In the vicinity of the Møller “peak”, there is a possibility of a small ($\sim 0.1\%$) contamination from pions and other charged hadrons. The background could result from processes with a very tiny cross-section with a potentially large analyzing power, as discussed in Sec. 4.5.3. It is therefore important to be able to directly measure both the dilution fraction as well as the parity-violating asymmetry of this background.

We propose to accomplish the dilution fraction and asymmetry measurements with a set of auxiliary detectors that will be placed along the primary Møller ”peak” trajectory behind shielding. The idea is to identify minimum ionizing particles (MIPs) that penetrate the shielding using a Pb-glass calorimeter, followed by two GEM planes to positively identify charged particles (see Fig. 17).

The dilution measurement will be carried out in an auxiliary calibration run at very low current, where pions will be identified by looking for MIP signals in both the Møller ”peak” sandwich detector as well as the Pb-glass detector, both in time coincidence with a track from the two downstream GEM detectors. The asymmetry measurement would be carried out during production running. Two methods are being investigated: either integrating the Pb-glass signal or designing a fast-counting electronics chain that establishes a coincidence between a Pb-glass MIP signal and a GEM track.

The final detector at the right edge of Fig. 16 is the so-called ”luminosity monitor”, which consists of quartz detectors that will detect the charged particle flux at extreme forward angles. Such monitors have two purposes. Since they have higher statistics (by a factor of 5 to 10) than the primary Møller flux, they serve as a sensitive diagnostic of target density fluctuations, beam fluctuations and electronics noise. The small scattering angle also implies that they should have a much smaller parity-violating asymmetry, so that they can also serve as a ”null asymmetry monitor”.

In the current spectrometer design, we have determined that the forward angle charged particle flux in the $\theta_{\rm lab}$ range between 2 and 2.5 mrad should not feel any fields. We therefore plan to instrument the region between 6.0 and 7.5 cm thirty meters downstream of the target with eight luminosity detectors; the detection technique will be similar in concept to the main integrating detectors i.e. a thin quartz plate with an associated air light guide and photomultiplier tube. The placement of these detectors can be discerned from Figs. 17 and 18.

3.4.3 Tracking Detectors and Scanner

In order to verify the spectrometer optics, to measure the absolute value of Q^2 and to evaluate our understanding of backgrounds, a tracking system is proposed to be used at very low current ($\sim$ 100 pA). The basic concept is to measure particle tracks using 3 GEM planes downstream of the two spectrometer toroids but before the particles arrive at the main integrating quartz detectors.

One plane would be just downstream of the hybrid toroid and two planes would be placed $\sim$ 3 m apart just upstream of the main detectors, as shown in Fig. 16. Since the first plane of GEMs must be made insertable in the vacuum space downstream of the hybrid toroid, we are investigating the use of the concept of “Roman pots”, so that the GEMs themselves can be operated in air. The two downstream GEM planes must be insertable to intercept the charge particle flux after they exit the vacuum window. In order to reduce costs, we propose to cover 25% of the cross-sectional area traversed by the beam with GEMs with seven planes distributed uniformly in the azimuth and have them attached to a remotely controlled “wheel” with the ability to rotate about one-seventh of 2π.

We expect that a resolution of $\sim$ 250 μm for a flux of $\lesssim$ 200 Hz/cm^2 will be required at the proposed operating beam current of 100 pA, which should not be too taxing for established readout techniques for GEMs. The ability to stably deliver such a low-current calibration beam for similar tracking measurements has been demonstrated in the Qweak experiment, which similarly relies on using a tracking system for background and kinematics measurements, at a beam current 6 orders of magnitude lower than that used for the primary asymmetry data-taking.

Another useful diagnostic will be a simple, small, movable detector that can operate at both the full beam flux and at the low beam currents needed for the tracking measurements. This "focal plane scanner" would consist of a small single Cerenkov detector made of fused silica, read out by PMTs, mounted on an x, y motion stage covering one sector of the acceptance, and located just upstream of the main detectors. Such scanners have been used in E158, HAPPEx-II, and one is now being used by Qweak.

This device can be used to confirm that the rate distribution as measured at low beam currents by the full tracking system is not significantly different than that seen at full luminosity. It also would allow periodic rapid monitoring of the distribution during production data-taking, to ensure stability of the effective kinematics and to any changes in backgrounds.

3.5 Electronics and Data Acquisition

The integrated response of the Cherenkov light from electrons that traverse the detector is linearly proportional to the scattered flux. The parity-violating asymmetry is measured by averaging the fractional difference in the response of the detectors F over many window-pairs:

$$A_i \equiv \left(\frac{F_R - F_L}{F_R + F_L}\right)_i \simeq \left(\frac{\Delta F}{2F}\right)_i; \quad A_{\mathrm{r}aw} = \langle A_i \rangle; \quad \delta(A_{\mathrm{r}aw}) = \sigma(A_i)/\sqrt{N}. \tag{8}$$

Here, A_i is the asymmetry in the ith window-pair, made from nearby (in the time domain) windows of opposite helicity. There are several aspects of the electronics and data acquisition (DAQ) specific to parity-violation experiments that are worth emphasizing, and we discuss them in the subsequent sections. The collaboration has extensive experience in these aspects of the experimental technique.

3.5.1 Rapid Helicity Flip

Second generation parity violation experiments at Jefferson Lab such as HAPPEX-II used a helicity reversal frequency of 30 Hz, which had the benefit of largely canceling beam jitter and electronics noise related to 60 Hz line. PREX ran successfully with 240 Hz helicity-reversal, while Qweak used 960 Hz reversal. It will be necessary for MOLLER to flip the helicity even more quickly. One reason as mentioned above in the discussion of the target, is that target density fluctuations are only expected to contribute at frequencies below a few hundred Hz.

More importantly, at the MOLLER event rate of ~ 150 GHz, electronics noise is a very severe challenge. At a helicity flip rate of 60 Hz, the variance $\sigma(A_i)$ would be 28 ppm. A pedestal noise level below 3×10^{-6} would be required in order to ensure negligible contribution to $\sigma(A_i)$. We are designing around a flip rate of 1.92 kHz, such that $\sigma(A_i)$ would be 80 ppm. This requires a pedestal noise floor of 1×10^{-5}, which appears feasible. It also implies that each helicity state is held for $\sim 500\mu$s. In order to avoid excess noise from 60 Hz line variations, a scheme for selecting helicity states will be required which will force complementary pairs at corresponding points in the 60 Hz cycle.

The goal is to flip the Pockels cell within 10 μs, which implies a dead time of 2%. At present, a settling time of 60 μs is achievable for reversal rates of 960 Hz. However, it has proven difficult to push the transition of the Pockels cell to be shorter than 60 μs while keeping the cell optical properties stable after the shock of the fast transitions. The collaboration is exploring modifications to the switching or damping of oscillations, the use of a different Pockels materials such as RTP (which are not piezoelectric and therefore do not experience mechanical shock on transition), and the use of Kerr cells in place of Pockels cells.

3.5.2 Integrating Electronics

At the high helicity flip rate of 2 kHz, the low noise electronics developed for the Qweak experiment by TRIUMF should be suitable for MOLLER with little or no modification. The Cherenkov light from the quartz travels down a light guide and is then converted to a current by a photodetector. This would be converted to a voltage signal by a transimpedence preamplifier located close to the detectors. The voltage signals from all the quartz detectors would go to electronics outside the Hall where it would be sampled at a 500 kHz rate by an 18-bit analog-to-digital converter (ADC). These digitized samples would be integrated over each helicity window by an internal field-programmable gate array (FPGA). These considerations are described in more detail in App. E.

The main scattered electronic flux detectors are not the only parameters that must be integrated over each helicity window. Even with perfect electronics, $\sigma(A_i)$ in Eqn. 8 would be dominated by fluctuations in electron beam parameters due to window-to-window fluctuations in intensity, position, angle and energy. To exploit the full available statistics one must remove the correlations of F to beam intensity, position, angle and energy, thus extracting the measured raw asymmetry as follows:

$$A_i = \left(\frac{\Delta F}{2F} - \frac{\Delta I}{2I}\right)_i - \sum\left(\alpha_j(\Delta X_j)_i\right). \tag{9}$$

Here, I is the time-averaged beam intensity over the duration of a helicity window, X_j are corresponding average beam trajectory parameters derived from judiciously placed beam position monitors and $\alpha_j \equiv \partial F/\partial X_j$ are coefficients that depend on the kinematics of Møller scattering as well as the detailed spectrometer and detector geometry of the given experiment. The parameters I and X_j will be derived from monitor signals in much the same way as the relative flux F, by feeding voltage outputs that are proportional to beam parameters into the same ADCs. It is critical to maintain close synchronization between the integration cycles of all the ADCs.

3.5.3 Online Calibrations and Feedbacks

The coefficients α_j must be continuously calibrated *simultaneously* with the collection of production data, since the numerical values depend on the details not only of the apparatus but also the accelerator beam tune and the sensitivity and location of beam monitoring devices. Various ways of accomplishing this at Jefferson Laboratory have already been implemented during HAPPEX and G0 measurements, including extensive collaboration with personnel from Accelerator Operations and careful consideration of impact on other Halls.

While α_j can be extracted from a correlation analysis of the response of the detectors and beam monitoring devices to beam fluctuations in window-pairs, proper calibration requires deliberately dithering the beam trajectory concurrent with data-taking in a quasi-continuous fashion by an amount large enough to observe all the correlations while avoiding to add a non-statistical component to $\sigma(A_i)$. More generally, the study of the detailed noise and beam response characteristics of the monitors is a critical component of understanding the systematics.

The success of the experimental technique will also depend on careful preparation of the initial polarization states of the electron beam, which begins with a careful setup of the laser transport electronics of the polarized source. During data collection, there will be extensive electronic communication with optical and magnetic devices at the low energy end of the machine as various automated feedback loops of varying time frequencies will have to be incorporated. These systems will have to be implemented while paying careful attention to potential electronic cross-talk problems for which the proposed measurement will have sensitivity at an unprecedented level. Again, the collaboration has extensive experience on this aspect of the measurement. Details on the considerations in this subsection can be found in App. A.

Error Source	Fractional Error (%)
Statistical	**2.1**
Absolute value of Q^2	0.5
beam (second order)	0.4
beam polarization	0.4
$e + p(+\gamma) \to e + X(+\gamma)$	0.4
beam (position, angle, energy)	0.4
beam (intensity)	0.3
$e + p(+\gamma) \to e + p(+\gamma)$	0.3
$\gamma^{(*)} + p \to \pi + X$	0.3
Transverse polarization	0.2
neutrals (soft photons, neutrons)	0.1
Total systematic	**1.1**

Table 4: *Summary of projected fractional statistical and systematic errors.*

3.6 Hall A Infrastructure

The apparatus depicted in Fig. 8 and related shielding will be designed so that MOLLER runs can be interleaved with other experimental programs in Hall A. A first-order check of the experiment layout in Hall A has been done and no major obstructions have been found. The layout has both Hall A High Resolution Spectrometers (HRSs) parked at 90° to the beam line. Moving from the beam entrance along the beam line towards the dump, one would encounter the cryogenic target approximately 7 m upstream of the nominal pivot, the first spectrometer toroid at the HRS nominal target pivot, followed shortly thereafter by the hybrid toroid and, with the detectors approximately 19 m downstream of the pivot. Møller events and the degraded beam travel under vacuum all the way to the detectors and beam dump, respectively.

Cooling of the collimators and room temperature spectrometer toroids will be done using a closed low conductivity water (LCW) circuit to contain the beam activated water in the hall. A heat exchanger will transfer the heat from the closed system to the JLab wide LCW system. An additional 1 MVA electrical transformer would be added to handle the load brought by the spectrometer toroids.

A one meter thick concrete wall will cover most of the spectrometer length to minimize radiation in the Hall. Guidance from JLab's Radiation Control group will be sought concerning various radiological issues brought up by this experiment, such as how best to handle the disassembly and storage of activated parts for a multi-year experiment with other experiments taking place in between MOLLER runs.

With the target significantly upstream of the HRS pivot, existing beam optics elements are too close to be effective. A detailed plan for configuring the upstream magnetic and beam diagnostic elements has been formulated, but final implementation awaits the final design of the spectrometer/collimator system.

4 Systematic Control

The proposed A_{PV} measurement in some sense constitutes a fourth generation parity-violation experiment at Jefferson Laboratory. Apart from the obvious challenge of measuring a raw asymmetry with a statistical error less than 1 ppb, an equally challenging task is to calibrate and monitor the absolute normalization A_{PV} at the sub-1% level. The collaboration continues to gain extensive experience on all aspects of such measurements as work continues on executing the third generation experiments PREX [32] and Qweak [33].

We tabulate our estimates of the most important systematic errors in decreasing order of importance

Beam Property	Assumed Sensitivity	Accuracy of Correction	Required 1 kHz random fluctuations	Required cumulative helicity-correlation	Systematic contribution
Intensity	1 ppb / ppb	$\sim$1%	$<$ 1000 ppm	$<$ 10 ppb	$\sim$ 0.1 ppb
Energy	-1.4 ppb / ppb	$\sim$10%	$<$ 286 ppm	$<$ 0.7 ppb	$\sim$ 0.05 ppb
Position	0.85 ppb / nm	$\sim$10%	$<$ 47 μm	$<$ 1.2 nm	$\sim$ 0.05 ppb
Angle	8.5 ppb / nrad	$\sim$10%	$<$ 4.7 μrad	$<$ 0.12 nrad	$\sim$ 0.05 ppb

Table 5: *Goals for first order corrections from electron beam helicity correlations*

in Table 4. It is instructive to recall that the raw asymmetry is about 32 ppb and that the raw statistical error is 0.6 ppb or about 2%. In the following subsections, we describe some of the principal challenges of controlling systematic errors in the proposed measurement and provide justification for the projected errors in the table.

4.1 Beam Fluctuations

As described in Secs. 3.1 and 3.5, the scattered flux would be integrated over the duration ($\sim$ 500 μs) of each helicity window. Equation 9 shows how one then extracts a signal proportional to the raw cross-section asymmetry by removing beam correlations. In this section, we summarize the upper limits for the random and helicity-correlated fluctuations in order to achieve the systematic error goals in Table 4. Apart from active techniques to control helicity correlations in the laser beam as well as in the low energy electron beam, one also gains additional suppression due to so-called "adiabatic damping" and with the use of several methods of "slow helicity reversal". Many more details on these issues based on experience from past experiments can be found in App. A.

Numerical estimates for α_j were made using Monte Carlo simulation, with results which are similar to expectations based on scaling the beam-motion sensitivities measured in HAPPEX-II. They are listed in Table 5. Using these numbers, the required monitoring resolution to achieve counting statistics for 1 kHz window pairs is $\lesssim$ 3 μm in position, and 10 ppm in intensity. The position monitor resolution will be straightforward to achieve based on previous experience in HAPPEX-II, PREX and Qweak. On the other hand, achieving 10 ppm resolution in beam intensity will require significant R&D, which the collaboration has flagged for further study and effort.

4.1.1 Helicity-Correlated Beam Fluctuations

If one averages over the instantaneous pulse-pair asymmetry A_i (see Eqn. 9 in Sec. 3.5.2) and considers the cumulative experimental asymmetry A_{raw} over many window pairs i, one can write

$$\begin{aligned} A_{\rm raw} \equiv \langle A_i \rangle &= \left\langle \left(\frac{\Delta F}{2F} \right)_i \right\rangle - \left\langle \left(\frac{\Delta I}{2I} \right)_i \right\rangle - \sum \alpha_j \Big\langle (\Delta X_j)_i \Big\rangle \\ &= A_F - A_I - \sum_j A_{Mj}. \end{aligned} \tag{10}$$

In a well-designed and well-executed high flux parity experiment, the helicity-correlated beam asymmetries (HCBAs) A_I and ΔX_i will be small enough so that $\langle A_{raw} \rangle \simeq \langle A_F \rangle$, even though $\sigma(A_F)_i$ will be significantly larger than $\sigma(A_{raw})_i$ for window-pairs.

The first goal is to ensure that each correction A_{Mj} is of the order of, or smaller than the projected raw statistical error of about 0.6 ppb, and that the slopes α_j are known to better than 10%, so that the systematic error contributions from these corrections are small. This can in turn be transformed under reasonable assumptions to goals for the grand average ΔX_j. These considerations are summarized in Table 5. These are realistic goals, as we elaborate briefly in the following. During the relatively short HAPPEX-II experiment, position differences were kept to less than 2 nm and angle differences to less than 0.2 nrad; only a modest improvement over these goals is required. The more recent experience with the PREXI experiment has been similarly good, and improved performance is expected in the final runs of Qweak and PREXII. Table 6 summarizes the experience of recent, ongoing and future parity experiments on the measured HCBAs.

Selected parity experiments and their measured or projected demands on
suppression of helicity-correltated beam-parameter differences

Experiment (*) actual (†) projected	physics asymmetry	stat. error	sys. error due to beam	limits on position differences	limits on angle differences	limits on diameter differences
*HAPPEX I	-15,050 ppb	980 ppb	$\pm 20\,\text{ppb}$	$< 12\,\text{nm}$		
*SLAC E158	-131 ppb	14 ppb	$\pm 3\,\text{ppb}$	$< 12\,\text{nm}$	$0.4\,\text{nrad}$	$< 10^{-5}$
*HAPPEX II-p	-1,580 ppb	120 ppb	$\pm 17\,\text{ppb}$	$< 1.7\,\text{nm}$	$0.2\,\text{nrad}$	
*HAPPEX III	-22,100 ppb	550	$\pm 66\,\text{ppb}$	$< 40\,\text{nm}$		
*PREX-I	657 ppb	60 ppb	$\pm 7.2\,\text{ppb}$	$< 4.0\,\text{nm}$		$< 10^{-4}$
Upcoming or ongoing parity experiments						
†PREX-II	500 ppb	15 ppb	$\pm 3.0\,\text{ppb}$	$< 1.0\,\text{nm}$		$< 10^{-4}$
†Qweak	-288 ppb	5 ppb	$\pm 1.4\,\text{ppb}$	$< 2\,\text{nm}$	$30\,\text{nrad}$	$< 7 \times 10^{-3}$
† 12 GeV Møller	36 ppb	0.6 ppb	$\pm 0.05\,\text{ppb}$	$\sim 0.5\,\text{nm}$	$0.05\,\text{nrad}$	$< 10^{-5}$

Table 6: *Shown are various parameters for several parity experiments, including HAPPEX I, E158, and HAPPEX II-p, that are published, HAPPEX III and PREx, the results of which are available, and QWeak, that is ongoing. Also shown are PREx-II, recently approved, and MOLLER. The second and third columns show the actual measured or projected asymmetries and statistical errors. The fourth column shows the actual or projected error associated with corrections for helicity-correlated beam-parameters. The remaining columns indicate actual or projected limits on helicity-correlated beam parameter differences.*

Extensive tools for tightly controlling A_I have been developed in previous experiments. The nonlinearity between the detectors and beam current monitors is typically controlled at the 0.5% level. Given the goal of 0.1 ppb contributed error from intensity corrections, this implies that the grand average A_I must be smaller than 10 ppb. Intensity feedback will be employed to assure convergence within that bound.

A large degree of cancellation for the slopes α_j is expected when considering the full azimuthal symmetry of the detector. A conservative estimate of a factor 10 reduction in sensitivity is taken to account for detector alignments tolerances. After applying corrections for small position and angle differences, an uncertainty of approximately 10% is likely to remain. This leads to the specifications for the run-averaged ΔX_j in order to keep the contributed uncertainty to less than 0.05 ppb each, as listed in Table 5.

4.1.2 Beam Spot Size Differences

In all the discussion above on beam-related systematic effects, it has been assumed that the dominant component in the scattered flux response to fluctuating parameters is linear. In practice, it is possible that certain second-order effects might be helicity-correlated and thus lead to systematic shifts. The stability of the CEBAF beam makes it highly unlikely that there are large effects, and none have been seen in experiments to date. Typically, second-order effects tend to scale as a fraction of the first-order effects, providing additional incentive to control the first-order effects as tightly as possible. Furthermore, the $g-2$ and "double-wien" slow reversals (discussed in Sec. A.4) will be powerful cross-checks of this assumption.

One common manifestation of a second-order effect is a helicity-correlated difference in the beam spot-size σ. We have simulated the effect for the proposed spectrometer/collimator geometry, finding it to be at the level of (12 ppm)$\times\Delta\sigma/\sigma$. Work on the laser table should be able to bound the laser spot size asymmetry to be less than 10^{-4}, in which case the potential effect would be as large as 1 ppb. We assume a factor of 10 suppression from cancellation due to the proposed periodic slow helicity reversals, so that the net contribution will be limited to 0.1 ppb.

4.2 Longitudinal Beam Polarization

The experiment requires a relative accuracy of the electron beam polarization measurement at the level of 0.4%. A comparable level of accuracy has been previously achieved by the SLD collaboration [38] using a Compton polarimeter with a $\sim$ 46 GeV pulsed beam at SLAC. The electron beam polarization is expected to be between 80 and 90%, with the exact value depending on specific photocathode materials and a variety of other factors. There is also a long-held belief that the beam polarization might vary at the 0.5 to 1% level over the duration of a specific photocathode's lifetime. Thus, achieving 0.4% systematic control will require redundant, continuous monitoring during data collection.

JLab has accumulated extensive experience with polarimetry at or below 6 GeV. Recently completed and ongoing experiments in the JLab "6 GeV" program, in both Halls A and C (PREX, HAPPEXIII, PVDIS and Qweak), have developed 1% polarimeters. However, these polarimeters have never been cross-checked with each other at the level of 0.4%, nor has any experiment yet matched this level of precision on a beam polarization observable.

In order to reach a robust 0.4% accuracy, we propose to develop two separate, continuous polarimeters, each independently normalized to that level of accuracy. Each polarimeter should provide a 0.4% statistical precision in comparable time periods of not more than several hours, in order to facilitate cross-checks and systematic studies. This redundancy, both in the measurement and monitoring of the beam polarization, will provide a new benchmark in precision electron beam polarimetry. We discuss both polarimeters briefly in the following sections.

4.2.1 Compton Polarimetry

Compton polarimetry is a very attractive technique for high precision polarimetry with high energy electron beams. When electrons scatter off circularly polarized laser photons, the associated Compton cross-section depends on both the electron and photon polarizations. Beam interactions with a photon target are non-disruptive, so Compton polarimetry can be employed at high currents as a continuous polarization monitor. The photon target polarization can be measured and monitored with a very high precision, and the scattering between a real photon and free electron has no theoretical uncertainty, such as atomic or nuclear effects which can complicate other measurements. Radiative corrections to the scattering process are at the level of 0.1% and are very precisely known. The SLD result of 0.5% polarimetry demonstrates the feasibility of very high accuracy Compton polarimetry.

JLab Compton polarimeters employ a 4-dipole vertical chicane, just below the primary beamline. The interaction point is between the second and third dipoles, where the electron beam is parallel to the primary beamline but at a lower height. A Fabry-Perot cavity serves as the photon target. The scattered electrons lose energy and are separated by the third and fourth dipoles from the primary beam and are intercepted by position-sensitive detectors such as silicon microstrips. The scattered photons are detected by a calorimeter downstream of the third dipole. The electron polarization can be extracted independently by measuring the helicity-dependent rate of the electrons or the photons, and important systematics studies can be carried out by studying electron-photon coincidences. The existing Hall A Compton polarimeter will be upgraded for 11 GeV operation as part of the baseline energy upgrade project.

Based on the collaboration's experience with Compton polarimetry from the third generation experiments PREX and Qweak, we have estimated the systematic uncertainties that seem feasible for continuous

Relative error (%)	electron	photon
Position asymmetries*	-	-
E$_{Beam}$ and λ_{Laser}*	0.03	0.03
Radiative Corrections*	0.05	0.05
Laser polarization*	0.20	0.20
Background / Deadtime / Pileup	0.20	0.20
Analyzing power Calibration / Detector Linearity	0.25	0.35
Total:	0.38	0.45

Table 7: *Goals for systematic errors for the Hall A Compton polarimeter at 11 GeV. Topics marked * are a common systematic error between the photon and electron analyses, while the other are largely independent between the detector systems.*

monitoring at 11 GeV. These ambitious goals are summarized in Table 7. Additional modifications to the polarimeter, beyond the scope of the baseline upgrade, will be required to achieve this precision. The goal is to have an internal cross-check at the 0.4% level by comparing the extracted beam polarization from the scattered photons to that from the scattered electrons. Detailed considerations leading to the projected systematic errors can be found in App. F, and some immediate plans for R&D are described in Sec. 7.6.1.

4.2.2 Møller Polarimetry

Møller polarimeters exploit the helicity dependence of polarized Møller scattering $\vec{e^-} + \vec{e^-} \to e^- + e^-$ to extract the beam polarization by using a polarized electron target of known polarization. It has a very high analyzing power (about 80%), a very large count rate, and the two electrons with high energies in the final state make it easy to detect their coincidence and reduce background to negligible values. Such polarimeters have been in use for more than three decades and many potential systematic effects are now controlled at the sub-1% level.

There are two fundamental limitations to Møller polarimetry. First, it requires a polarized electron target whose degree of polarization must be known accurately. Second, it is a "destructive" measurement requiring the periodic insertion of the polarized target and measurements at a beam current of a few μA, thus precluding continuous polarization monitoring at high beam current. In the following, we briefly review the steady improvement in target polarization accuracy and then describe a proposed new technique that would allow continuous monitoring and dramatically improve target polarization accuracy. More details on these considerations can be found in App. G.

The most common polarized electron targets are ferromagnetic foils. The total polarization in fully magnetized iron is about 8% (~ 2.1 electrons in the d-shell of the Fe atom are polarized). The exact value cannot be calculated from first principles but must be derived from the measured magnetization. The best techniques have produced relative target polarization accuracy approaching 2%.

A significant improvement has been achieved by using fully saturated iron foils in a strong longitudinal field approaching 4 T. The magnetization is not measured but published data on the properties of bulk iron can be used to infer the foil polarization to an accuracy approaching 0.1%. There are are several additional corrections of the order of 0.5% that must be made, most notably involving temperature variations due to beam loading and also for extrapolation from low to high beam current. Table 8 shows the current and projected list of systematic errors for the technique of Møller polarimetry.

For MOLLER, the upgraded Hall A column of numbers is viewed as the backup plan. The main strategy

Variable	Hall C	Hall A		
		pre-2010	2010 upgrade	proposed
Target polarization	0.25%	1.50%	0.35%	0.01%
Target angle	0.00%	0.50%	0.00%	0.00%
Analyzing power	0.24%	0.30%	0.30%	0.10%
Levchuk effect	0.30%	0.20%	0.30%	0.00%
Target temperature	0.05%	0.00%	0.02%	0.00%
Dead time	-	0.30%	0.30%	0.10%
Background	-	0.30%	0.30%	0.10%
Others	0.10%	0.50%	0.50%	0.30%
Total	0.47%	1.8%	0.86%	0.35%

Table 8: *A list of systematic errors quoted for the Møller polarimeters in Hall C [39] and in Hall A. The present Hall C configuration is assumed. For Hall A, the first column shows the warm-magnet configuration used prior to 2010, the second column shows the results achieved with the the high-field target, Hall C style upgrade, while the last column shows the expectations for the polarimeter, equipped with an atomic hydrogen target. The regular, low beam current operation is assumed for all, but the last column, which is for operations at high beam currents, but less than* < 100 *μA.*

to avoid the limitations of conventional Møller polarimetry [40, 41] is to use polarized atomic hydrogen gas, stored in an ultra-cold magnetic trap, as the electron target. Such a target of practically 100% polarized electrons would remove the errors associated with the ferromagnetic targets, namely knowledge of the target polarization. The other errors such as the Levchuk effect, the analyzing power and the dead time can be strongly suppressed. Such a target is thin enough to be used continuously with the experiment. A 1% statistical accuracy can be achieved in less than 30 minutes of running.

The expected systematic error (see right column in Table 8) is below 0.4%. This will require a dedicated R&D effort. Although the technique of hydrogen trapping is well established, there is presently no experience in passing a high intensity beam through such a trap. We describe our near-term plans on the R&D in Sec. 7.6.2.

4.3 Transverse Beam Polarization

If there is any transverse polarization component to the beam on target, the apparent A_{PV} as a function of the azimuthal angle would show a modulation due to the vector analyzing power A_T in Møller scattering, a QED effect involving the interference between the tree-level amplitudes and the two-photon exchange amplitudes. The relevant parameter for A_T is the energy of each electron in COM frame, which is 53 MeV; the electron's boost factor is therefore rather modest. The magnitude of A_T is such that even a few percent transverse polarization can result in an azimuthal modulation of the measured polarization asymmetry that is an order of magnitude larger than A_{PV}. While this effect should cancel if one averages data over the full range of the azimuth, imperfect cancellation could lead to a significant systematic error.

Some interesting features of A_T facilitate a strategy that would allow us to keep this potential systematic error under control. If one looks at A_T as a function of the COM scattering angle, or equivalently $y \equiv 1 - E'/E$, one finds that A_T must vanish at $y = 1/2$, which corresponds to 90° scattering in the COM frame, due to CP symmetry. Thus, the maximum A_T is around 15 ppm, and occurs at $|y - 0.5| \approx 0.2$, at the very edges of the momentum acceptance and more importantly, A_T is of opposite sign at these two extremes. This leads to an order of magnitude suppression in the effective A_T averaged over all detectors.

It is possible by passive setup procedures to limit the transverse component of the beam polarization at the target to be less than 1°. One can measure the ϕ modulation to very high precision during production data collection within the first few hours, by studying the azimuthal dependence of the raw detector asymmetry, since different azimuthal detectors have very different acceptances as a function of y. Thus, it should be possible to devise a "manual" feedback loop that would make small tweaks to the launch angle of the electron beam polarization at the low energy end of the machine based on the measured A_T's. This technique is designed to converge to zero transverse polarization. In practice, the suppression should go like $1/N$, where N is the number of adjustments. In principle, we should gain a factor of about 25 below the setup accuracy of 1° in a week. We will assume this factor for the duration of the entire data collection period for the estimate of the systematic error.

If one now further conservatively assumes only a factor of 10 suppression in the grand average of A_{PV} over the full range of detectors, then the total systematic error from the correction to A_{PV} is less than 0.07 ppb. If this level of suppression is difficult to achieve in practice, some of it can be recovered by a slightly different reweighting of the data from the various different azimuthal detectors with only a small loss in the statistical error in the extracted A_{PV}.

4.4 Absolute Value of Q^2

For momentum transfers $Q^2 \ll M_Z^2$, A_{PV} at tree level is directly proportional to Q^2. The uncertainty in the Q^2-acceptance of the experiment therefore contributes directly to the ultimate uncertainty on Q^e_W. Our goal is to determine the average value of Q^2 in our detector acceptance to 0.5%. We will rely on the extensive experience that is being developed to measure Q^2 for Qweak. Also, sub-1% accuracy has been achieved in the HAPPEx measurements.

The average Q^2 can be determined from a detailed Monte Carlo integration of $Q^2 = 4EE' \sin^2 \theta/2$ over the acceptance, where E is the beam energy determined by Hall A energy measurement systems, E' is given by 2-body kinematics, θ is the electron laboratory scattering angle at the $e + e$ vertex, and events are weighted by the known $e + e \to e + e$ cross section. In the approximation where radiation in the target is neglected, Q^2 can be largely determined from survey measurements of collimator apertures and knowledge of the target location and length, and the absolute beam energy calibration tools in the Hall A beam line.

With the beam going through a 10.5 gm/cm^2 target however, the distribution of trajectories and energies are significantly modified. This requires not only a detailed Monte Carlo simulation but also validation by direct measurement of individual tracks in calibration runs at low current. This is one of the primary motivations for the tracking system discussed in Sec. 3.4.3. The large amount of multiple scattering, dE/dx and radiative losses due to the thick target, coupled with the large kinematic acceptance, and the rapid variation of the asymmetry with Q^2, means that the Monte Carlo simulation of the effective Q^2 seen by each detector segment needs to be validated carefully.

If the integrating quartz detectors cover the full acceptance of the events passing through the collimators, a precise survey of them would in principle provide an accurate measurement of the average Q^2. However a variation in the analog response of the integrating detectors would reweight the effective Q^2 of the integrated response. The aforementioned tracking system can evaluate this effect by measuring the variation in response as a function of position in the quartz using single Møller electron tracks at low beam currents.

4.5 Backgrounds

4.5.1 Elastic ep Scattering

The principal irreducible background under the Møller "peak" (see Fig. 19) is radiative elastic electron-proton (ep) scattering, which constitutes 8.3% of the signal. The background can be easily modeled and then verified explicitly with auxiliary tracking measurements of the radial profile of the scattered flux. The parity-violating asymmetry is also well known for this process. In addition, the Qweak measurement of the weak charge of the proton Q_W^p can be used directly to predict this background asymmetry.

After the modeling has been fine-tuned with calibration data, the Q^2 distribution of the background under the Møller peak can be estimated from the Monte Carlo simulation. The average Q^2 is 0.004 GeV^2. Assuming an uncertainty of 4% on the knowledge of Q_W^p, this leads to a 0.3% systematic error

4.5.2 Inelastic ep Scattering

A more challenging background correction is due to the smaller dilution from inelastic ep scattering. Even though the contribution from the background is expected to be small, $\lesssim 0.5\%$, the asymmetry correction can be significantly larger due to the fact that the estimated coupling to the Z boson is more than an order of magnitude larger than Q_W^e. Indeed, this background was studied in E158 and the parity-violating asymmetry from inelastic electron-proton scattering was consistent with the formula $0.8 \times 10^{-4} \cdot Q^2$[GeV^{-2}].

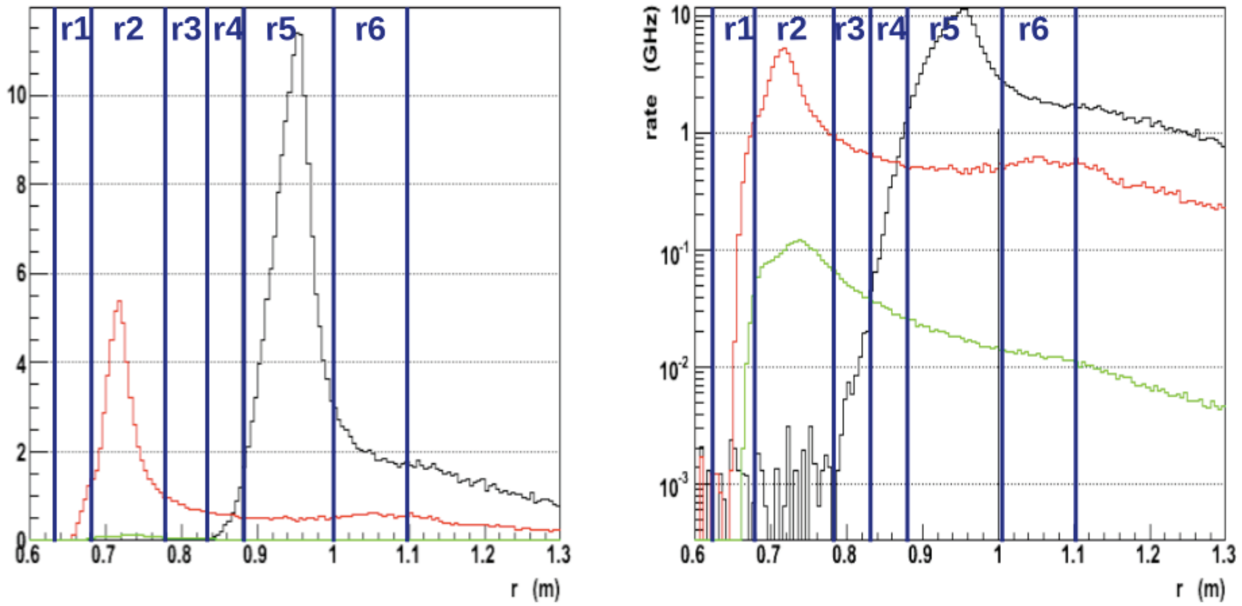

Figure 19: *Proposed radial segmentation of the scattered electron flux, shown both in linear and log scale. The vertical lines correspond to the radial segmentation of the quartz detectors as shown in Fig. 17. The black, red and green curves are for electrons from Møller, elastic e-p and inelastic e-p scattering.*

We have done a preliminary optimization of the radial segmentation of the integrating detectors that will allow us to measure the relevant combination of vector couplings and make a reliable background correction to the raw Møller asymmetry. The six different colors shown in Fig. 17 correspond to the six radial bins shown in Fig. 19, where the segmentation is overlaid on the Monte Carlo radial distributions for scattered Møller, elastic ep and inelastic ep electrons. The Møller electrons primarily hit the red quartz (r5) while the elastic e-p electrons predominantly hit the yellow quartz (r2).

The measured raw asymmetries in the green and blue detectors in between (r3 and r4) will be dominated by the inelastic ep parity-violating asymmetry. This is because the inelastic ep coupling is expected to be 20 times bigger than the elastic ep coupling, whereas the inelastic ep flux (green) is only 5 to 10 times smaller than the elastic (red) flux (see Fig. 19). Those measurements can be used to estimate the correction due to the inelastic ep background in the "red" detectors that contain the raw Møller asymmetry of interest. We make the assumption that the inelastic Z coupling is relatively constant in three different regimes of the recoiling hadron mass W: the Delta resonance, other resonances below 2 GeV, and the continuum above 2 GeV. A Monte Carlo study has demonstrated that we can reliably estimate the correction for the Møller detectors by studying the variation of the radial detectors as a function of the azimuth. We have concluded that we can make the estimated 4% correction to 10% of itself, leading to a 0.4% systematic error.

4.5.3 Hadrons and Muons

There is the possibility of pions, heavier hadrons and muons to contribute at a small level to the signal in the Møller detectors. The polarization asymmetry of this background will depend on the processes that create them. The dominant source is from pions produced by real and virtual photoproduction off protons in the target. This background was studied for the E158 configuration and was explicitly measured to be 0.12% in the Møller detector. The parity-violating asymmetry, measured in dedicated pion detectors that measured the hadronic leakage behind the Møller detector, was found to be ~ 0.5 ppm.

For the configuration of this proposal, a reasonable extrapolation from the E158 kinematics implies that the fractional background fraction will be fractionally about the same; the Møller cross section has gone up by a factor of 4, but the solid angle bite has also gone up by about a factor of 4. The asymmetry will likely be the same size, which would lead to a significant (~ 0.5 ppb) but manageable correction. However, it is possible to have a contribution from a fractionally tiny flux of pions or muons from weak decays of heavy baryons produced by electro- or photo-production in the target. If there is sufficient polarization transfer, the potentially large analyzing power in weak decays might lead to a sizable correction.

We have a preliminary concept for directly measuring the dilution factor as well as the parity-violating asymmetry in the hadron background with dedicated "pion" detectors described in Sec. 3.4.2. The collaboration plans further Monte Carlo studies of the kinematic acceptances of pions from weak decays. The results from these studies will be used to further refine the conceptual design of the "pion" detectors.

4.5.4 Photons and Neutrons

In a forward spectrometer of the type being discussed, it is very challenging to suppress neutral background from soft photons and neutrons. We will follow a strategy similar to E158, where neutron background was heavily suppressed by burying the photodetectors in a lead shield and we will follow a similar strategy here. We have taken a preliminary look at the collimation system and we believe that we can greatly suppress photon background, designing a near-perfect "two-bounce" collimation system. There will be at most one or two edges from which photons could reach one of the primary detectors after undergoing only one bounce from the taget. The flux at these edges will be rather modest compared to the signal flux.

Further suppression will be achieved for the auxiliary Møller detector made of alternating plates of quartz and tungsten i.e. a "shower max" detector. Based on previous experience and simulation, we anticipate suppressing this background at the level of a fraction of a percent and expect to make the correction with an error less than 0.1%. These backgrounds can be measured with special runs, such as by "blinding" the Cherenkov photodetectors and looking for the residual beam-correlated response, as well as runs with the spectrometer magnets turned off. Such backgrounds are not expected to have any polarization asymmetry.

5 Beam Time Request and Run Goals

While the MOLLER apparatus is being designed for a beam current of 85 μA at 11 GeV, we have assumed a beam current of 75 μA and a beam polarization of 80% to formulate the beam time request. If higher beam current and/or higher beam polarization are considered routine, the request can correspondingly be reduced using the appropriate P^2I factor. In order to ensure the technical success of this challenging measurement, we are proposing to take data in three separate run periods. These run periods have been optimized so that

Run Period	1kHz Width (ppm)	% Stat. Error	Stat. Error (ppb)	PAC Days (Prod.)	Eff. %	Calendar Weeks (Prod.)	Comm. Weeks	Total Weeks
I	100	11.0	2.88	14	40	5	6	11
II	95	4.04	1.05	95	50	27	3	30
III	90	2.43	0.63	235	60	56	4	60
		2.05	0.53	**344**			**13**	101

Table 9: *Summary of the Estimated Beam Time (75 μA, $P_e = 80\%$).*

not only important technical milestones are met, but also that each run will provide publishable results and will significantly add to our knowledge of electroweak physics to date.

One important criterion for gauging the amount of running time required is to estimate how close one can approach counting statistics in the instantaneous raw asymmetry measurement (see the discussion in Sec. 3.5.1). From our Monte Carlo simulation, we estimate that $\sigma(A_i)$ for a 0.96 kHz pulse-pair is 83 ppm. Considering the various sources of additional fluctuations such as target density and electronics noise, an aggressive but realistic goal for final production running is $\sigma(A_i) = 90$ ppm. However, it will be challenging to achieve the final goal for $\sigma(A_i)$ in early running, so we will assume 100, 95 and 90 ppm respectively for the three running periods.

Another important criterion is overall efficiency. Generally, once parity experiments have been properly commissioned, the up-time should be 90% for the experimental apparatus, since stable run conditions are required over extended periods of time. Coupled with an accelerator efficiency of 70%, the final running should yield an effective efficiency greater than 60%. Again however, we are unlikely to achieve this in early on. So, we have assumed total efficiencies of 40, 50 and 60% respectively for the three running periods.

We summarize our estimated beam time in Table 9. The total request is for 344 PAC days for production running and 13 commissioning weeks over the three running periods. In the following, we summarize the goals of each run and then discuss special considerations that must be part of the discussion with both the scheduling committee and accelerator operations before final beam time allocation.

5.1 The Three Runs

5.1.1 Run I

The primary goal of the first run will be to commission the principal subsystems of the apparatus. The focus will be on validating the target design, the spectrometer optics, rejection of background and the demonstration that detector fluctuations are dominated by statistics. Once this is established, a reasonable goal would be to achieve a statistical error better than or equal to the E158 result, which we conservatively estimate can be done in 5 calendar weeks. The duration of production running also allows enough sensitivity to demonstrate that there are no anomalously large background asymmetries from charged current processes.

5.1.2 Run II

The primary goal of the second run is to get more than 25% of the proposed statistics so that one is able to achieve $\delta(\sin^2\theta_W) \sim 0.0005$. This would be the single-best such measurement at $Q^2 \ll M_Z^2$, which could already potentially have a major impact on TeV-scale physics depending on the status of LHC data anomalies. The control of beam helicity correlations must be fully commissioned to achieve $\delta(A_{raw}) \sim 1$ ppb. The fractional statistical error of 4% will require modest but not the ultimate systematic control of absolute normalization errors such as the beam polarization. We have assigned 3 weeks for recommissioning of the apparatus. We will also strive to achieve better than 50% overall efficiency for data collection.

5.1.3 Run III

This run must have all aspects of the apparatus to be working to its full scope. We must also have enough diagnostics in place and sufficient trained personnel within the collaboration so that high quality data can be collected with the best possible efficiency. We are targeting 60% total efficiency. The full control of normalization errors such as the absolute value of Q^2 and the beam polarization at the level of 0.4-0.5% must be achievable. The long duration of this run likely means that it must be split between two fiscal running cycles, and we have assigned 2 weeks of commissioning for each period.

5.2 Special Beam Considerations

Systematic control is one of the most important considerations that must govern various decisions on the design as well as running conditions for the experiment. Two important aspects of this are the methods of "slow helicity reversals" (passive sign flips of the raw asymmetry), and controlled changes to the degree of transverse beam polarization.

5.2.1 Transverse Polarization Running

The large vector analyzing power A_T for Møller scattering (ranging from 5 to 15 ppm at our kinematics) presents a unique opportunity to test the complete apparatus and its capability for absolute normalization at the fraction of a percent level, including detector acceptance, background corrections, azimuthal imperfections, radiative corrections, absolute value of Q^2 and the longitudinal beam polarization. This is because A_T is known theoretically at the 0.1% level. The Møller apparatus is capable of measuring A_T with a fractional statistical error of $\sim 0.2\%$ in a matter of 8 hours at full luminosity. We are therefore planning to request several periods, each lasting 2 to 3 shifts, of 100% transverse polarization in Hall A for a sensitive test of systematics. The periods can likely be synchronized with a change of beam energy that we also plan to request (see Sec. 5.2.4 below).

5.2.2 Wien Angle "Tweaks"

The large A_T value also represents a challenge in terms of systematic control. As discussed in Sec 4.3, in order to ensure a negligible systematic error at the fraction of a ppb level due to a coupling between residual transverse components of the electron beam polarization with azimuthal imperfections in the apparatus, it will be required to make periodic corrections to the polarization launch angle at the polarized source. We estimate that changes at the level of 1° to the launch angle might be requested once a day during production running. Assuming the launch angle was set correctly given the sensitivity of the available diagnostics, over many days the total change to the launch angle should average out to zero to high precision. We expect that these changes will be small enough to have no impact on the average longitudinal polarization that will be seen in any of the Halls that happen to be running at the same time.

5.2.3 The Double-Wien

The "Double-Wien" filter at the front end of CEBAF was commissioned during the PREX run. The system accomplishes a full flip of the beam polarization direction with a aid of two Wien filters and a solenoid lens. The method is very effective because the flip is achieved with a relatively minor change to the beam optics at the front end of the machine. This is a very powerful and crucial way to cancel subtle systematic errors.

It would be good to get 50 to 100 flips by this method over the duration of the full set of runs. This might require a configuration change once every 5 to 7 days during production running.

5.2.4 Beam Energy

Over the next two years, as the detailed design of the MOLLER apparatus evolves and depending on discussions with the Accelerator Division, the exact beam energy for MOLLER (somewhere in the range of 10.5 to 11 GeV) will be chosen and used to fix the geometry of the spectrometer and the associate collimation. Once this energy is chosen, we will immediately investigate what minimum configuration change would accomplish a beam polarization sign flip either by slightly reducing the total energy of the machine or moving from symmetric to slightly asymmetric energies in each of the two linacs.

For a symmetric linac configuration change, the beam energy change needed is $\sim$ 93 MeV. This is a small enough fractional change in the total beam energy that the MOLLER apparatus can be designed to accommodate both energies for production running with no other changes. Of course, if an asymmetric linac configuration can be found that will maintain the total energy to be the same while accomplishing a polarization sign flip, that would be desirable. However, we do not believe this is a necessary constraint, especially if it complicates other aspects of beam quality.

Over the duration of all the production running, a total of 10 energy flips would be desirable, with at least one such flip during run I, 3 to 4 flips in run II and 6 to 8 flips in run III, or effectively a configuration change every 6 to 10 weeks during production running. The exact frequency and the nature of the configuration change would be chosen after detailed consultation with the Accelerator and Physics Divisions. Since the requested frequency for the configuration change is similar to that required for transverse running, it might well be optimal to schedule the required 100% transverse running in the period in which an energy configuration change is being made.

6 Collaboration

Our collaboration has extensive experience in the measurement of small, parity-violating asymmetries with proton and electron beams. In particular, we have brought together participants in the ongoing 3rd generation Jefferson Laboratory parity-violation program (Qweak [33] and PREx [32]), plus senior members of the completed E158 [1] program at SLAC. The experimental collaboration is still growing, and we hope to expand international involvement. Theoretical support is provided by J. Erler and M. Ramsey-Musolf.

6.1 Subsystems

In the following paragraph, we list key subsystems and institutions who are interested in design, construction and implementation of them. Note that these are not firm or binding responsibilities, but simply the current thinking of the collaboration given each institution's current interests and previous experience. We have listed all the Canadian institutions (University of Northern British Columbia, University of Manitoba, University of Winnipeg and TRIUMF) as a group in this list and the detailed distribution of responsibilities among them will be determined later.

- Polarized source: UVa, JLab, Miss.St.
- Hydrogen Target: JLab, VaTech, Miss.St.
- Spectrometer: Canada, ANL, MIT, UMass, UVa
- Focal Plane Detectors: Syracuse, Canada, JLab, UNC A&T, VaTech

- Luminosity Monitors: VaTech, Ohio
- Pion Detectors: UMass, LATech, UNC A&T
- Tracking Detectors: William & Mary, Canada, UMass, UVa, INFN Roma
- Electronics: Canada, JLab
- Beamline Instrumentation: UMass, JLab, VaTech
- Polarimetry: UVa, Syracuse, JLab, CMU, ANL, Miss.St., Clermont-Ferrand, Mainz, William & Mary
- Data Acquisition: Ohio, Rutgers
- Simulations: LATech, UMass/Smith, Berkeley, Idaho State, UVa

6.2 Governance

The MOLLER collaboration is at present being organized and run by a Steering Committee consisting of senior PIs with extensive experience in similar parity-violation experiments. It is chaired by K. Kumar. We have also formed working groups to organize the development of various subsystems, with coordinators to oversees various developments. The groups and conveners are:

- Polarized Source: G. Cates
- Polarized Beam and Beam Instrumentation: M. Pitt
- Hydrogen Target: J-P. Chen
- Spectrometer: K. Kumar
- Integrating Detectors: M. Gericke
- Tracking Detector: D. Armstrong
- Polarimetry: K. Paschke
- Electronics/DAQ: R. Michaels
- Simulations: J. Mammei, D. McNulty

If MOLLER moves forward as a project funded by DoE and NSF, we anticipate putting a more formalized collaboration structure similar to other projects of comparable size. We are also seeking help and advice on how to organize MOLLER as a formal project. We discuss our near-term R&D plan and the current status of our estimates of project cost next.

7 Research and Development Topics

It is hoped that the MOLLER project can obtain significant project funding for design, construction and assembly starting in FY14, and that proper planning would allow assembly of the apparatus to commence towards the end of FY16. In anticipation of this schedule, the collaboration has developed R&D activities to be carried out in preparation in 2012-13, which we discuss in this section. While some of the topics are being carried out in collaborating institutions with graduate student and postdoc efforts from ongoing user grant funds, a significant portion of the activities will require technical manpower from national laboratories, and are therefore candidates for pre-R&D funding in FY12 and FY13. Based on further discussions within the collaboration and with JLab management, a specific prioritized funding request will be developed.

7.1 Polarized Beam

7.1.1 Polarized Laser Light

In collaboration with the Polarized Electron Gun Group at JLab, research has started on methods for achieving the fast helicity flip goal of stable polarization in 10μs. A prototype Kerr cell is being developed. A liquid Kerr material may not experience mechanical shock from a fast high voltage transition and is expected to allow for very fast transition times. As an alternative, studies are continuing on shaping the high voltage transition to speed transition and reduce piezo-optical ringing in a Pockels cell. More generally, the ongoing program of study to optimize alignment and characterization techniques for polarized source optics is continuing.

7.1.2 Beamline Instrumentation

As noted in Sec. 4.1, the experiment requires that the beam charge be measured with a precision of 10 ppm for 1 kHz window pairs. Achieving this goal will require significant R&D. This will initially be done in cooperation with the Qweak experiment (which includes many MOLLER collaborators). As part of its systematic studies, the Qweak collaboration needs to study the behavior of its BCM (beam charge monitor) device measurement resolution. These results will help the MOLLER experiment plan further R&D efforts on this topic. The charge monitoring system used by Qweak consists of two stainless steel microwave cavity charge monitors with a primarily analog electronic read-out system. This system provided adequate resolution (60 ppm for 240 Hz window "quartets") for the experiment in its initial production run in 2010.

For redundancy in this critical measurement, an alternate system was also used during the run. It consists of two cavity monitors of the same design with a digital electronic read-out system designed by the JLAB rf electronics group. This system showed great promise, but it was limited by common mode noise. An improved version of this electronics with better isolation is being implemented for the second production run of Qweak in Nov. 2011 - May 2012. Also, two additional cavity charge monitors (equipped with the digital electronics readout system) are being added to the Qweak beamline for this run. Routine production running of the Qweak experiment will provide data on the stability of the BCM resolution and the valuable comparison of the charge normalization with the two different systems.

Systematic studies will also be performed to measure the charge monitor resolution as a function of beam current and window pair rate for both systems. These studies will help determine most important contributing factors to the charge monitor resolution, which will allow the MOLLER experiment to plan the optimal R&D upgrade path to meet our resolution goal. This R&D could be performed during the 12 GeV shutdown with a goal of testing improved apparatus in the Hall A beamline early after the 12 GeV turn-on.

7.1.3 Beam Transport

Compared to 6 GeV, at 11 GeV the CEBAF beam will have a much larger emittance due to synchrotron radiation in the recirculation arcs. The effect of this emittance growth will be complicated by skew focusing fields in the RF accelerating cavities and in other optical elements. Accelerator Division has initiated simulation studies of beam properties to predict the increase in beam halo associated with this effect and known non-linearities in machine optics. These studies will also be used to refine procedures for maximizing the benefits of adiabatic damping of helicity-correlated beam asymmetries. The collaboration will encourage and assist this program of studies, including supplementing these studies with beam-based measurements before and after the energy upgrade.

7.2 Target Design

Work must begin soon on the issue of achieving a reliable conceptual design for the liquid hydrogen target system. The first activities will be more sophisticated simulations with the CFD program by physicists, a review of the appropriateness of the E158 target cell and the loop pump by designers and engineers associated with the JLab target group, and a collaborative effort for calculations related to cryogenic supply and return. A software license will have to be purchased for the CFD calculations. Depending on funding availability, it might be possible to design and test a prototype target using liquid nitrogen. An Early Career pre-proposal that would incorporate this effort into a multi-purpose CFD facility at JLab has been recently submitted to DoE.

7.3 Simulations and Software

The collaboration has chosen to use GEANT4 to develop an application for designing the acceptance and studying the backgrounds for the experiment. Field maps are produced using the "coils only" capability of TOSCA (which was used to design the actual conductor layout for the coils of the magnets) and then read into the GEANT4 simulation. Two applications are under consideration; the continued development of the one used to produce results shown in the original proposal to the JLAB PAC, as well as the possibility of adopting the GEMC application which was originally developed for use in Hall B.

The geometry used in the simulation will continue to grow in complexity. The next step is the design of a "2-bounce" collimation system for photon background. Additional physics generators are needed for backgrounds from pion production, electrons which scatter from the aluminum in the target cell, and weak decays with large analyzing power, to test the conceptual design of auxiliary detectors, and to gauge the radiation levels in the Hall from neutron production. The simulation will also be used to determine the expected energy deposited in the collimators and the coils of the spectrometer, and to optimize the dimensions of the radial and azimuthal segmentations of the primary quartz detectors, and design the air light-guides.

The analysis software and software tools needed for MOLLER will be related to those used by previous parity violation measurements at JLab, such as Qweak and PREX. The higher event rate and larger number of detector channels lead to a data rate that would be a challenge for the software to provide rapid diagnostic and analysis results. The development of the analysis software and online tools can progress in parallel with the continuing development of simulation, allowing exploration of different software choices before the electronics and data acquisition designs are fully developed.

7.4 Spectrometer Design

In summer 2010, a Magnet Advisory Group was formed to provide advice to the MOLLER project regarding the design of the spectrometer magnets. The group consists of engineers who have extensive experience with high power warm magnet designs. The group members are: George Clark (TRIUMF), Ernie Ihloff (MIT-Bates), Vladimir Kashikhin (Fermilab), Jim Kelsey (MIT-Bates), Dieter Walz (SLAC) and Robin Wines (JLab). Their feedback was used to prioritize recent R&D activities. They will be consulted again in the next few months once pre-R&D funding for further design effort becomes available.

Over the past year, the conceptual design for the spectrometer has been improved to take into account the actual layout of the conductor within the available space between the beamline and the acceptance electron envelope. Although the current optics with the actual conductor layout are acceptable, efforts are ongoing to improve the focus of the Møller electrons at the detector plane to reduce the size of the peak in order to minimize the contribution from backgrounds. The collimation system also has to be adjusted to work optimally with the new fields, and to reduce the amount of photon backgrounds seen from the edges of the collimators. Conceptual designs of the support structure of the magnets and collimators need to be developed, as well as the water-cooling systems for both the toroids and the collimators and the electrical connections for the toroids.

7.4.1 Toroid Design

The optics of the spectrometer with the actual conductor layouts changed slightly from that of the idealized fields used in the proposal, and further optimization needs to be done in order to minimize both the neutral backgrounds and those from electron-proton scattering, and to improve the radial focus of the Møller peak as well as the radial separation of the Møller and e-p peaks. Studies of the manufacturing tolerances for coil mis-alignments or rotations, as well as for the straightness of the conductor along the length of the coils need to be performed. Preliminary studies of the magnetic forces on the coils need to be expanded to study the effect of coil mis-alignments as well.

Conceptual designs of the support structure and electrical and water-cooling connections need to be carefully considered so as not to interfere with the scattered electron envelope, or to cause stray fields which could affect the focus. The support structure must support the weight of the collimators, coils, water and water and electrical connections, and be able to withstand the magnetic forces on the coils as well as the mechanical stresses of the water flowing through the conductor. TOSCA will be used to check for interferences with the conceptual designs of the coil supports and the various connections.

7.4.2 Collimation and Shielding

The collimation system is needed to define the acceptance of the Møller electrons, block line-of-sight to the target and shield the coils. A preliminary design is in the simulation which produces a reasonable acceptance, but needs to be optimized to reduce the size of the Møller peak. This design also seems to block line-of-sight to the target even with the new field maps, but higher statistics simulations are needed to confirm this. The collimators will be neutron sources in the hall, and the shielding for the electronics needs to take this into account. Simulations will also be used to estimate the power deposited in the collimators, some of which will need to be water-cooled.

The next steps will be to develop mechanical designs for the collimators and associated water cooling. The support structure of the toroids will have to support the collimators and allow for the water-cooling connections for them as well. Additionally, once the mechanical structure is defined, appropriate sections of the beamline must be housed in custom concrete structures to limit radiation; these structures must be designed to be easily removable and must be optimized for quick assembly so that multiple runs and interleaving with other projects can be done efficiently.

7.5 Detector Design

Figures 17 and 18 in Sec. 3 show the layout of the main detector elements. There is significant R&D that needs to be carried out to flesh out the conceptual design and reaffirm the technology choices that were made based on experience from previous PVES projects.

7.5.1 Quartz and Light Guide

Thin quartz detectors were the technology of choice for the PREX and Qweak experiments. The shape, dimensions and surface quality of the quartz all play critical roles in determining how many photo-electrons will reach the detector. An equally important issue is the shape and material of the air light guide. After these issues are optimized in a Monte Carlo simulation, it will be very important to build a few prototypes and benchmark the performance using cosmic ray studies as well as test beam studies. In addition, such a test will validate the specific choice of light detector, which is a complicated decision based on efficiency, uniformity, linearity, radiation hadness and background rejection.

7.5.2 Mechanical Assembly

We have developed a proof-of-principle concept using a CAD program for a compact assembly of the full complement of quartz detectors and light guides. Once the light guides have been optimized with Monte Carlo simulations and benchmarked with cosmic and beam tests, the next step would be to have an engineering design of the detector assembly, which is complicated not only by the compact and dense detector array, but also the necessity to have a significant lead housing for the light detectors. This significantly increases the weight of the detector assembly. In addition, the entire assembly must be easily transportable to reduce the turnaround time between interleaved projects.

7.5.3 Pion Background

As discussed in Secs. 3.4.2 and 4.5.3, we plan to design auxiliary detectors that will measure the relative flux of pions as well as the resultant parity-violating asymmetry directly during data collection. We have a preliminary conceptual design for these measurements. The next steps are to develop a full Monte Carlo generator for pion production including those from weak hyperon decays, and also to develop simulations of pion background in order to optimize the detector conceptual design.

7.5.4 Tracking Detectors

As described in Sec. 3.4.3, a tracking system has several critical applications to understand the apparatus and control systematic errors. The GEM technology that is being proposed is part of a significant R&D effort that is important for several other projects after the 12 GeV upgrade at JLab. MOLLER collaborators play a significant role in these initiatives. In addition, a conceptual design for the external GEM detector holders has to be developed. Finally, it is envisioned that the first plane of GEMs would be insertable into the scattered beam envelope using the concept of “Roman pots”. This concept needs to be explored in the specific context of the MOLLER spectrometer and beamline and may warrant mechanical tests with prototypes before a final decision on the technology choice can be made.

7.6 Polarimetry

7.6.1 Compton Polarimetry

A vigorous and dedicated R&D effort is planned for a group consisting of physicists from a number of collaborating institutions with prior experience with Compton polarimetry and laser development. One of the largest challenges to operating the JLab Compton polarimeters has been bremsstrahlung photons scattering from narrow beam apertures, which are required by the small electron-laser crossing angle. At 12 GeV, beam emittance growth driven by synchrotron radiation in the arcs of the higher passes might exacerbate this problem, and force a re-engineering of the Compton interaction region.

In order to maintain high luminosity at a larger electron-photon crossing angle (and therefore larger beam apertures), we propose moving from green to infrared light and upgrading the power build-up cavity gain and injection power. While the power upgrade should be relatively straightforward, the other essential requirement is that the laser system must allow a 0.2% laser polarization measurement. This is a significant improvement on recent performance. R&D on the precision polarization measurements on stored laser light must start soon, to demonstrate the feasibility of using a high-gain system to achieve high precision.

An alternative concept for a new laser system has also been proposed based on a short-pulse mode-locked laser, either colliding with the beam directly or injected into a low-gain Fabry-Perot cavity. Such a system would significantly simplify the determination of laser polarization while maintaining sufficient statistical power and reducing systematic errors associated with backgrounds. Development of such a laser system could start in parallel with the default design; this alternative would be adopted if studies of the CW system fail to demonstrate sufficient precision in polarization measurements.

A separate challenge in 11 GeV operation would be the total power of synchrotron light incident on the photon detector from bends in the Compton chicane. Initial studies have shown that minor changes to the chicane magnets can reduce the synchrotron power at 11 GeV to the level observed in 6 GeV operation. The initial studies will be followed up with improved simulation, and detailed magnetic modelling and mechanical design of the shims to incorporate them into the beamline.

7.6.2 Møller Polarimetry

As described in Sec. 4.2.2 and in more detail in App. G, a Møller polarimeter using a pure iron foil target in a 4 T field is a backup plan that should yield a complementary measurement of the electron beam polarization with a systematic error of 0.8%. The PREXI measurement of beam polarization at 1 GeV achieved 1.1%. It is anticipated that PREXII (if approved) will provide the opportunity to develop the stated goal of 0.8%.

A new R&D thrust will be to develop the concept of atomic hydrogen polarimetry for the JLab high intensity electron beam. A collaborative effort is in the process of being formed between the institutions interested in this project, led by MOLLER collaborators from the University of Mainz. The Institute for Nuclear Physics there is proposing a new project called MESA. It will produce up to $\sim$10 mA beams with an energy up to 200 MeV and will perform high-precision low-energy parity-violation experiments (e.g. Q_{W}^{p}) as well as dark matter searches. Because of the very low beam energies, the MESA apparatus cannot use a conventional Møller polarimeter or a Compton polarimeter and will need the atomic hydrogen Møller polarimeter for sub-1% measurements. The MESA proposal is under consideration by funding agencies in Germany, and we should know in early 2012 whether it is successful in obtaining funding.

It is envisioned that Mainz would become the technical lead on atomic hydrogen polarimetry, though there will be significant participation also from other US institutions who are part of the MOLLER collaboration. The Jefferson Lab target group would need to play an essential role as well. Assuming successful funding for the MESA project, a possible outline of the R&D effort is the following. First, we can learn from a prototype of the hydrogen cell that had been built several years ago by the University of Michigan and which has been obtained by and is presently stored at the University of Virginia and could be shipped to Mainz. Practical experience can be gained by reviving the functionality of this prototype. In the meantime, the simulations must be refined and a new prototype more directly suitable to the application can be designed. Target cells and the electrodes for sweeping away the ions must be designed. Bench tests will be performed, and beam tests at the Mainz Microtron will be undertaken to prove that the concepts work.

The goal of this R&D is to produce a working polarimeter based on a storage cell with 100% longitudinally electron spin-polarized hydrogen, with a thickness of at least 6×10^{16} electrons/cm^2, a systematic accuracy of $\leq 0.5\%$, that operates in the presence of the 100μA CEBAF beam. Once the benchmarks have all been established, the apparatus would need to be brought to Jefferson Lab for the MOLLER project. The expensive components are the solenoid and the dilution refrigerator (with its pumps), so it is presently thought that we would share these items between Mainz and Jefferson Lab. The other components of the system are relatively less expensive, and to a degree customized to the laboratory location, so they would be copied locally at each laboratory. We note that the ultimate sensitivity will be required only for Run III, and that this entire R&D plan is driven more by the needs of the SoLID project, which will likely run before MOLLER's final run.

8 The MOLLER Project

Table 10: *Proposed MOLLER project funding profile. Estimates include 40% contingency.*

	Estimated costs in then year $k (escalated)								
	FY11	FY12	FY13	FY14	FY15	FY16	FY17	FY18	Total
Pre-R&D		400	400						800
R&D									
CDR									
PED				4,402	884				5,286
Construction					9,169	5,738	688		15,595
Pre-ops									
TEC				4,402	10,053	5,738	688		20,881
TPC				4,402	10,053	5,738	688		20,881

CDR = Conceptual Design Report, PED = Project Engineering & Design, TEC = Total Estimated Cost = PED + Construction, TPC = Total Project Cost = TEC + R&D + Construction + Pre-operations.

We have taken a first look at all the major MOLLER subsystems to carry out a preliminary costing exercise. Experience from previous experiments, estimates from JLab engineers & designers (albeit quick ones), purchases by other experiments at JLab like Qweak, and quotes from vendors have been used to develop the estimates. While the estimates are very preliminary, attention was paid to apply proper escalation to obtain estimates in actual year dollars, assuming that project engineering and design funding begins in FY14. Table 10 shows the proposed project funding profile after adding 40% contingency. The profile assumes that technical questions requiring prototyping or development have been resolved by the time project engineering & design starts in FY14. Table 11 shows the Møller project cost highlights.

9 Conclusions

We have described an experimental design to measure parity-violation in electron-electron scattering to unprecedented precision using the 11 GeV electron beam in Hall A at JLab. The project represents a unique opportunity to probe physics beyond the Standard Model at the TeV-scale, probing contact interactions in a manner complementary to the LHC that could become crucial in the next few years depending on what is discovered at LHC and elsewhere. The specific measurement described here would be the most sensitive low energy measurement of a flavor-conserving purely leptonic interaction at low energy and cannot be carried out in any other existing or planned facility anywhere in the world. It is further worth noting that the sensitivity goal for A_{PV} in Møller scattering can only be achieved at JLab. The project would realize its full potential towards the end of the decade, which is timed well with availability of full statistics from various LHC searches.

A motivated and experienced collaboration is ready to carry out the R&D, design, construction, installation, data collection and analysis. Given the evolution of related projects, the timing of the 12 GeV upgrade, and the compelling physics opportunity, we urge that the MOLLER project be given serious consideration to be reviewed to enter the Critical Decision process as promptly as possible.

Table 11: *Cost highlights of the MOLLER project. Estimates* **do not** *include contingency. The estimates are actual year dollars based on the profile shown on Table 10. The estimates shown include JLab overhead.*

Component	Estimate ($k)
Liquid Hydrogen Target	
Engineering & Design (E&D)/Fabrication	1,487
Spectrometer	
Upstream Toroidal Magnet - E&D/Fab.	557
Downstream Toroidal Magnet - E&D/Fab.	1,579
Magnet Collimators - E&D/Fab.	755
Power Supply - 800 kW	307
Main Integrating Detector System - 252 channels	
Quartz, Light-Guides, PMT & HV base	1,207
Pre-Amp & ADC (Triumf)	307
VME Crates, CPUs, cables, connectors, HV supplies	472
Detector Support & Shielding (E&D/Fab.)	750
Testing (including hardware) & installation labor	229
Auxiliary Detector System	
GEM chambers (27 + spares, ∼30cmX30cm each) with electronics	670
"Roman Pot" mechanics for GEMs (7) - E&D/Fab	250
Synchronized Rotator with GEM flipping mechanism - E&D/Fab.	180
Pion Detectors (6) (GEMs accounted above)	137
Luminosity Monitors (8) & Shielding/Mech. Support	137
Testing (including hardware), installation labor & integration	282
Hall A Infrastructure	
Beam-line modifications (before target)	741
Add 2 MVA transformer	449
Isolated LCW for magnet cooling - E&D/Fab.	331
300 concrete blocks (stainless-steel rebar)	1,066
Hall cryogenic transfer-line upgrade	1,317
Hall Installation (including labor)	1,046
Miscellaneous	
Computing and Data Acquisition (including CPUs)	390
Project Management	269

A Polarized Beam

A.1 Polarized Electron Source

Laser light illuminates a semiconducting photocathode, the surface of which has been chemically treated to produce a negative work function, referred to as a negative electron affinity (NEA) surface. The laser light wavelength is tuned to promote electrons from a specific valence band to the conduction band of the semi-conductor. The photocathode is held at a negative potential, so as the electrons from the conduction band exit the cathode they are accelerated into the injector beamline.

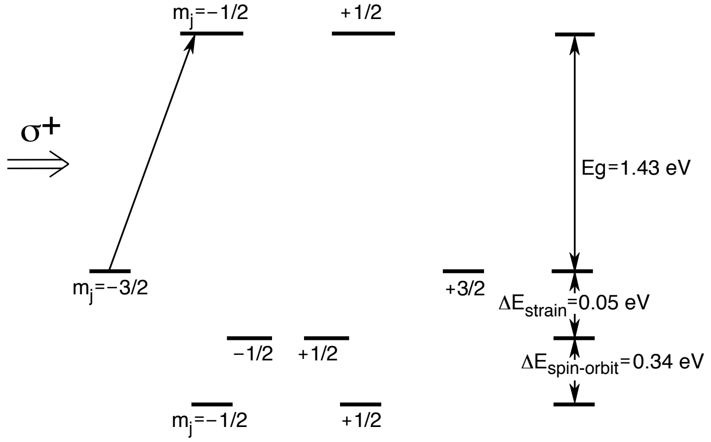

Figure 20: *Band structure of GaAs, showing how circularly polarized laser light produces polarized electrons.*

Through doping or other stress applied to the photocathode, the degeneracy in the spin-orbit states of the specific valence band are split, as shown in Fig. 20. For circularly polarized light, the spin-1 photon is restricted to exclusively promote electrons to a single spin state. This process produces an electron beam polarization of nearly 100%, however, some depolarization occurs in the diffusion of the liberated electrons to the photoconductor surface. The CEBAF polarized source now routinely provides $\sim 85\%$ polarization with up to a few hundred μA beam current.

Since the electron polarization is fully determined by the circular polarization of the incident laser light, it is possible to rapidly flip the helicity of the electron beam by changing the laser polarization. This is accomplished using an electro-optic Pockels cell, acting as a quarter-wave plate to produce circularly polarized light from the initial linear polarization. A reversal of the applied voltage on the Pockels cell reverses the circular polarization of the laser light, and thus the helicity of the electron beam. A schematic diagram of the experimental configuration is shown in Fig. 21.

A.2 Operational Experience

There is significant operational experience in using the polarized electron source for parity-violation experiments at Jefferson Lab [37]. One challenge of these experiments is that changes in the beam properties (intensity, position, profile) will change the detected scattered flux. If the changes in the beam are correlated with the electron helicity, the result can mimic the tiny parity-violating asymmetries. While changes are typically measured and corrections are applied, the corrections are typically made with precision of around 10%. Helicity-correlated beam asymmetries (HCBAs) are therefore a potential systematic error in the mea-

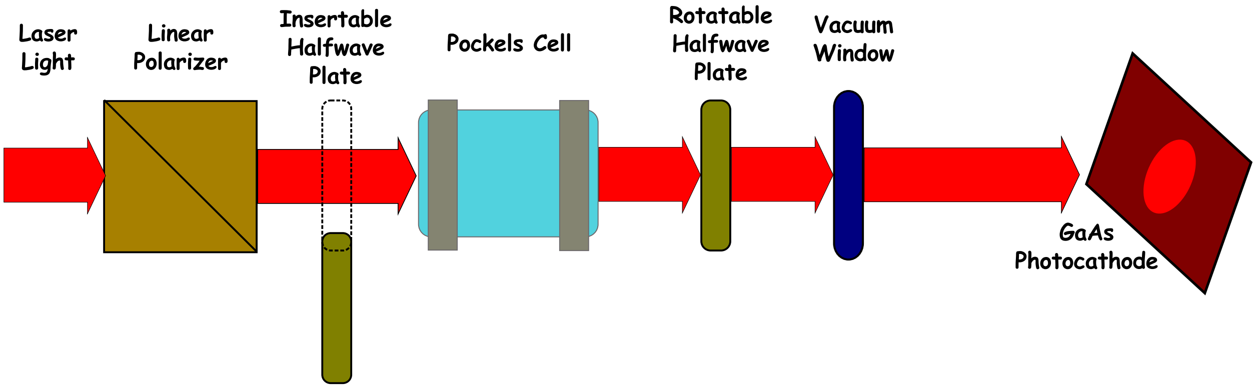

Figure 21: *Schematic of the laser transport line that allows for rapid reversal of the electron beam polarization.*

surement of small asymmetries, and a very high level of control of HCBAs is required for the precision measurement contemplated here.

A sophisticated understanding of the sources of HCBAs at JLab has been achieved. The HAPPEX-II experiment, which ran in Hall A in 2005, made use of this improved understanding to achieve run-averaged helicity-correlated position differences, measured in the experimental hall, which were consistent with zero systematic offset with uncertainties of < 2 nm and 0.2 nanoradian in angle (see Fig. 22).

The PREX experiment, which ran in Hall A in early 2010, and the Qweak experiment, which started data-taking in Hall C in mid-2010, have statistical-precision goals that are approximately an order of magnitude better than what has been achieved previously at JLab. Regarding systematic effects, the PREX experiment ultimately aims to keep helicity correlated beam motion to < 1 nm (HAPPEX-II achieved < 2 nm) and to bound the beam spot difference to $< 10^{-4}$ of the intrinsic beam size. In the 2010 run, with only eight days of production beam, correlated beam motion was held to < 4 nm with no feedback, a notable achievement in such a short running time when other problems, mostly vacuum related, dominated our efforts. We note finally that the polarized-source setup, fine-tuned to reduce systematics, was probably the best ever achieved. When we are better able to take full advantage of all we have learned about source-related systematics, we are confident that the goal of holding helicity-correlated beam motion to < 0.5 nm for MOLLER is achievable. Between further PREx running (PREx-II was just approved by PAC-38), and ongoing Qweak running, we will be gaining valuable experience toward meeting the stated MOLLER goals for controlling HCBAs.

A.3 Adiabatic Damping

The impact of helicity-correlated spatial variation in the beam can be greatly reduced in the accelerated beam impinging on the target due to the process of adiabatic damping. A simple consequence of relativistic mechanics is that the available phase space for a beam which has been adiabatically accelerated to a momentum p from a momentum p_0 is reduced by a factor of $\sqrt{p/p_0}$. For the 3 GeV beam energy of the HAPPEX-II experiment, this corresponds to a reduction in beam motion in each dimension by a factor of ~ 95, compared to motion of the 100 keV injector beam.

The benefits of this effect are typically not fully realized; getting close to the theoretical limit requires detailed understanding of accelerator beam optics, tuning and diagnostics. The collaboration typically works closely with accelerator physicists to produce the best results and maintain them over the duration of data

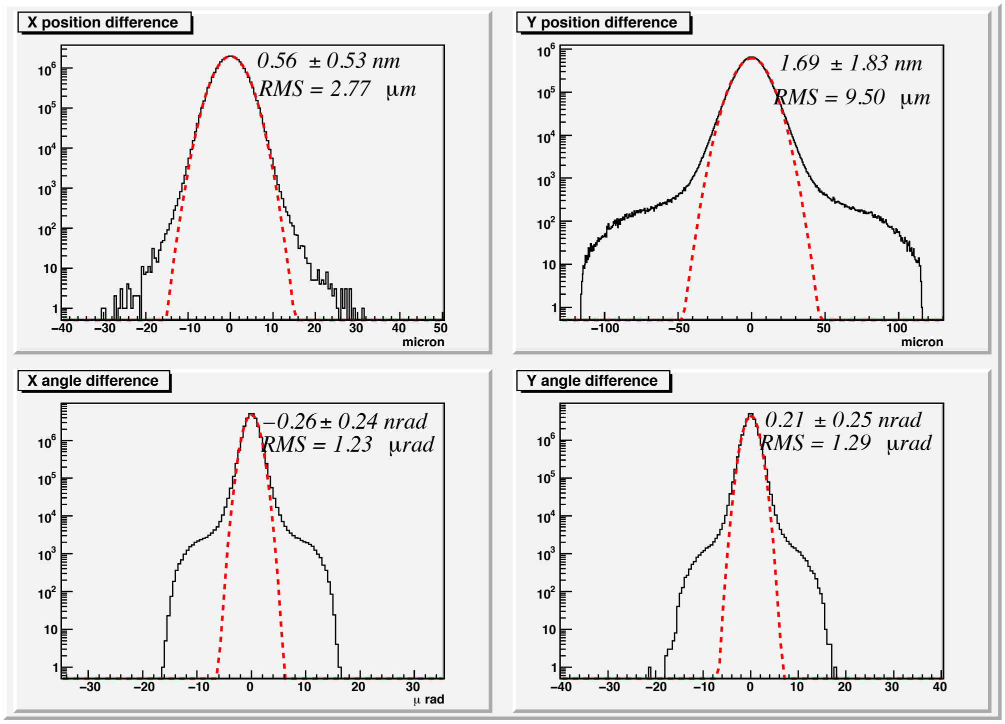

Figure 22: *Beam position and differences, plotted for all* 27×10^6 *pairs of the HAPPEX-II analysis. Arithmetic means, widths, and centroid uncertainty due to random noise are shown. The systematic correlation to helicity was measured to be consistent with zero within the random beam noise. Gaussian fits are included for reference.*

collection. The best performance from the HAPPEX-II experiment suggested that helicity-correlated variations were suppressed by factors up to ~ 30.

The benefits from adiabatic damping have lagged behind the theoretical maximum in part due to difficulties in configuring the 100 keV injector region. Additional diagnostics and optics in that portion of the injector would presumably allow greater benefits to be realized. Such work, in addition to other, already implemented, additions to diagnostics and control, should make it possible to realize a significant fraction of the theoretically maximum suppression factor of 180 for the case of a 11 GeV beam.

Apart from the obvious benefits for helicity-correlated beam fluctuations from adiabatic damping, there are also advantages for random fluctuations in the beam trajectory on target. In order to ensure that one attains the goals for systematic corrections, random fluctuations in beam parameters at 1 kHz must be less than those specified in Table 5. Recent tests during the commissioning of Qweak have demonstrated that these goals should be straightforward to achieve.

A.4 Slow reversals

The technique of “slow helicity reversal” generally refers to the introduction of an additional helicity flip, which changes the sign of the helicity relative to some sources of HCBA. An example would be the introduction of an additional half-cycle $g-2$ rotation, which would reverse the electron beam helicity with respect to the helicity of the beam created in the polarized source. The statistical consistency of data sets taken in different states of the reversal can be used to demonstrate the absence of large, unknown systematic errors, and the combination of data sets (appropriately sign-corrected) provides a method for further canceling possible unmeasured or poorly-corrected HCBA effects.

Until quite recently, only one slow-reversal has been commonly employed at CEBAF. A half-wave plate is inserted into the laser path to reverse the sign of laser polarization, relative to the voltage applied to the Pockels cell (see Fig. 21). This slow-reversal is particulary effective for cancelling two types of effects. First, any false asymmetries related to electronic signals, either from the logic or Pockels cell high voltage, will be completely unaffected by the insertion of a half-wave plate. Thus, such false asymmetries will not change sign while the physics asymmetry does change sign. Second, it is well established that when a Pockels cell is pulsed, it can steer or even focus the beam in a fully helicity-correlated fashion that is unrelated to polarization effects. Presumably this is due to the piezoelectric properties of the crystal or simple mechanical stress. Such steering and focussing will be unaffected by the half-wave plate, again insuring the false asymmetries will not change sign when the physics asymmetry does. Many HCBA's, however, are explicitly related to helicity-dependent residual linear polarization. Most of these effects will change sign with the insertion of the half-wave plate just at the physics asymmetry does, and hence are not cancelled. For this reason, other methods of slow-helicity reversal are desirable.

At 11 GeV, the total number of $g-2$ spin rotations will be large, on the order of 120π. It will be possible to change the orientation of spin, while maintaining very similar beam optics properties, by changing the energy of the accelerator by about 100 MeV. This interval is small enough to not require invasive reconfiguration of the experiment: backgrounds, spectrometer optics, etc. should remain very similar. This would be a very effective slow reversal, in that all HCBAs from the source should influence the final measurement with the opposite sign. Since this is disruptive to other halls, this method might be used a few times over the duration of the entire run.

A similarly effective slow reversal that can be used much more often can be created using spin manipulation in the injector. Spin manipulation (using a "Wien rotator") is necessary in the CEBAF source to align the electron polarization into the horizontal plane, and then to set the in-plane launch angle to optimize longitudinal polarization at the experimental target. In principle, it is possible to apply a half-cycle spin rotation without changing the optics of the beam. In practice, this requires a more complicated spin manipulation in the CEBAF injector. The "Double-Wien" filter (shown schematically in Fig. 23) uses a second Wien rotator and a solenoid, which allows a helicity slow reversal using only solenoidal spin manipulation without changes to the Wien rotator setpoints. This system was commissioned prior to the PREX run in 2010, and it was used routinely during both the PREX run and the ongoing Qweak run to achieve a slow spin flip with relatively minor changes to the front end beam optics.

A.5 Requirements for 11 GeV

A.5.1 Rapid Helicity Flip

Previous parity-violation experiments at Jefferson Lab have used a rapid helicity reversal frequency of 30 Hz, which had the benefit of largely cancelling beam jitter and electronics noise related to 60 Hz line noise. It will be necessary for future experiments to flip the helicity much more quickly, in large part because it is expected that density flucuations in the high-power cryotarget are limited to frequencies below a few hundred Hz. This proposal is designing around a flip rate of at least 2 kHz, which implies that each helicity state is held for 500 microseconds. In order to avoid excess noise from 60 Hz line variations, a scheme for selecting helicity states will be used which will force complementary pairs at corresponding points in the 60 Hz cycle.

The goal is to flip the Pockels cell within 10 μs, which implies a dead-time of 2%. At present, a settling time of 60 μs is achievable for reversal rates of 960 Hz. However, it has proven difficult to push the transition of the Pockels cell to be shorter than 60 μs while keeping the cell optical properties stable after

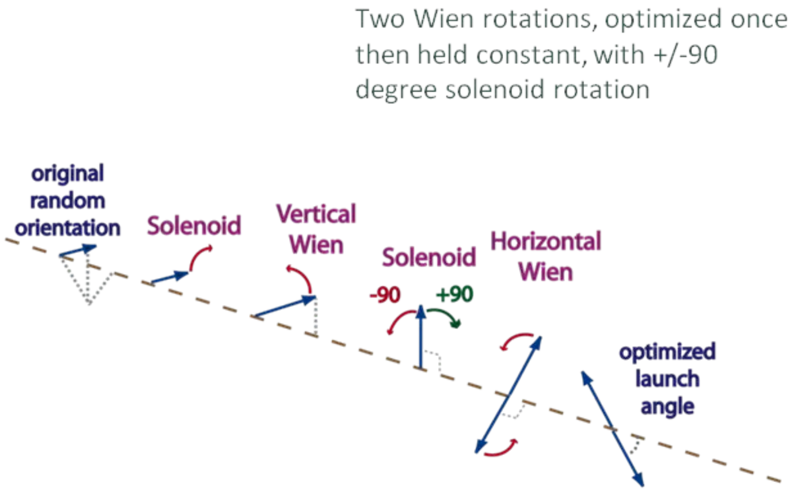

Figure 23: *Schematic of the concept of the "Double-Wien" filter, which allows a full "slow" flip of the electron beam polarization with minimal disruption to the front end electron beam optics. The flip is accomplished by adjusting the second solenoid, without changing the settings of the two Wien rotators.*

the shock of the fast transitions. Additional studies of switching with the Pockels cell will explore possible improvements from both shaping the leading edge of the voltage transition and electrical or mechanical damping of oscillations.

The ringing of the Pockels cell is thought to be related to piezoelectric shock on the voltage transition, and the resistance to completing the transition quickly may be related to other mechanical relaxation effects. A liquid-filled Kerr cell would presumablye not suffer from either effect, and is expected to be capable of very fast transitions. Kerr cells are inconvenient compared to Pockels cells, but are none-the-less a very promising route to meeting the needs for MOLLER. R&D on the use of Kerr cells for a polarized source has also been initiated. The studies will make use of characterization techniques developed for Pockels cell studies to evaluate the suitablility of Kerr cells for high-precision measurements.

A.5.2 Measurement and Control of HCBAs

Monte Carlo simulation was used to estimate the sensitivity of the apparatus to beam motion. With the minimum acceptance angle defined by collimators placed 10 meters downstream of the target center, the detected flux in one azimuthal segment is expected to change by approximately 8.5 ppb for a 1 nm shift in the beam centroid. This result is consistent with simple scaling arguments applied to sensitivities measured during HAPPEX-II. This suggests the approximate sensitivity to changes in the beam angle, as well: 85 ppb/nanoradian. The ratio of these sensitivities roughly matches the accelerator which, as a rule of thumb, has a characteristic length of about 10 meters.

A reasonable goal for any measurement of a small asymmetry is to keep the cumulative correction averaged over the entire run due to random or helicity-correlated beam motion to be no larger than the grand statistical error, and to believe the correction to 10% of itself. An important (but not sufficient) step toward achieving this goal is to further insist that beam-related corrections for an individual pulse pair are no larger than the statistical error for that pulse pair, which in our case is 78 ppm for our 1 kHz pairs. The detector for the MOLLER experiment has seven segments and a high degree of azimuthal symmetry. A goal that greatly facilitates a number of diagnostic techniques is to insist that *the beam-related corrections for each of the detector's segments are no larger than the statistical width of that individual segment, a width that will be around 200 ppm*. It is this goal (together with the caveat that we only assume that we understand our corrections at the 10% level) that guides us in most of our specifications for both beam jitter and monitor resolutions.

It is quite possible to successfully correct for HCBAs on a pulse-to-pulse basis, but still accumulate large HCBAs over the course of the entire run. This could happen, for example, if for whatever reason the corrections were always in a particular direction (with respect to the physics asymmetry). Such a problem might not become apparent until quite late in the run, since the precision of our knowledge of beam parameters during MOLLER will typically only be sufficient to keep corrections small compared to statistics. There are at least two ways out of this conundrum. One is to have significantly improved monitoring of beam parameters, something that would require improved technology beyond what we have demonstrated. The other is to employ feedback. Luckily, we have demonstrated effective feedback for both beam position and intensity at the required level. Of interest here are the sensitivities of the measured asymmetries to the HCBAs, which we will conservatively assume to be ten times better than those quoted above for individual segments.

With all the aforementioned requirements in mind, we find the following specifications for MOLLER:

- The beam centroid must be measured at two locations 10 m apart just upstream of the target with a resolution of a few microns for 1 kHz window pairs.
- The beam centroid and angle jitter must less than ~ 50 microns and ~ 5 microradians respectively at 1 kHz.
- If the beam jitter is significantly larger than quoted above, active position feedback on the electron beam at 1 kHz frequency will be necessary.
- The grand-average helicity-correlated position difference over the duration of the entire run must be less than 1.2 nm and the angle difference should be less than 0.12 nrad.

We elaborate on these issues below. The experience of HAPPEX-II, which found position (angle) differences of around 1 nm (0.2 nrad) suggests that these specifications should be achievable.

A.5.3 Beam jitter and monitor resolution

The most stringent requirement on beam position monitor resolution comes from requiring that the additional random noise contribution from beam jitter (after regression) be no larger than 10% of the counting statistics width for a single azimuthal element of the detector. This leads to a more stringent requirement than applying the same criterion to the average over all detectors. This is important for two reasons. It allows for high precision comparison among selected combinations of the azimuthal detector elements to study the behavior of the linear regression corrections. It also insures the precision necessary to measure the azimuthal dependence of the raw detector asymmetries for the "manual" feedback loop to control transverse polarization described in Sec. 4.3. Applying this criterion leads to a requirement on the beam position monitor measurement resolution of 3 μm for 1 kHz pairs. Qweak has measured the beam position monitor resolution for 480 Hz pairs for the standard "stripline" beam position monitors (BPM). Typical values of ~ 4.5 μm are found (see Fig. 24). Taking the conservative assumption that the monitor noise is dominated by white noise, the scaling from 480 Hz to 1 kHz can be estimated as $4.5\ \mu\text{m} \times \sqrt{2} \sim 6\ \mu\text{m}$ for the resolution at 1 kHz pair rate. The needed factor of two improvement to achieve the goal should be obtainable from the radiofrequency microwave cavity monitors that are installed in the Hall A beamline. These have not been

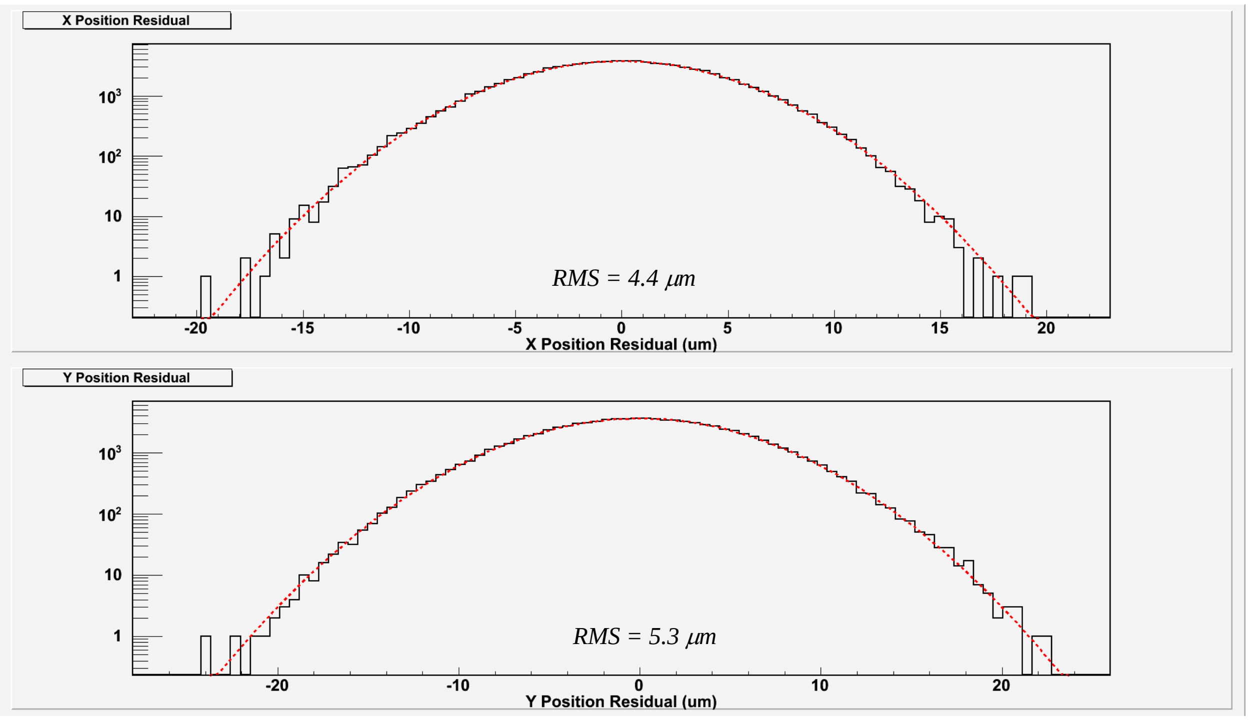

Figure 24: *Typical position measurement resolutions from the Qweak experiment for 480 Hz window pairs for "stripline" beam position monitors. The residuals from a comparison of the measured beam position to the projected position from two upstream monitors are shown.*

used extensively, but initial testing during HAPPEX running in Hall A demonstrated at least a factor of two resolution improvement over the stripline BPMs.

The goal for the accuracy of beam corrections also imposes requirements on the "jitter" (random noise) in the beam properties. Typically, the beam parameter correction sensitivities (the α_j coefficients in Eq. 9) are determined with no better than $\sim 10\%$ precision. For single azimuthal sectors, this implies that the beam property jitter can be no larger than 200 ppm for a single sector (to insure that the resulting random noise contribution after regression is no larger than 10% of the counting statistics width). This leads to these requirements on the maximum allowed jitter (see Table 5): < 47 μm (position), < 4.7 μrad (angle), and < 286 ppm (energy) for 1 kHz window pairs. Typical numbers for the jitter for 480 Hz window pairs from the running Qweak experiment are shown in Figs. 25 and 26. To project to what to expect for 1 kHz pairs, we assume a white noise assumption and multiply by $\sqrt{2}$ to obtain projected jitter values of: $\sim$ 48 μm (position), $\sim$ 1.4 μrad (angle), and $\sim$ 6.5 ppm (energy). Thus, all of the jitter requirements appear achievable, assuming the jitter behavior is similar after the 12 GeV accelerator upgrade.

As with past parity experiments, we will normalize our detector signals to beam intensity on a pulse-to-pulse basis. Here it is critical that the beam charge monitors (BCMs) and detector electronics chain are highly linear, something we expect will be true at the level of 1% or better. In our error budget (Table 4) we have allowed ourselves a 0.3% relative error associated with the BCM linearity, something that corresponds to about 11 ppm for an individual 1 kHz pulse pair when averaged over the entire detector. To be conservative, we have thus set a goal of 10 ppm for the BCM resolution associated with an individual pulse pair. Using this resolution, can can also put a limit on allowable jitter in the beam intensity. With a 10 ppm BCM resolution and 1% linearity we can tolerate beam intensity jitter of 1000 ppm (0.1%) before the jitter itself

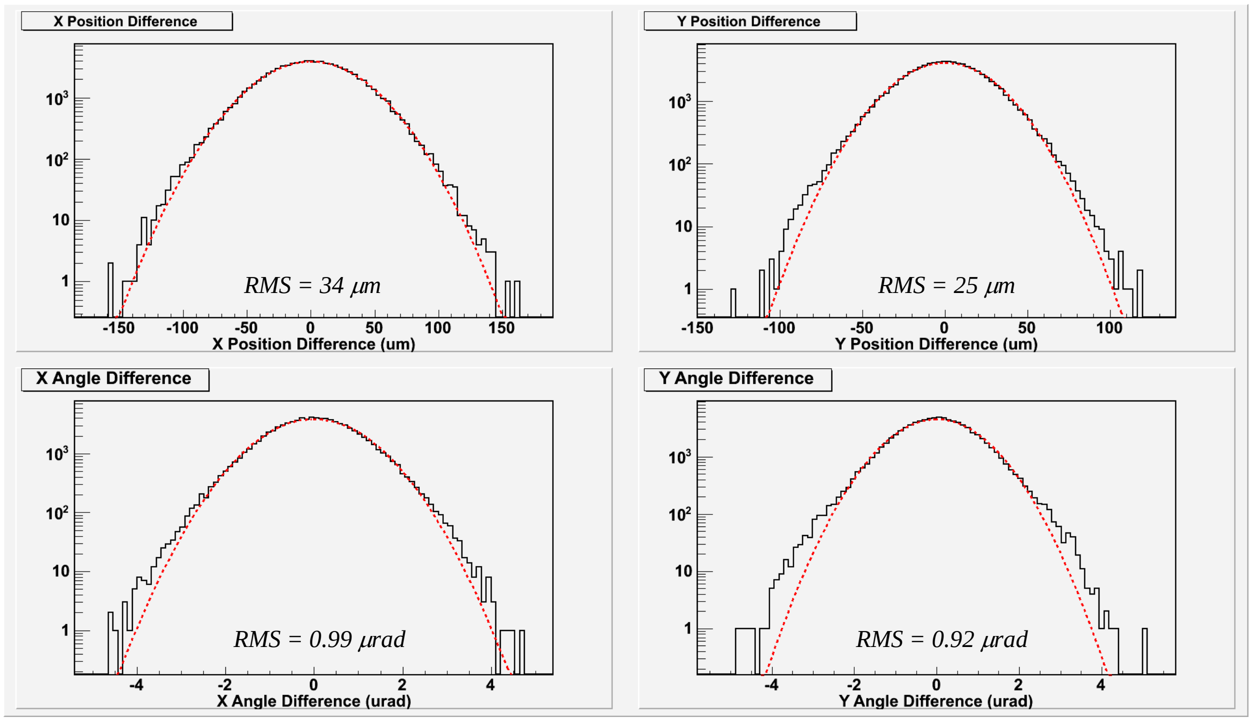

Figure 25: *Typical X and Y position and angle difference distributions for 480 Hz window pairs from the Qweak experiment at 160 μA beam current. The RMS values from the Gaussian fits are the random beam noise ("jitter") in these parameters.*

begins to add to the pulse-to-pulse statistical width. The recent Qweak data on intensity jitter at 480 Hz is shown in Figure 26. Applying the standard $\sqrt{2}$ "white-noise" scaling factor predicts $\sim$ 500 ppm for 1 kHz pairs, so the goal of 1000 ppm seems easily achievable. Finally, we note that random noise at the 10 ppm level from the BCMs, when added in quadrature to the roughly 80 ppm 1 kHz pulse-pair statistical width will result in less than a 1% increase in the statistical width.

A.5.4 Position Feedback

A more significant problem might be the slow convergence of the random beam jitter. Even with no systematic helicity-correlated offset, beam jitter of 5 micron would converge to zero with a 1σ range of 0.8 nm.

A systematic non-zero helicity-correlated position difference could be diagnosed more quickly, and the potential loss of statistical precision could be mitigated, by forcing the random jitter to converge through feedback. This feedback would necessarily be helicity-correlated, and operate with a time-scale between a few minutes and a few hours. The optimized feedback time-scale will depend on the safe dynamic range of the feedback system, the time scale of any slow-reversal or other significant beam disturbance, and the magnitude of the jitter, among other factors.

The goal of any such feedback would be to improve on the statistical rate of convergence for the beam position jitter by a relatively small amount. Under optimal feedback, the centroid would converge to zero as $1/N$, where N is the number of integration periods of the feedback cycle, compared to $1/\sqrt{N}$ for the case without feedback. A balance will need to be found between keeping the average feedback correction small, while still operating on a time scale that drives convergence to zero position difference. Updating feedback

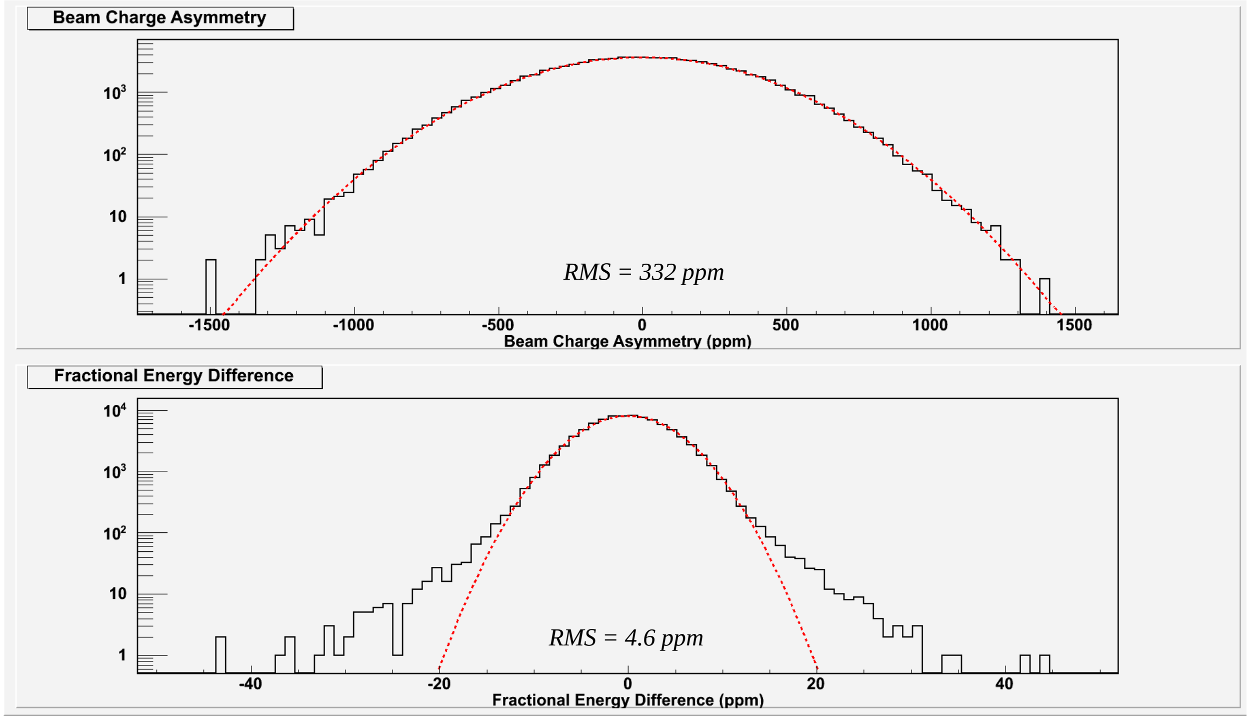

Figure 26: *Typical intensity asymmetry and energy difference distributions for 480 Hz window pairs from the Qweak experiment at 160 μA beam current. The RMS values from the Gaussian fits are the random beam noise ("jitter") in these parameters.*

every hour, for instance would improve convergence by a factor of $\sqrt{8}$ on an ideal shift, while implying that the size of the correction would be around 4×10^{-3} of the beam jitter.

It is important not to mask serious configuration problems in the polarized source with the use of intensity and position feedback systems. For this reason, the average position correction will be monitored for significant non-zero average corrections which indicate the need for re-tuning of the polarized source. It is also crucial that any position dependent feedback does not change intensity asymmetries in a way which reduces the rate of convergence of the crucial intensity feedback.

There are several mechanisms which could be used for position feedback. The commonly employed technique at Jefferson Lab, successfully employed by the G0 collaboration, uses a piezoelectric actuated mirror in the source optics to deflect the laser beam. Similar techniques were employed or tested by the E158 collaboration at SLAC and the SAMPLE collaboration at Bates.

Since the dominant source of position differences is a non-zero first moment in the helicity-dependent residual linear polarization distribution of the laser spot, a superior feedback mechanism might involve a birefringent element with a variable, linear variation of birefringence across the beamspot. Such a device could be conceptually similar to the continuously variable birefringent system, such as the Babinet-Soleil compensator.

There are several disadvantages to position feedback mechanisms which operate on the source laser. The most important is that the photocathode changes significantly on the time-scale of days. Ion back-bombardment damages the photo-cathode, creating a quantum efficiency "hole" at the laser spot and along a path to the electrical center of the cathode. Motion of the beamspot on the cathode can interact significantly with these strong QE gradients, changing the effective slope of the correction and creating significant coupling with electron beam intensity.

These complications can be avoided by using magnetic deflection of the electron beam. A system of 4 air-core magnets has been constructed in the injector, with a fully isolated power and control system. These were constructed by the Electron Gun Group as a potential feedback mechanism. As expected, this system avoids the significant coupling to beam intensity which complicates use of the piezoelectric mirror. Further testing would be required to qualify this system at the required level of precision, and at the 2 kHz reversal frequency.

A.5.5 Beam spot-size asymmetry

Geometric arguments predict that the sensivity to a spot size asymmetry $\delta\sigma/\sigma$ is approximately (12 ppm)$\delta\sigma/\sigma$. An upper bound on the spot size asymmetry should be possible from measurements on the laser table of $\frac{\delta\sigma}{\sigma} < 1 \times 10^{-4}$, which would imply a net false asymmetry of about twice the statistical error bar over the course of the run. Spin precision spin flips, including both the $g - 2$ and spin-manipulator slow reversals, will both serve to flip the helicity without changing the spot size asymmetry, and should provide a high degree of cancellation. Assuming roughly equal statistics are collected in each reversal state, the average effect from spot size should be reduced by a factor of 10.

A.6 Strategy for control of HCBA

As described above, modest improvements on the state-of-the-art are necessary to achieve sufficent control on the run-averaged helicity-correlated beam asymmetries. A summary of the strategy is presented here.

The intensity asymmetry requires control at the level of < 10 ppb. As with previous experiments, an automated helicity-correlated feedback on beam intensity will be required to achieve this small value. There does not appear to be any fundamental reason why the conventional asymmetry feedback scheme should not converge to this level. While this is approximately an order of magnitude beyond what will be required for the PREX and Qweak experiments, those runs will provide an opportunity to demonstrate feedback effiency at the required level.

Control of position differences will require careful configuration of the source optics. As is currently done, the optics system will be qualified first with diagnostics on the laser table, and then with measurements of HCBA in the electron beam in the low-energy injector. It is estimated that improvements in the injector measurements are feasible which would enable precision scans of important configuration parameters leading to the verification of injector position differences approaching $\sim$ 20nm. As is required for the PREX experiment, the potential spot size asymmetry will also be bounded in laser table studies at the level of 10^{-4}, which limits the potential effect on the measurement at the level of 1 ppb.

Good optical transport throughout the injector and accelerator is crucial to realizing the benefits of the adiabatic phase space damping. It should be possible to achieve a damping factor approaching 100 (about half of the theoretical maximum) if further improvements in injector diagnostics are made. In combination with a source configuation giving position differences in the injector at the level of 20 nm, the average systematic helicity-correlated offset would lie in the 0.2 nm (0.02 nrad) range, sufficient for this measurement.

If the careful beam preparation succeeds at this level, the dominant source of helicity-correlated beam position difference would be the slow convergence of the random (non-helicity-correlated) beam motion. For this reason, it may be necessary to employ feedback on position differences. The feedback integration period would be long enough to allow small corrections to position differences, which are not likely to interfere with other aspects of beam preparation or delivery. The magnitude of feedback corrections will be monitored for signs of a required reconfiguration of the polarized source.

Several slow reversals will be employed. The insertable halfwave-plate in the source optics will be used frequently, possibly changed at 4-12 hour intervals. A frequent spin-manipulation slow reversal is required to cancel spot size asymmetries, so the injector solenoid slow reversal should be used on a period of approximately 1 week. The $g-2$ energy change spin flip, should be used at least once, dividing the full data set in two. Although it is potentially more disruptive, it is also expected to be the most effective of the slow reversals, and the experiment would benefit from using it as often as once per month.

B Detailed Discussion of the Hydrogen Target

As mentioned in the discussion of the experimental design, our preliminary assessment using the Computational Fluid Dynamics code `FLUENT` is that the E158 target cell is a good starting point for the design of the high power target required for this experiment. Experience with the Qweak target using JLab's high intensity, CW beam is crucial for benchmarking our simulations so that the performance of the new target can be predicted with confidence. We also examined whether sufficient target cooling power will be available on site in the 12 GeV era. This can be a complex and potentially contentious issue since it depends on things which simply are not known today, such as the ultimate heat load of the new SRF cavities during 12 GeV operations. However, extremely helpful discussions with the Cryo Group have suggested one logical and reasonable path forward which we present below.

The following sections contain a detailed discussion on these issues.

B.1 Comparable Targets

Unpolarized LH_2 targets with internal heat dissipation of up to 1 kW have been successfully and safely run in the SAMPLE, HAPPEX, PVA4, G0 and E158 experiments. The LH_2 target for the Q_{weak} experiment is the first target in the world that has significantly exceeded 1 kW in internal heating. It was recently commissioned and successfully operated at over 2.9 kW, higher than its design power of 2.5 kW.

Although these targets could not be more different in geometry and experimental conditions, they all have as a central part a cryogenic closed re-circulation loop, made of a thin-windowed cell traversed by the beam, a heat exchanger, an in-line pump and a high power heater. The central part of the cryogenic loop is the target cell as it is the region where the interaction between the target fluid and the e^- beam takes place. The rest of the loop is designed around the cell to satisfy the needs for cooling power and fluid flow.

In this respect the MOLLER target will have the same conceptual components as previous LH_2 targets. The design will have to satisfy the detector acceptance requirements, and, more stringently for such a high luminosity and high precision experiment, the target density variations that affect the physics measurement will have to be minimized. In nominal running conditions the MOLLER target is rated for 5 kW.

For the first time for such targets, Computational Fluid Dynamics (CFD) simulations were used to design the Q_{weak} target cell. The CFD software engines used were `FLUENT 6.3` and `FLUENT 12.0` developed by Fluent Inc. (now part of ANSYS). The Qweak target was recently commissioned and its measured performance indicates that its design goals have been met. The target has been successfully operated with 3 kW of cooling power. It has been run routinely now at beam currents between 150 and 180 μA. The target boiling contribution to the asymmetry has been measured using several techniques. At 180 μA, the measured target noise is only 46 ppm with a 4x4 mm^2 raster and 960 Hz helicity reversal frequency. The bulk density changes have also been bounded to less than 0.2% at 150 μA. Further experience with the Q_{weak} target will be used to benchmark the simulations, thus reducing technical risk.

B.2 Target Parameters

The Møller experiment at 11 GeV proposes using a 150 cm long liquid hydrogen target cell. The nominal beam intensity is 85 μA and the nominal beam raster size is 5 mm x 5 mm. The nominal running point for LH_2 in the thermodynamic phase space (p, T) is 35 psia (2.38 atm) and 20 K, although these parameters might change slightly depending on the refrigeration solution for the target. In these conditions the liquid is 3.7 K below the liquid-vapor curve and its density is 71.5 kg/m^3. The target thickness is 10.72 g/cm^2 and its radiation length is 17.5 %. The heating power deposited by the e^- beam in the target cell is given by

$$P = I\rho L\frac{dE}{dx} \tag{11}$$

where ρL is the nominal target thickness in beam, I is the beam intensity and dE/dx is the average energy loss through collisions of one electron in unit target thickness. If $dE/dx = 4.97$ MeV/(g/cm^2) for electrons of 11 GeV in LH$_2$ then $P = 4533$ W. For an Al target cell made with beam entrance and exit windows of 0.127 mm (0.005") each, the heat deposited by the beam in the windows, calculated with Eq. 11, is 6.4 W per window. The cumulative beam heating in the target cell is then 4546 W. The nominal parameters of the target and beam are in Table 12. In order to minimize target density variations, all high power LH$_2$ targets run in a closed feedback loop with the high power heater, allowing a constant heat load on the target to be maintained over time. The heater needs to account for beam heating and target power losses to the environment (such as radiative and viscous losses) and maintain a cooling power buffer for the feedback loop. Based on experience with previous such targets, the losses and the buffer account for about 10 % of the beam heating. Taking this into account the Møller target is rated for 5000 W of cooling power in nominal running conditions, which is a factor of 2 higher than the Q$_{weak}$ target rating, and by far the most powerful LH$_2$ target ever built and with the most stringent requirements on systematic effects.

Table 12: *Møller LH$_2$ target and beam nominal parameters.*

Target Parameters		Beam Parameters	
cell length	150 cm	I, E	85 μA, 11 GeV
cell thickness	10.72 g/cm^2	raster	5 mm x 5 mm
radiation length	17.5 %	beam spot	100 μm
p, T	35 psia, 20 K	detected rate	153 GHz
ϕ acceptance	5 mrad (0.3°)	helicity flip rate	2000 Hz
target power	**5000** W	beam power	**4546** W
ρ fluctuations <26 ppm			

The measured detector asymmetry width for the Møller detector is given by $\sigma_m^2 = \sigma_A^2 + \sigma_b^2$, where σ_A is the counting statistics width and σ_b accounts for systematic effects independent of counting statistics, which are typically dominated by the target density fluctuation (boiling) on the time scale of the helicity pair. For the current design parameters, the projected counting statistics width for the experiment is about 80 ppm. Target density fluctuations on the level of less than 26 ppm would contribute only a few % to the measured asymmetry width, σ_m.

B.3 Density Variation

The Møller target will use LH$_2$ as the target material and it thus contributes two important systematic uncertainties on the physics measurement: density reduction and density fluctuation. The equation of state of the target fluid in steady-state isobaric conditions is $\rho(p, T) = \rho(T)$. Density reduction is the effect of the fluid density variation with temperature caused by beam heating over the volume of the target cell illuminated by the beam. A LH$_2$ temperature increase of 1 K causes a density reduction of $\Delta\rho/\rho \approx 1.5$ %. Whenever the beam is on target, a dynamic equilibrium is established in the interaction region, where the temperature of the fluid increases locally with respect to the beam-off condition and the fluid density decreases, resulting in a net reduction of the target thickness in beam. If the target fluid density reduction is e.g. 5 % then the experiment would have to run 5 % longer to get the same statistics as expected from a fixed target density. Density reduction can be predicted analytically for laminar fluid flow and it is usually mitigated by increasing the fluid turbulence in the interaction region.

For the Møller target a laminar fluid flow of 1 kg/s transverse to the beam axis would result in a temper-

Table 13: *Liquid hydrogen targets for parity violation experiments. The first group represents actual operating targets, while the last one is a target under design.*

	p/T/$\dot{m}$	L	P/I	E	beam spot	$\Delta\rho/\rho$	$\delta\rho/\rho$
	psia/K/kg/s	cm	W/μA	GeV	mm	%	ppm
SAMPLE	25/20/0.6	40	700/40	0.2	2	1	<1000 @60Hz
HAPPEX	26/19/0.1	25	1000/100	3.481	4.8x4.8 6x3		<100 @30Hz
PVA4	25/17/0.13	10	250/20	0.854	0.1	0.1	392 @50Hz
E158	21/20/1.8	150	700/11-12	45/48	1	1.5	<65 @120Hz
G0	25/19/0.3	20	500/40-60	3	2x2	1.5	<238 @30Hz
Q$_{weak}$	35/19/1	35	2500/180	1.165	4x4		<50 @250Hz
Møller	35/20/1	150	5000/85	11	5x5		<26 @2000Hz

ature increase of 0.5 K in nominal running conditions and a relative density decrease of less than 1 %, which would be further decreased by turbulence effects and would be negligible in this experiment. A summary of design parameters and target systematic effects for previous and future LH$_2$ targets used in parity violation experiments is presented in Table 13. The quoted target systematic effects for targets that have run before are the measured ones, for the Møller targets they are the desired ones. The two highest power LH$_2$ targets in the world have the most stringent requirements for target density fluctuation compared to the previous targets.

The target density fluctuation effect is usually dominated by the target cell windows region. The heat density deposited by the e^- beam in the thin Al windows is typically one order of magnitude higher than the heat density deposited in LH$_2$. The heat deposited by the beam in the window material is dissipated through conduction in the window material and convection on only one side of the window, the LH$_2$ side, as the other side is exposed to vacuum. The target liquid boils at a window with high probability if two partially correlated effects happen simultaneously: surpassing the critical heat flux and a temperature excursion between the window and the bulk liquid greater than some tens of degrees. Typically for these targets the heat flux from the window to LH$_2$ is much higher than the critical heat flux for boiling. The critical heat flux for LH$_2$ at a wall is on the order of 10 W/cm^2 [42]. The total heat flux at the windows in nominal conditions is 43 W/cm^2 for the G0, 78 W/cm^2 for the Q$_{weak}$ and 25.6 W/cm^2 for the Møller targets respectively. CFD simulations revealed that over the beam raster area the convective part of the total heat flux is 18 W/cm^2 for the G0 target and 33 W/cm^2 for the Q$_{weak}$ target. The temperature excursions determined with CFD for the G0 and the Q$_{weak}$ targets at the windows are on the order 10-30 K. The G0 and the Q$_{weak}$ targets seem likely to develop liquid boiling at the windows. Of these three targets the Møller target has the lowest total heat flux at the windows and careful CFD design could drop the convective part of the total heat flux below the boiling threshold.

From experience with previous LH_2 targets, the effect of density fluctuation is mitigated by optimizing both fluid conditions (flow, turbulence etc.) and beam conditions (raster size, intensity). The measurements done with the G0 target [43] at a helicity flip frequency of 30 Hz indicate a drop by a factor of 2.4 in the magnitude of density fluctuations when the raster size was increased from 2 mm to 3 mm at constant pump rotation, and by a factor of 3.5 when the pump pressure drop was doubled at the same raster size.

For the Møller experiment, we plan to run with a helicity flip frequency (2000 Hz) that is nearly two orders of magnitude greater than the 30 Hz that has been used in the completed Jefferson Lab parity experiments. As noted above, the counting statistics and target density fluctuation asymmetry widths add in quadrature to give the measured statistical width. The advantage of the higher helicity flip frequency is that it is expected to reduce the relative contribution of the target density fluctuations to the measured asymmetry width. As the helicity flip frequency is increased, the counting statistics width increases, while the expectation is that the target density fluctuation width will decrease (or at worst remain constant) with increasing frequency.

To make an estimate of the target density fluctuation width for the Møller target, we use the measured G0 target properties as a starting point. The G0 target has a longitudinal flow design similar to the E158 target, which we are using for prototyping a Møller target cell. The G0 target was run in the CW JLAB electron beam (as opposed to the pulsed beam used in the E158 experiment at SLAC). An upper limit of 238 ppm was observed for the target density fluctuations in the G0 target at 40 μA beam current. We estimate the density fluctuations in the Møller target by using conservative power laws for each of the parameters known to affect density fluctuations. We expect the target density fluctuations to vary inversely with the raster area and linearly with the beam power; these expectations have been borne out by previous target studies. Data from previous targets on the dependence on mass flow rate have not been completely consistent (which could be due to the fact that different target designs were being compared), but the dependence always rises faster than linear. For this estimate, we assume a linear dependence on mass flow rate, which is the most conservative choice.

Finally, we estimate the dependence on helicity flip frequency from an empirical power law measured in Q_{weak} beam tests done in June 2008. Data were taken at helicity flip frequencies of 30 Hz, 250 Hz, and 1000 Hz on both a carbon and 20 cm hydrogen target at a range of beam currents. The hydrogen target available for the test was not one that was optimally designed for minimization of density fluctuations, but we ran at a variety of beam currents to see if our conclusions were valid over a range of "boiling" conditions. The scattered electron rate was monitored with "luminosity" monitor detectors at small scattering angles. The data from the carbon target were used to determine the parameterization of all sources of random noise other than the target density fluctuation effects in the hydrogen target. The result of the work was the target density fluctuation width as function of helicity flip frequency determined at a variety of beam currents. The results are shown in Figure 27. A simple power law ($\sigma_b \propto f^{-0.4}$) describes the data well as a function of helicity flip frequency f for the beam currents of 40, 60, and 80 μA. Data were also taken at 10 and 20 μA, but contamination from 60 Hz power line noise made it difficult to draw meaningful conclusions; a refined analysis will be pursued to try to extract information at those currents. Explicit measurements with the Qweak target at 960 and 480 Hz helicity reversal frequencies verifies that target noise scales according to this empirical power law.

In summary, the assumed scaling arguments for estimating the target density fluctuation widths are: linear in beam power, inversely linear in beam raster area, linear in mass flow rate, and $f^{-0.4}$ in helicity flip frequency. The input parameters for the G0 target are an upper limit of 238 ppm target density fluctuations for a 20 cm long target, 40 μA beam current, 2 mm square raster size, 30 Hz helicity reversal rate, and 0.25 kg/s mass flow rate. The corresponding expected parameters for the Møller target are a target length of 150

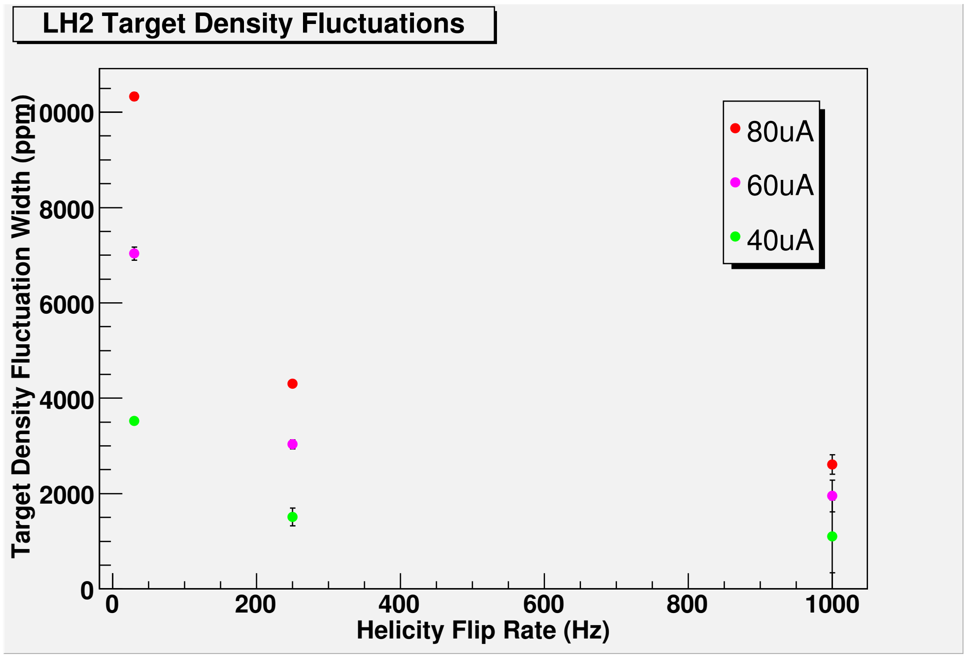

Figure 27: *Target density fluctuation widths versus helicity flip frequency from recent Q_{weak} beam studies.*

cm, 85 μA beam current, 5 mm square raster size, 2000 Hz helicity reversal rate, and 1.0 kg/s mass flow rate. Applying the scaling leads to an estimate that the target density fluctuations for the Møller target could be as large as 26 ppm corresponding to 5% excess random noise.

This will be discussed in more details in section B.6 with the latest Q_{weak} target experience, which shows that the situation is better than the conservative scaling arguments starting from the G0 target information.

B.4 Cell Design

A 150 cm long cell was used in the 55 liter LH_2 target for the E158 Møller scattering experiment at SLAC at 45 GeV and 48 GeV electron beam energies. The E158 target was rated for 700 W beam heating removal and 1000 W cooling power. The E158 target density fluctuations contributed 65 ppm [44] to a Møller detector asymmetry width of 200 ppm at a repetition rate of 120 Hz or about 5 % of the detector asymmetry.

A drawing of the target cell for the E158 experiment is in Fig. 28. The target was designed and built by a group from Caltech led by Cathleen Jones. The cell is made of 3” ID pipe with a 3” inlet and outlet that are connected to the rest of the vertical cryogenic loop. Inside the target cell there are 8 wire mesh rings (see Fig. 28), with a 45^o cut-out and 1.5” diameter clearance in the middle. The rings are to increase fluid turbulence and mixing in the cell. This cell is a natural first candidate for a target cell for the Møller experiment at 11 GeV. For this reason the cell design from Fig. 28 was studied in a steady-state CFD simulation in `FLUENT` under the nominal running conditions from Table 12. The heating from the electron beam was implemented as a uniform power deposition in the volume of the cell illuminated by the rastered beam to yield 4.5 kW in this volume. The cell walls are made of Al and the beam heating in the windows was implemented also as a uniform power deposition to yield 12.5 W. Hydrogen properties are implemented as functions of temperature in isobaric conditions from the freezing point to 300 K. No boiling model was implemented for hydrogen. The mass rate considered was 1.2 kg/s. The cell volume is 7.8 liters. The cell was simulated both with meshes and without. The results from Figs. 29a-29d are for the cell with internal meshes. The global temperature increase of the LH_2 between the inlet and the outlet to the cell is 0.37 K but

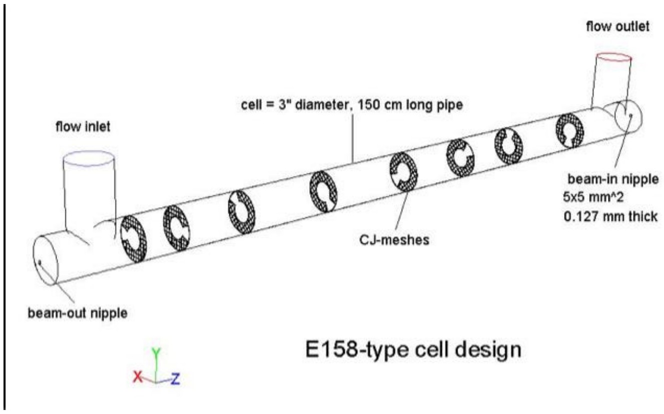

Figure 28: *E158-type target cell design. Note that the fluid flow (left to right) is opposite the electron beam direction (right to left).*

the average over the beam volume is 1.23 K, which yields a LH_2 density reduction of 2 %. The temperature averaged over the cell windows' beam nipples is 30.1 K for the beam-in window and 34.8 K for the beam-out window. The heat flux, predicted by `FLUENT`, from the window nipples to LH_2 is 4 W/cm^2 for beam-in and 8 W/cm^2 for beam-out respectively, which are both less then the critical heat flux for LH_2. *This would indicate that there is a low probability of liquid boiling at the windows.* Although the cell is symmetrical between the inlet and outlet the flow near the end caps of the cell is not. The cap at the inlet (with the beam-out window) experiences a large vortex with very little flow in the middle, where the liquid seems to be boiling. The pressure drop over this cell at this flow rate is 0.49 psid. The cell design would have to be refined to get rid of the bulk liquid boiling, but it looks promising in the windows region.

B.5 Refrigeration

An examination was carried out to ascertain whether sufficient target cooling power will be available on the JLab site in the 12 GeV era. Such an estimate is complex since it depends on things which simply are not known today, such as the ultimate heat load of the new SRF cavities during 12 GeV operations. However, after discussion with the JLab Cryo Group, a logical and reasonable path forward has been established.

If the accelerator delivers electron beams at 12 GeV and all the new SRF cavities continue to show high heat loads, there might be little spare capacity from the new Central Helium Liquefier (CHL). However, the ESR #2 could deliver 4 kW cooling power at 4 K and could be modified to deliver more than 6 kW of cooling power at 15 K and 3 atm. A similarly novel design feature involving the reconfiguration of the existing transfer line has now been validated by Q_{weak}, in order to simultaneously supply both 4 K coolant and 15 K coolant to the target, and in particular, to return both coolant sources on separate lines back to the ESR.

A director's review of JLab cryogenic capacity has been held recently. The final report is available at

`http://www.jlab.org/div_dept/dir_off/ccr/.`

The MOLLER experiment's 5 kW cooling power requirement figures prominently in the report. The report states that the planned ESR #2 by itself has the 5 kW capacity required for the MOLLER experiment. The ESR #2 building is currently under construction, and the refrigerator has been designed (but not yet funded). However, the first of the director's review committee's recommendations is that funding be secured for ESR #2 on a timeline that will make it available for the MOLLER experiment. Finally, the report also

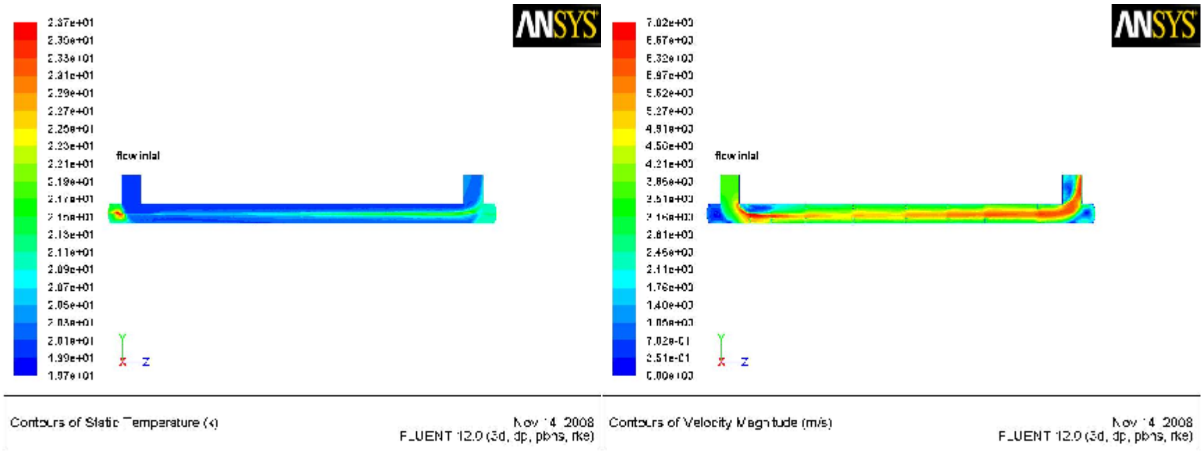

(a) Temperature profile. (b) Velocity profile.

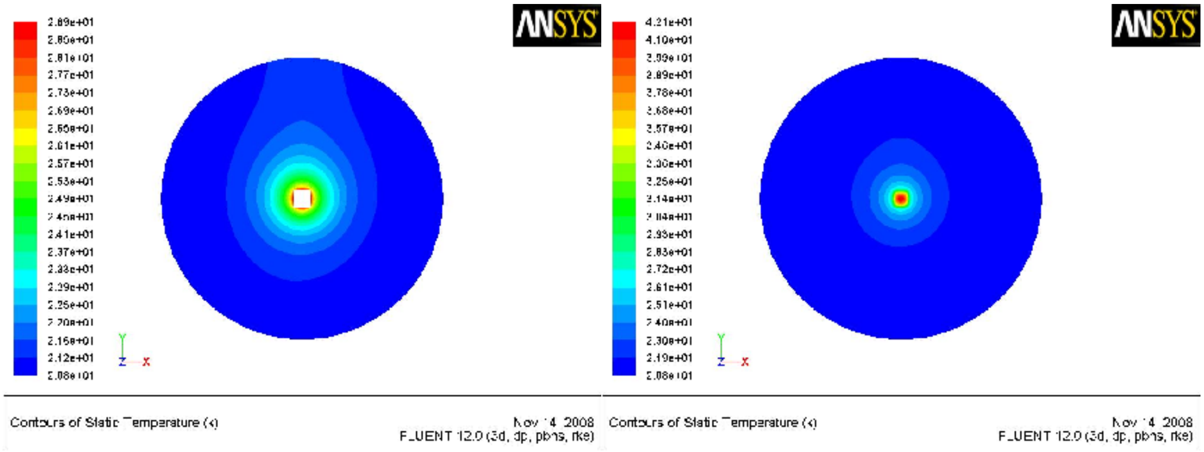

(c) Beam-out window without nipple. (d) Beam-out window with nipple.

Figure 29: *CFD simulations of a E158-type cell in nominal conditions.*

recommends that the Hall A 4K transfer lines be re-evaluated and upgraded for the 12 GeV era in part because they have unusually high heat loads associated with them, and in part to better meet the demands of the 12 GeV era (such as the MOLLER experiment).

B.6 Qweak Target Experience and Expected MOLLER Performance

The design of the MOLLER target, as described in the proposal, is predicated on several novel ideas which were to be tested for the first time with the Qweak target. The Qweak target, we argued in the proposal, is really the prototype for the MOLLER target. This section reviews what has been learned from the Qweak experience in order to see whether those Qweak ideas and design aspects crucial to the Moller LH2 target hold any water.

The most crucial aspect of the MOLLER target design which needs to be validated is the novel use of computational fluid dynamics (CFD) as a design tool. Computational fluid dynamics was used in almost all aspects of the design of the Qweak target. It was used to tailor the cell design in order to optimize the flow, temperature and density profiles across the beam axis in the hydrogen volume as well as at the cell windows. These simulations were used to fix the mass flow required of the target, one of the most crucial design parameters. The pressure head represented by the complicated cell shape was derived by CFD. Analytic calculations for the Qweak target's heater and some aspects of the heat exchanger were checked with CFD simulations. CFD simulations fixed the raster size required for the target and helped us design strategies for various off-normal events. In many respects the novel design which emerged was considered a bit of a gamble, given that CFD was not a proven tool for target design.

The 35 cm long, high power Qweak target has met its ambitious design goals. The target has been successfully operated with 3 kW of cooling power, significantly greater than any target previously built. It has been run routinely now up to 180 μA of 1.165 GeV electrons. The target boiling contribution to the asymmetry widths in the experiment has been measured at a raster size of 3.5x3.5 mm^2 in the beam current range from 50 to 170 μA (Figure 30). The measured performance is in excellent agreement with the expectation estimated from scaling the performance of the G0 target with the CFD model. The bulk density changes have also been bounded to less than 0.2% at 150 μA. This should be compared to the performance of the standard pivot 15 cm machined cells, for which the density variation at 100 μA has been measured to be at the level of 20%. Although the design raster size for the Qweak target was 4x4 mm^2, the target's performance is so good that it is operated routinely at 150 μA with a raster size of only 3.0x3.0 mm^2.

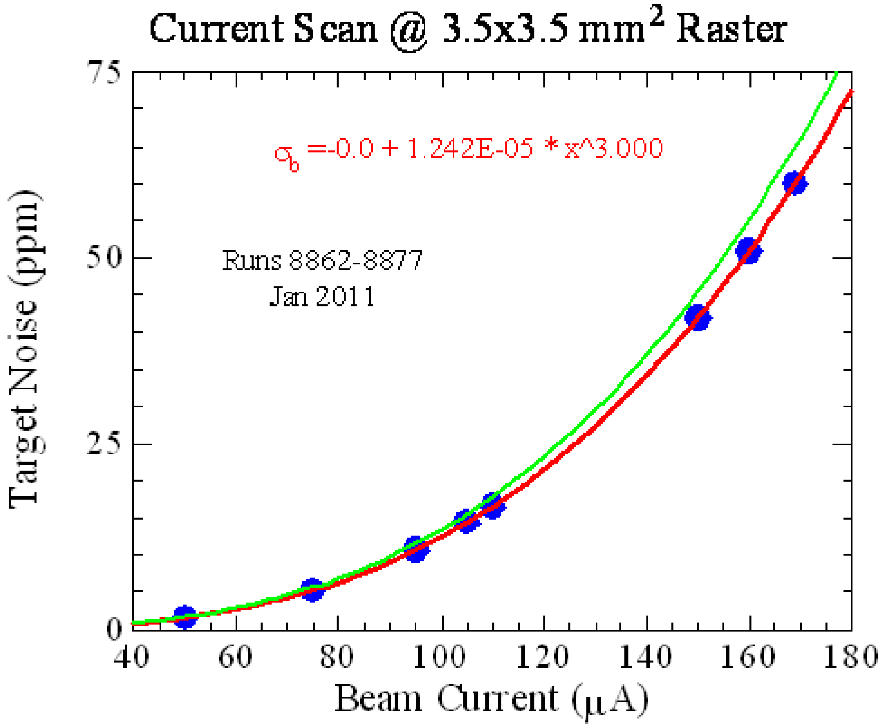

Figure 30: *Qweak target performance: density fluctuation widths versus beam current from recent Q_{weak} measurements. The blue points are measured data. The red curve is a fit to the data. The green curve is another fit, providing a measure of the uncertainties.*

The fact that the Qweak target has achieved all of its design goals validates the use of CFD as a design tool. The expected performance of the MOLLER taregt can now be scaled from the Qweak target performance.The MOLLER target requires the target density fluctuation to be less than 25 ppm at the operation condition of 85 μA with a raster size of 5x5 mm^2 at a helicty flip frequency of 2 KHz. At 85 μA beam current, the measure Qweak target density fluctuation (noise) is about 7 ppm at a raster size of 3.5x3.5 mm^2. At a raster size of 5x5 mm^2, the expected noise is 3.4 ppm. If we scale it with the target length, it will be 15 ppm. Considering the fact that only the noise due to boiling within LH2 will approximately scale with the target length, while the noise due to the boiling at the aluminum windows will be approximately independent of the target length, the expected noise will be less than 15 ppm. Taking into account the factor that MOLLER plans to have the helicity reversal frequency twice of that for Qweak, the density fluctuation will be further reduced.

Since the density fluctuation due to the film boiling at the aluminum windows is often the dominating factor, a study was carried out with the CFD calculations for the MOLLER in comparison with the two Hall C parity experiments (G0 and Qweak). Figure 31 shows the heat flux for the three experiments, both the convective part, which is responsible for film boiling at the windows, and the total. Also shown is the threshold for film boiling. It is interesting to notice that the MOLLER situation is just below the threshold. A careful design may actually eliminate the film boiling.

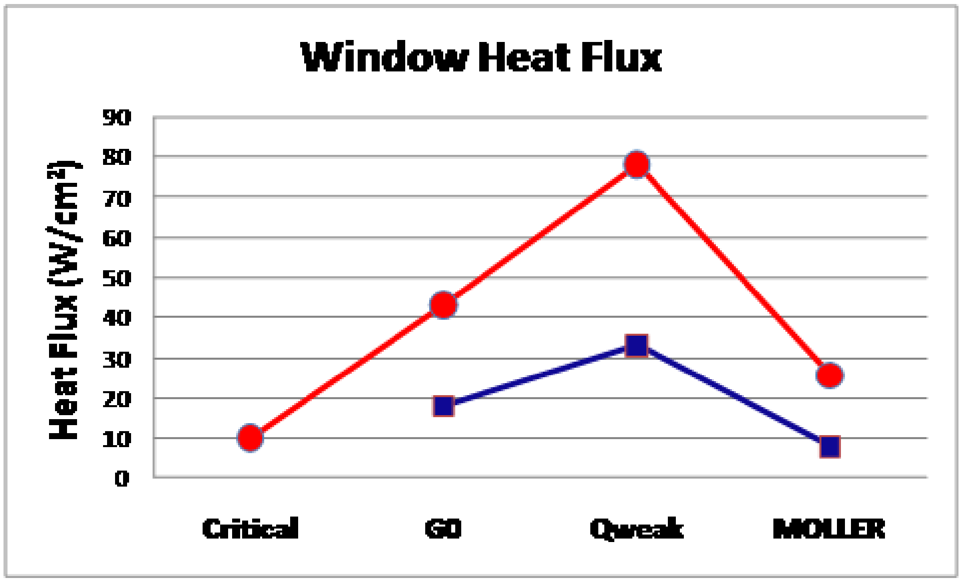

Figure 31: *CFD study of film boiling at the aluminum windows: window heat flux for three experiments (G0, Qweak and MOLLER). The blue points are the convective part of the heat flux, which is mainly responsible for the film boiling. The red points are the total heat flux. The first (red) data point shows the threshold for film boiling.*

We note that the matrix of 24 solid targets that are also part of the Qweak experiment were also designed with CFD. The relationship between temperatures at the center of each target to thermometry scattered around the solid target frame was studied with CFD. Knowing how high these thermometers can safely go, by virtue of the CFD calculations, has made it possible to put more beam current on our solid targets than has ever been done before at JLab.

It also shows that the heat exchanger design process used for Qweak was correct. Note that the Qweak heat exchanger is a completely novel design which combines a 4 K and a 15 K heat exchanger using overlapping heat exchanger coils in the same shell.

It also shows that the high power heater design and fabrication process was correct. The 3 kW heater performance is unmatched. When beam trips occur, or beam is restored to full current, the typical temperature excursions in the target loop thermometers are less than 0.1 K.

The pressure head predicted for the Qweak target at the design mass flow of 1.1 kg/s was 1.2 psi. The head measured with the Qweak target at this massflow is 1.1 psi, in amazingly good agreement with the prediction considering how very difficult it is to calculate this ahead of time. Note that head and massflow are the two most crucial design parameters for most of the target's components.

The fact that the required massflow and pressure head were achieved for the Qweak target also validates the pump design. Problems have been encountered with the Qweak pump bearings, which have led to some down time. However the basic deliverables of the pump (head and massflow) have been achieved at the required values.

Qweak initiated the use of faster helicity reversal as a tool to mitigate the effects of target noise on the experiment. Fast Fourier transforms acquired under a wide variety of conditions during the Qweak experiment's commissioning phase show that this is an important and effective tool for reaching the goals of the experiment, and its effectiveness for the MOLLER experiment is now also validated.

Qweak also pioneered the use of a recovery heat exchanger at the ESR in order to boost the effectiveness of the ESR by making use of the enthalpy of the returning 4 K coolant. The ESR recovery heat exchanger (designed by Rao Ganni for Qweak) has been used for both the HAPPEX-III/PVDIS experiments in Hall A and for Qweak in Hall C. It has been proven to be enormously successful that it boosted the 15K cooling power the ESR can deliver by about a factor of two.

Another novel design feature now validated by Qweak is the re-configuration of the existing transfer line infrastructure in order to simultaneously supply both 4 K coolant and 15 K coolant to the target, and in particular, to return both coolant sources on separate lines back to the ESR. This required using the LN2 supply shield as a 20 K helium return. A small superconducting polarimeter magnet in the Qweak experiment is also fed and successfully operated with this highly unusual configuration.

To summarize: the Qweak target employed a large number of novel and highly unusual ideas to meet its goals. We now know that every single one of these new ideas has worked. This greatly reduces the risk associated with the extensions needed for the MOLLER target. The expected performance in terms of the density fluctuation should meet the MOLLER requirements. The cooling power needed for the experiment has been carefully considered by the lab and solutions are already under way that will insure the experiment's requirements can be met.

C Toroidal Spectrometer

We have already listed the salient features of the spectrometer system in Sec. 3.3. In the following we provide further details of the conceptual design and describe the progression to a buildable coil design.

C.1 Hybrid Toroid Concept

The shape of the hybrid toroid is designed to provide a large range of total $Bd\ell$ correlated to the angle of the track. The conceptual design evolved under the imperative of maintaining a large current in a small volume near the beam line (due to the lowest angle tracks). Idealized currents were found which achieved the desired optical properties, focusing a large range of Møller scattered electron angles and energies, with sufficient separation between the Møller and Mott scattered electron peaks. This original design conformed to the basic requirements of manageable current density and sufficient tolerances for water flow and support structure and was robust under small changes in geometry, but did not take into account the need for a realistic conductor layout.

There were four primary features to the conceptual magnet design:

- In order to maintain sufficient current at realizable density, the magnet fully enclosed the beamline from z=10 meters to z=13 meters.
- The current in the magnet grew from z=10 m to z=13 m, with current returning in 4 different radial paths, spaced along the beamline by about 1 m.
- the back-end of the magnet, with the highest current, juts out to keep the highest-energy Møller-scattered tracks in high field for a longer time, while minimizing the field seen by the Mott-scattered electrons.
- the top of the coil is dropping, over the radial range of accepted flux, so that some tracks receive less $Bd\ell$ by entering the field region comparatively late, or leaving it comparatively early.

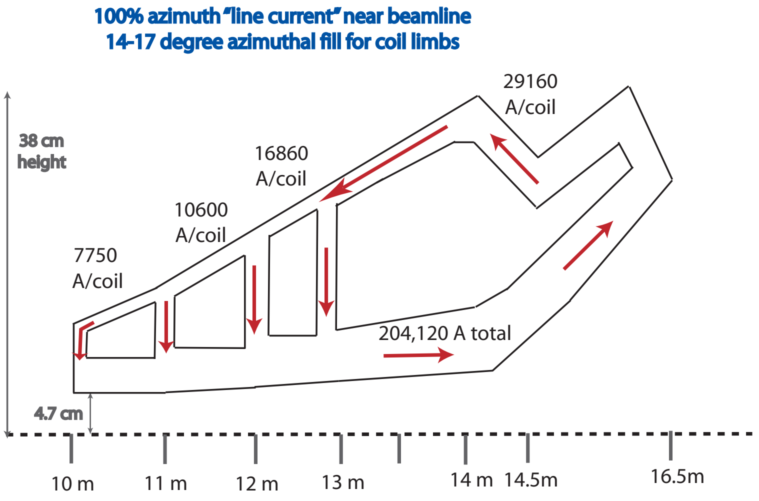

Figure 32: *Schematic of the hybrid toroid design concept.*

Each of the coils in this conceptual design carried around 29 kA, with total power consumption of about 600 kW.

C.2 Detailed Description of Coil Design

In order to achieve a buildable coil design with a realistic conductor layout while achieving the design goals stated in sections 3.3 and above, it was necessary to take into account additional constraints. The most important consideration was to find an actual conductor layout that would not interfere with the scattered electron envelope, but still had a reasonable current density. This was complicated by the need to have multiple current return paths with a minimum bend radius of 5× the radius of the conductor. An additional constraint is that ideally the coils would be wound with a "double-pancake" structure, so that when the conductor is being wound, it can be returned in the second layer by reversing the direction of the winding. The final coil design consists of several individual "double-pancakes" that will fit together, with each pancake designed to be as flat as possible while fitting within the radial and angular acceptances. The segments in z which are formed from the multiple current return paths have values that are as close to the ideal currents as possible.

C.2.1 Conductor Layout

The actual conductor layout was optimized using an iterative procedure, because the scattered electron envelope depends not only on the upstream torus, but also the configuration and current in the upstream parts of the hybrid torus itself. A commercial software program called TOSCA, available from Vector Fields, was used to determine an actual conductor layout by drawing the configuration of individual conductors and then tracking electrons with the correct angle and energy correlations (though lacking radiative effects in the target or other materials) through the fields to check for interferences. The first step was to find a standard conductor size which minimized the current density, if possible. Once a conductor size was chosen, a reasonable layout was designed using a "double-pancake" structure which fit generally into the radial and azimuthal constraints. Tracks were then simulation in TOSCA to check for interferences.

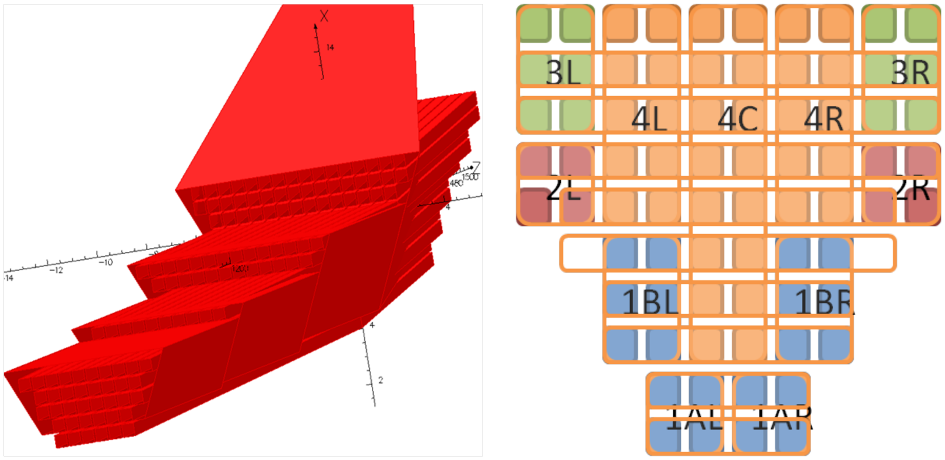

(a) (b)

Figure 33: *Layout of individual conductors within the allowed space at low radius (trapezoidal shapes) in TOSCA for 0.1819 inch OD square conductor (a). Diagram showing the layout for 0.2294 inch OD square conductor, color-coded and labeled by how they are wound in individual "double-pancakes" (b).*

The biggest constraint on the coil cross section comes at the most downstream current return path, at the z location where all of the current returns. In addition to taking into account the water-cooling hole, the space needed for insulation between individual wires was considered. The closest that a coil comes to the center of the beamline is 5σ of the multiple scattering angle (estimated to be 0.515 mrads) plus 1/2 inch for aluminum supports and tungsten shielding (1/4 inch each). In order to fit the conductor radially (beneath the radius of the lowest angle Møller scattered electrons at that z location) it is necessary to nearly fill the full azimuth in a roughly trapezoidal cross-section. The smaller the conductor, the easier it is to fill the shape of the acceptance, except that more of the area is taken for insulation between the conductors, resulting in a higher current density. With larger conductors, there is unutilized space near the edges of the acceptance, so the choice of the size of the conductor does not impact the current density significantly; in all cases the current density ranged from 1550 to 1600 A/cm^2. However, the smaller the conductor, the easier it is to achieve the idealized currents used in the original field map, leading to the choice of 0.1819 inch OD conductor which was presented to the Magnet Advisory Committee in August 2010.

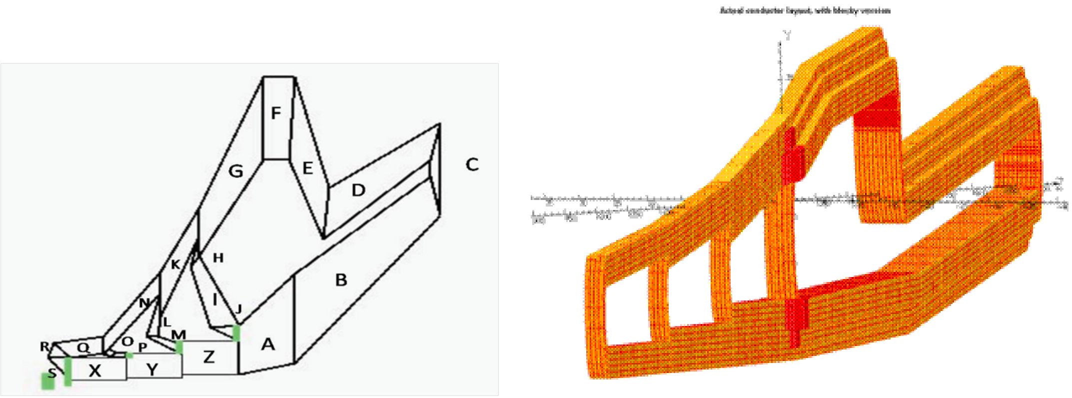

(a) (b)

Figure 34: *Conceptual model of a single hybrid coil, with the segments labeled for reference (a). Model of the actual conductor layout in TOSCA (red) overlayed with the blocky model used for simulation and production of the maps (orange) (b).*

When designing the layout, it was necessary to consider how the coils would be constructed. Figure 33, (b) shows the scheme of how the individual double-pancakes will be put together in a cross-section at z=1300 cm. Currently the design has the conductors as closed loops. Starting at z=1300 cm at the inner radius part of a coil, or segment A in Figure 34, (a), and moving upstream toward segment Z, the conductor in pancakes 1B, 2 and 3 (left and right, or L and R) is bent inward toward the center of the coil, and continues upstream with the conductor in pancakes 1A (L and R). The conductor in pancakes 4 (L, C, and R) bends radially outward to form the current return path of segments J, I, and H. At z=1200 cm, pancakes 3 (L, R) bend radially outward to form the current return path of segments M, and L, and then at z = 1100 cm, pancakes 2 (L, R) form the current return path of segments P and O. Finally, at the upstream nose of the coil, pancakes 1A and B (L, R) bend radially outward to form the current return path of segments S, R and Q. At large radius, the conductor in the pancakes continue downstream and come together again at z=1300 cm and bend outward from the center of the coil so that they have the same cross-section as at the inner radius. The pancakes as labeled in Figure 33, (b) will be wound separately and then put together with the orange ones in the middle, then the green, red and blue ones fitting around them.

C.2.2 Suggestions from the Magnet Advisory Committee

The Magnet Advisory Committee was positive about the design of the magnet, and offered suggestions on how to improve the design and the presentation of the specifications of the magnet. They were not concerned with the size of the current density so much as the size of the water-cooling hole in the chosen conductor size. It was suggested that chilled water, flowed fast enough, would work for this current density, but that faster water flow rates would also increase the erosion rates. They all agreed that a water cooling hole of at least 0.125 inches ID round would eliminate concerns about back-flows and eddies in the bends in the magnet, which could lead to the build-up of oxides that could cause a plug which would limit the long-term operation of the magnet. The possibility of mounting the coils inside the vacuum pipe was suggested, which would allow for a much simpler vacuum enclosure design, which would reduce the expense of conforming to the ASME standards for the complicated petal-shaped beamline. There was some concern about manufacturing tolerances for the coils which will need to be considered carefully. The magnetic forces on perfectly symmetric coils are very small, but they cautioned that the support structure would need to account for forces on asymmetric coils. They also requested more details about the geometry of the field. Work is ongoing to develop a conceptual design for the support structure (see Figure 35) as well as studying the tolerances and the effect of asymmetric coils on the magnetic forces.

C.2.3 Summary of Coil Specifications

In order to achieve the necessary field integral while fitting the coils within the sectors behind the collimators, the hybrid toroid is a very long and skinny water-cooled copper resistive magnet (see Fig. 35). The full length of the magnet is ∼7 m and the outer radius of the torus is ∼40 cm, but each coil weighs only 555 lbs. Based on suggestions from the Magnet Advisory Committee, the chosen conductor size is 0.2294 inch OD square with a water-cooling hole of 0.128 inch (round) with 0.08 mm of insulation (0.04 mm half-lapped). All of the bends take into account a minimum bend radius of 5× the conductor OD (for mechanical considerations). With conductor this large, there is more space at the edges that is open in order to avoid interference with adjacent coils, but the current density is still only 1551 A/cm^2.

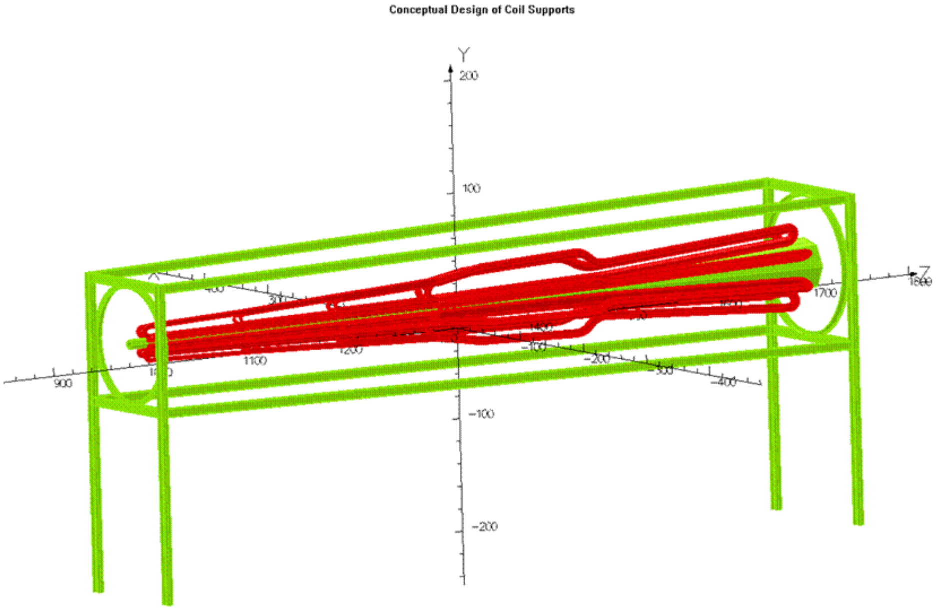

Figure 35: *Hybrid toroid with no z scaling. Conceptual design for magnet supports also shown.*

Further work is needed to develop a water-cooling scheme and to study the manufacturing tolerances and the effect of the magnetic forces on asymmetric coils. Preliminary calculations suggest that the magnet, which has a total power of 765kW, can be cooled with 4 turns per loop, which would be 19 loops, or 38 water connections per coil. It is hoped that it could be made to work with 6 turns per loop, so that the individual pancakes can be made from loops with either 4 or 6 turns. Water and electrical connections can be made at the tail (segment B) and at the top (segment F) with some modification from the ideal layout for access to the conductor in the inner part of the coil cross section (portions of 4 (L, C and R), see Figure 33). The effect of the electrical connections on the scattered electron envelopes has not yet been studied. A preliminary study of the magnetic forces on the coils indicates a modest centering force of less than 3000 lbs. per coil, with a force along the beamline (z-direction) of 50 lbs. (due to the asymmetric shape). For perfectly placed coils, the force in the azimuthal direction is negligible.

C.3 Simulated Properties of the Spectrometer

The simulation of the properties of the MOLLER spectrometer was done using the GEANT4 framework [45]. The simulation was run with three different particle generators which produced Møller electrons, Mott electrons and electrons from inelastic ep scattering, respectively. In each of the generators, electrons are generated with random vertex positions, with z chosen along the length of the target, and the x and y positions chosen within ± 2.5 cm in order to simulate the effects of the raster. A scattered electron is produced from the post radiated beam and the appropriate cross section for the process in question, with a random azimuthal angle. The scattered electrons are propagated through the geometry which consists of collimators, magnetic fields for the two toroids, and a detector plane. The detection plane was chosen to be 28.5 m downstream of the center of the target, where the Møller electrons have their tightest radial focus. At this position the ep elastic (Mott) peak and the peak due to Møller electrons are separated by more than 20 cm.

For the conceptual version of the hybrid torus, a code was written to do a Biot-Savart calculation of the fields for the idealized current layout. This field was then read-in to the GEANT4 simulation. TOSCA was used to produce field maps for various versions of the the actual conductor layouts for the upstream and hybrid toroids, as well as for a TOSCA version of the idealized currents for comparison. Using a combination of TOSCA and GEANT4 simulations, the detailed layout of the actual conductor was optimized to achieve similar focusing properties to that of the field map for the idealized currents of the conceptual hybrid torus.

C.3.1 Properties of the Idealized Hybrid Field

The position of the Møller electrons at the z=28.5 m plane in cylindrical coordinates (radius vs. azimuthal angle ϕ) is shown in the left of Figure 36. Here we establish the color convention which will be used in future plots - red for the detector in the center of the open sector, blue for the detector in the center of the closed sector and green for the detector which straddles the open and closed sectors. For quantities that are azimuthally symmetric, the various detectors of the same "color" will have the same distribution, and for the purpose of the following plots, are combined. The plot on the right of Figure 36 shows the distribution of Møller electrons as a function of ϕ_{wrap}, the azimuthal angle from the center of the nearest open segment, plotted in total expected rate (GHz) for all sectors for a beam current of 85 μA.

The radial distributions of scattered electrons from Møller, elastic e-p and inelastic e-p scattering have been discussed in Sec. 4.5.1, as shown Figure 19. The primary source of background is the result of initial and final state radiation in the target from Mott scattered electrons. The anticipated position of the Møller electron detector is a ring with inner radius 0.88 m and outer radius 1.00 m, also shown in Fig. 19. The integral of the expected rate within this region is 154 GHz for the Møller electrons and 12.6 GHz for the Mott electrons - a background of 7.6%. If the calorimeter is a "shower max" detector, then the background would be 8.3% due to the slightly higher average energy of the background electrons. Figure 37 shows the Q^2 distribution of the background from elastic e-p scattering that is accepted by the detector; this distribution is relevant for estimating the size of the background correction.

Figure 38 shows the E' and θ_{lab} distributions for Møller electrons that hit the main detectors. One can

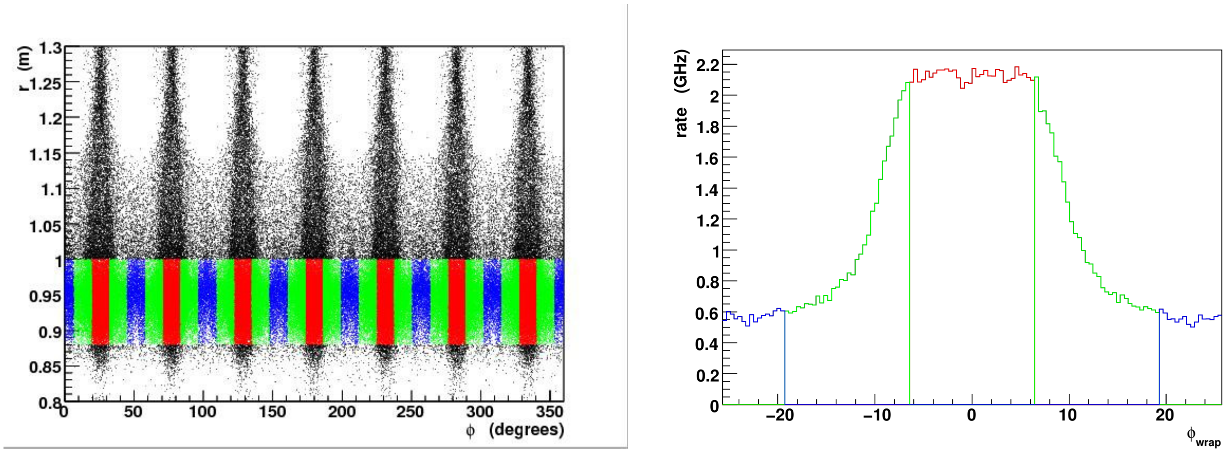

Figure 36: *Møller electrons in the z=28.5 m plane in cylindrical coordinates (radius vs. azimuthal angle ϕ). The detected particles are colored according to which detector they hit, red for the detector in the center of the open sector, blue for the detector in the center of the closed sector and green for the detector which straddles the open and closed sector. On the right is the rate of Møller electrons detected as function of ϕ_{wrap}, the azimuthal angle from the center of the nearest open sector.*

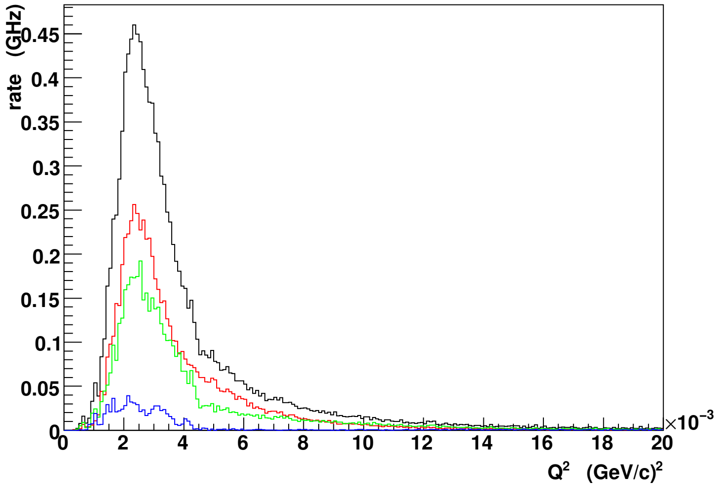

Figure 37: *Rate of Mott electrons detected as function of Q^2, the square of the four momentum transfered in the scattering. Color convention from Fig. 36.*

see that the “red” detector contains mostly the higher energy, forward Møllers, the “blue” detector is mostly the lower energy, backward Møllers and green has a mixture of both. The numbers relevant for estimating detector rates and predictions for asymmetries are listed in Table 1.

C.3.2 Properties of the Actual Conductor Layout

The field calculation for the conceptual hybrid design was verified by directly comparing the actual field values and by comparing the results of GEANT4 simulations using the different field maps. The comparison

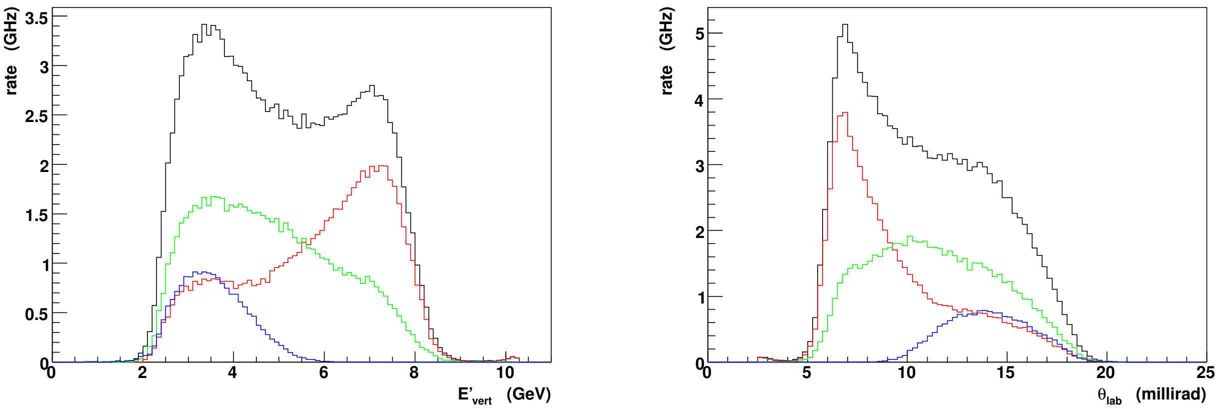

Figure 38: *Rate of Møller electrons as a function of E'_{vert}, the energy of the scattered electron immediately after the interaction (left), and θ_{lab}, the scattering angle in the laboratory frame (right). Color convention from Fig. 36.*

of the fields (T) for a radius of 15 cm shown in Figure 39 is of the primarily azimuthally (de-)focusing component (B_x in this sector) vs. z. At each z location there are 5 points in ϕ. The top plot is for $-25 \leq \phi \leq 20$, the next is for $-20 \leq \phi \leq 15$, etc., with the bottom plot for $-5 \leq \phi \leq 0$. The field of the conceptual hybrid is shown in red, and the TOSCA version is shown in black. The black points are not visible for the most part because they are directly beneath the red points. The top plot shows some extra scatter in the red points because this is actually within the location of conductor in the model. TOSCA seems to handle the calculation of the fields at these points in a relatively smooth manner. The results of the comparison using the GEANT4 simulations are also very similar, with small differences due to the fact that the geometries of the TOSCA version did not exactly reproduce the idealized current distribution.

A default actual conductor layout has been designed which yields similar simulated properties as that of the idealized currents in the conceptual hybrid design. The magnet which was presented to the Magnet Advisory Committee yielded properties that were remarkably similar to those of the conceptual hybrid. When the suggestions from the committee were taken into account, it was necessary to perform some optimization of the resulting coil geometry in order to get back to similar focusing properties. Much of the optimization was done using TOSCA simulations of the Møller and Mott electrons, with the proper scattering angle/energy correlations. The final comparison requires GEANT4 simulations to account for radiative effects. Figure 40 shows some of the progression of the ϕ_{wrap} and θ_{lab} distributions from the conceptual hybrid to the default actual conductor layout which is being used in the simulation for other studies.

The conceptual field map had a ϕ_{wrap} distribution which was relatively flat. This distribution becomes more rounded in the actual conductor layout versions due to additional azimuthal pre-focusing when the electrons pass close to adjacent coils at the inner radial part of the coil, especially in the upstream toroid. Thus the actual conductor layouts seem to have more low angle electrons in the "red" or open segment. The rates for the default field are 155 GHz, 14 GHz and 0.5 GHz for the Møller, Mott and inelastic ep electrons respectively, for a background rate of 8%. In the bottom plot of Figure 40 there is an additional bump in the θ_{lab} distribution at high angles because the collimators have not yet been optimized for this field map. Figure 41 shows a comparison of the radial and θ_{cm} distribution of the conceptual field map and that of the default actual conductor layout. The radial distribution of the default map is slightly wider and is centered at a slightly larger radius than for the conceptual field, while the θ_{cm} distribution is slightly more unbalanced in favor of the larger angles. It is desired that the forward and backward acceptance be very similar, both

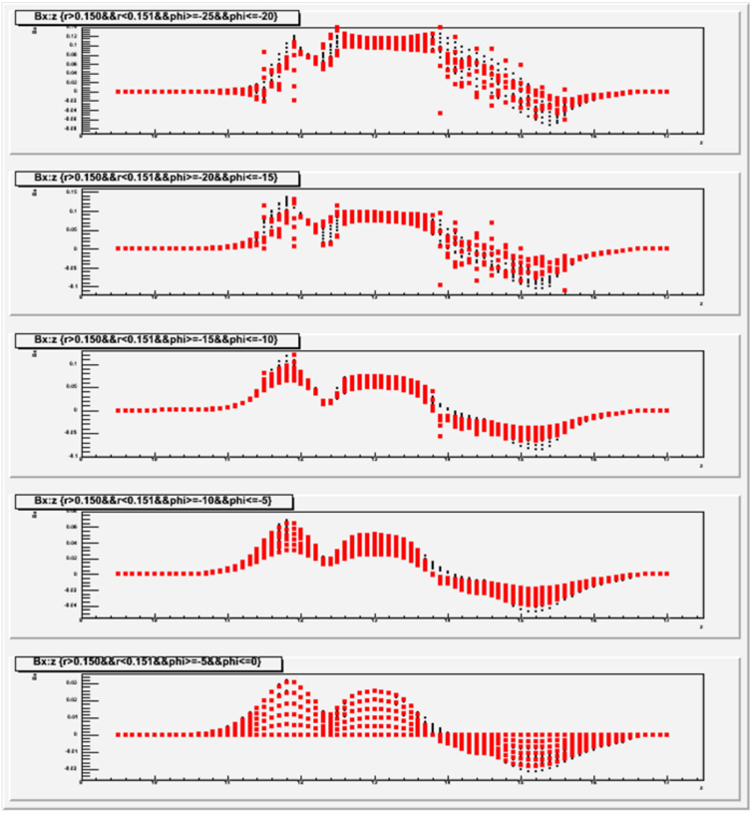

Figure 39: *Plot comparing the* B_x *component of the magnetic field (T) vs.* z *(cm) of the conceptual hybrid (red) and the TOSCA version (black) of the conceptual hybrid for a radius of 15 cm for different bins in* ϕ*.*

because we want full azimuthal acceptance for the accepted range of scattering angles (see Section 3.3) and because the transverse asymmetry will cancel more fully (see Section 4.3). Further optimization of the coil geometry and optimization of the collimator is needed to improve these properties.

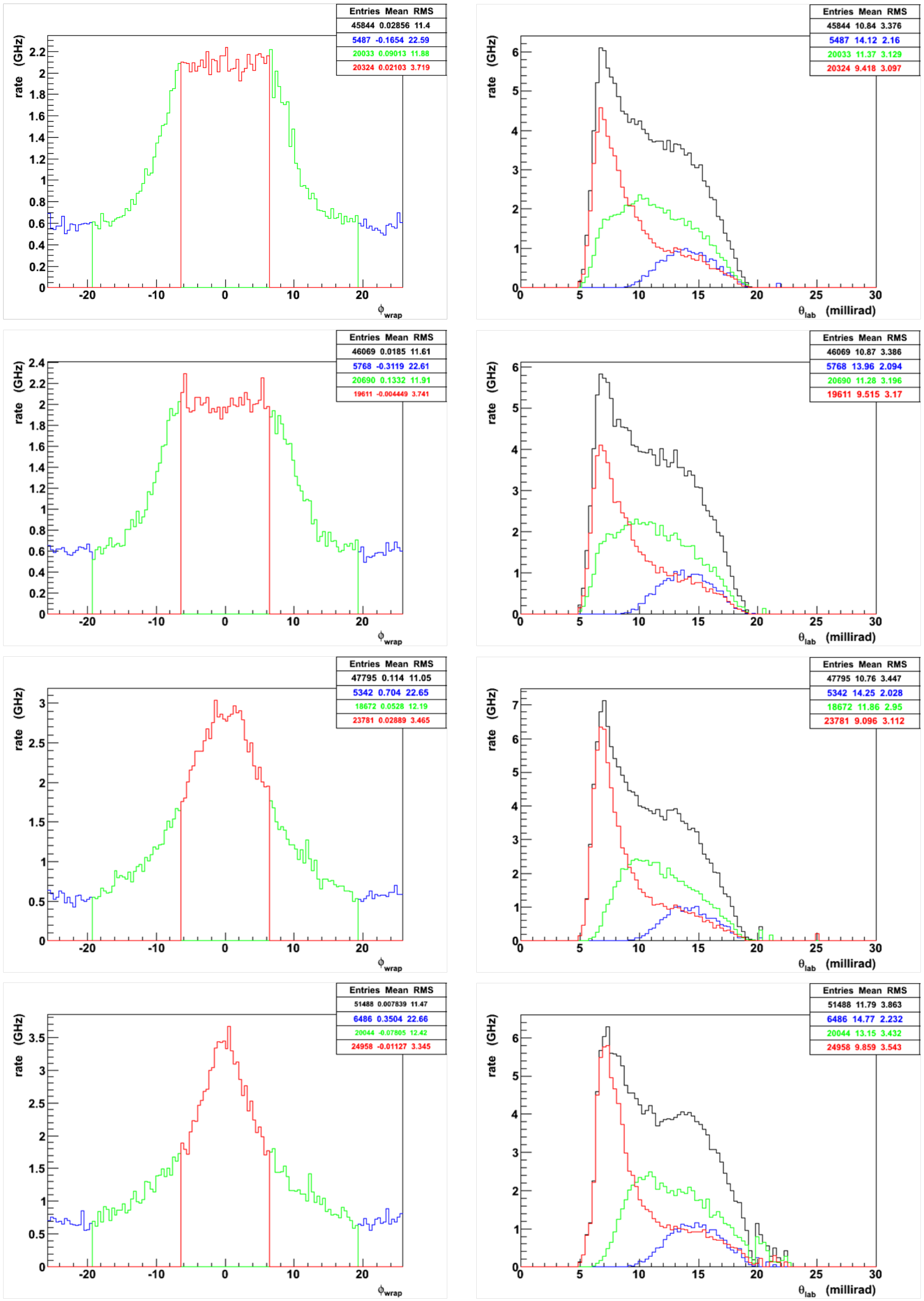

Figure 40: *Plots showing the progression of changes in the ϕ_{wrap} (left) and θ_{lab} (right) distributions from the conceptual field (top). The conceptual field was first verified using TOSCA (second row) and then the actual conductor layout which was presented at the Magnet Advisory Committee was developed (third row). The default field (bottom) is the result of optimization of the conductor layout which takes into account the suggestions from the Magnet Advisory Committee. Color convention from Figure 36.*

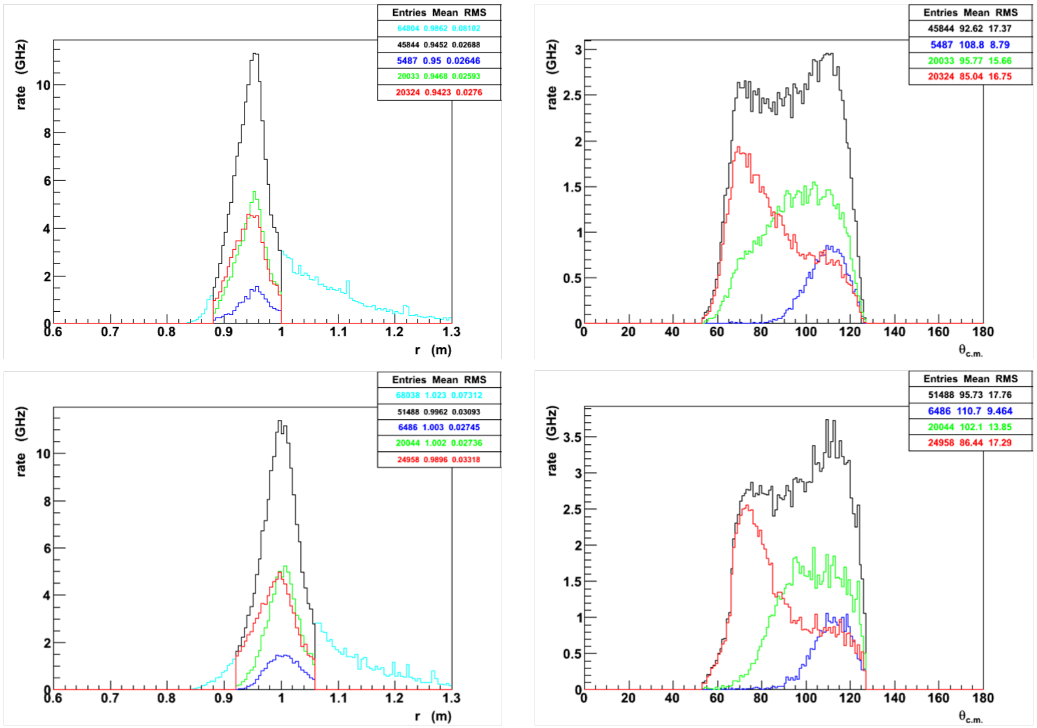

Figure 41: *Plots comparing the radial (left) and θ_{cm} (right) distributions of the conceptual field (top) and the field for the actual conductor layout (bottom). Color convention from Figure 36.*

D Integrating Detector Considerations

We have discussed the requirements of the detector systems in Sec. 3.4 In the following sections, we describe some important considerations of the main integrating detectors discussed in Sec. 3.4.1.

D.1 Current-Mode Signal Magnitude

As can be seen from the discussion in Sec. 3.4 and in Fig. 15, the largest signal will be in the fifth radial quartz detector, which will intercept most of the Møller "peak". For this specific radial bin, we plan to have 84 azimuthal bins. The azimuthal binning is highly non-uniform (see Fig. 36 in App. C); the highest flux in a single quartz detector will be about 5 GHz. The Cherenkov light from each detector will be collected by a single 2" PMT with UV glass windows and will conservatively register 15 photoelectrons per track. With the PMT gain adjusted to 675, the resulting signal amplitude will be

$$I_{anode} = 5.0 \text{ GHz} \times 15 \text{ pe/track} \times 675 \times 1.6 \times 10^{-19} e/C = 8.9\ \mu A.$$

This is a large signal, and still below the nominal 10 μA maximum usually recommended by PMT manufacturers for good long-term stability.

Another consideration for the PMT operational envelope is the *cathode* current of 11 nA. This is far too much current to draw from a standard semiconducting bi-alkali cathode without collapsing the voltage in the center of the cathode, causing defocusing and loss of gain. Hence we will either use a conducting S20 ("multi-alkali") cathode as used in Qweak, or a cathode with thin conducting grid laid across a bi-alkali cathode. The trade-offs are a higher thermionic emission noise in the case of the S20 cathode (which is only an issue at the low rate of the event mode studies), versus reduced quantum efficiency in the case of the cathode overlaid with the conducting grid. The choice will require detailed study. The current-mode PMT parameters are summarized in Table 14.

D.2 Event-Mode Signal Magnitude

Event mode operation is helpful for verifying the magnetic optics and essential for detailed background studies. JLab's CW beam and the flexibility of PMTs allows the detectors to be reconfigured for event-mode operation simply by reducing the beam current, increasing the PMT high voltage, and routing the signal from the parity ADCs (which integrate in 1 msec bins) to flash ADCs (which integrate in bins of a few nsec). At a gain of 1×10^7, the average voltage pulse across a 50 Ω termination is

$$V_{signal} = I_{signal} \times R = (15pe \times 10^7 \times 1.6 \cdot 10^{-19} C/e/10^{-8} sec) \times\ 50\Omega = 120 \text{ mV}$$

which is a robust signal. Even a single photoelectron signal of 8 mV, produced for example by Compton scattering of a few MeV gamma-ray background in the radiator, could be easily observed.

A modest rate of only 100K tracks/second would require the beam current be reduced to 2.25 nA. By employing a combination of laser attenuator and narrow chopper slit, the JLab injector group has provided stable beam to Hall C well below 1 nA for Qweak calibration studies. The beam position is checked at regular intervals by wire scanners. The event-mode PMT parameters are also summarized in Table 14.

D.3 Radiation Hardness

Radiation damage is in principle a concern, since Cerenkov light production occurs predominantly in the UV, which is exactly where loss in light transmission first shows up. For example, the familiar "yellowing" of lead-glass is due to the loss of transmitted light at the blue end of the spectrum. The dose to the artificial, fused-silica radiator material from the $e + e \rightarrow e + e$ events will be only 15 MRad by the end of the

Table 14: *Parameters for the PMT signals from the quartz detector with the largest flux.*

Parameter	**Value**
Total PMTs	252 (6×28 and 1×84)
current mode:	
$I_{cathode}$	11 nA
gain	675
I_{anode}	8.9 μA
non-linearity (goal)	$5{\times}10^{-3}$
pulsed mode:	
$I_{cathode}$	0.24 pA at 100 KHz
gain	$1{\times}10^{7}$
I_{anode}	2.4 μA
V_{signal} (no amp.)	8 mV for 1 pe; 120 mV for 15 pe
non-linearity (goal)	$< 10^{-2}$

experiment. Given the average path length in the radiators of only a few cm, and our non-agressive short wavelength cutoff of 250 nm set by the UV glass of the PMT windows, no measurable loss is transmission is expected. This is ideal since it means that the photoelectron yield and any detector biases (e.g., with respect to Q^2) will be stable throughout the experiment.

All other detector construction materials in the beam envelope (such as radiator supports) must be vetted for susceptibility to damage under 15 MRad dose. Degradation by potentially elevated ozone and nitric acid levels may also be a factor in the choice of detector materials.

E Electronics

With little or no modification, the low-noise electronics developed for the Qweak experiment by TRIUMF should be suitable for the 11 GeV Møller measurement. Signals handled by the front end electronics are shown schematically in Figure 42 for the quarz detector with the largest flux of about 5 GHz. The gain of the photomultiplier will be adjusted to yield an anode current of 6 μA, depending on the measured flux in each detector. The current signal is converted to a voltage by a transimpedance preamplifier located close to the detectors. The voltage signal goes to electronics outside the Hall where it is sampled at 500 KHz with an 18-bit ADC. These digitized samples are then integrated over each spin state in an internal FPGA. The signal levels anticipated will be similar to those of the Qweak experiment, so the same, or very similar, electronics will be appropriate.

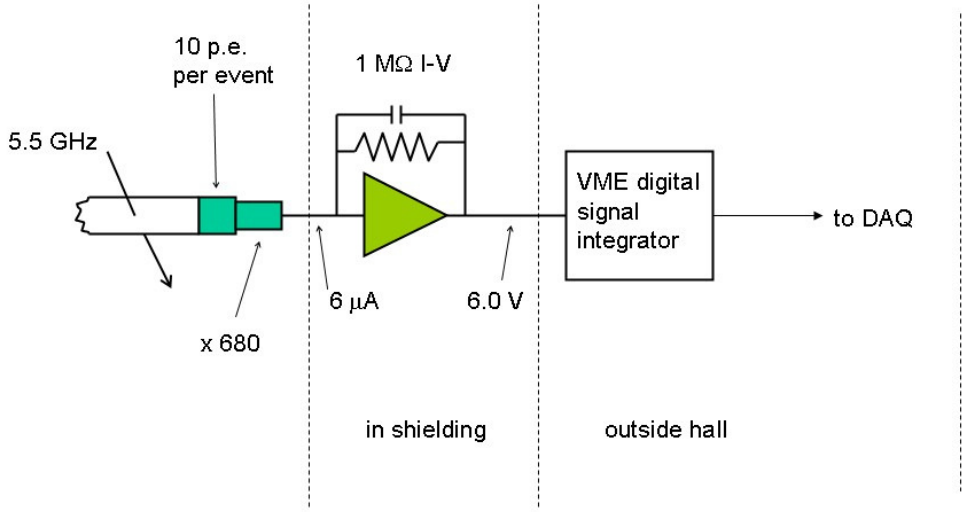

Figure 42: *Possible front-end signals assuming a 5.5 GHz event rate and 10 photoelectrons per event. The photomultiplier gain is set to deliver 6 μA to the 1 MΩ current to voltage preamplifier.*

E.1 The TRIUMF Electronics

Preamplifiers Figure 43 shows one of the preamplifiers built for the main detectors of the Qweak experiment. The main features are:

- Gain: V_{out}/I_{in} = 0.5, 1, 2, or 4 $M\Omega$, switch selectable.
- Output: ±10 volts. Adjustable ±2 V offset. Drives 130 m RG-213 cable.
- Input: current limit set by gain and 10 volt output limit.
- Power: +5 VDC on Lemo connector.
- Bandwidth: $f_{3db} = 26$ kHz.
- Noise: 0.5 $\mu V/\sqrt{\mathrm{Hz}}$ referred to output with 1 MΩ gain setting. (Amplifier noise specification assumes the input capacitance of 5 m of RG-62.)
- Packaging: two channels per 80 mm x 70 mm x 28 mm box.

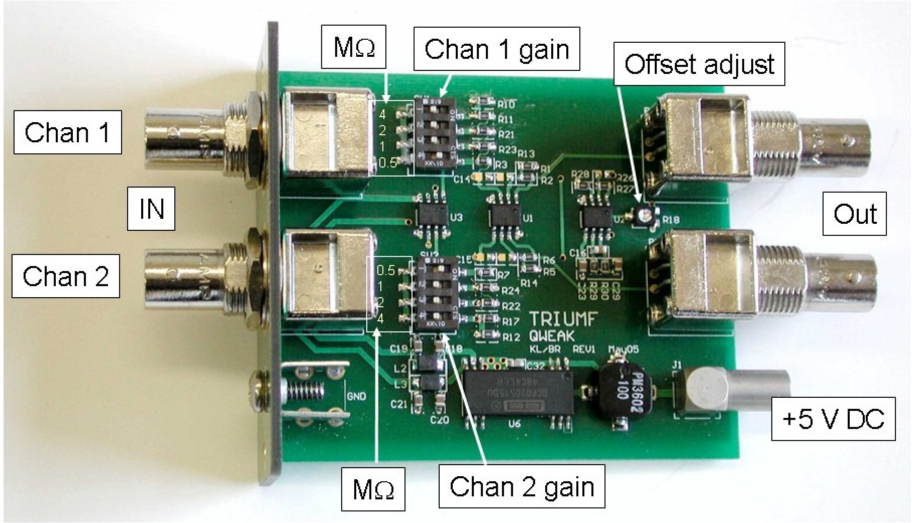

Figure 43: *TRIUMF current-to-voltage preamplifier for the Qweak experiment.*

Digital Integrators Figure 44 shows a TRIUMF digital integrator built for the Qweak experiment. The module has 8 channels in a single width VME module. The main features are:

- Trigger: external NIM signal or internal trigger selectable.
- Integration time: selected as a number of samples, up to 1/30 second.
- Sample rate: selectable up to 500 ksps. 18-bit ADCs.
- Clock: internal 20 MHz or external NIM selectable.
- Input: ± 10 volts. High impedance quasi-differential.
- Output: 32 bit sum. The integration period may be sub-divided into up to four blocks. No dead time between blocks.
- Anti-aliasing: 5-pole filter with 50 kHz cutoff.

E.2 Performance

Table 15 shows that based on reasonable assumptions about the main detector signals on the Møller experiment, the Qweak electronics seem suitable. Noise in the table is referred to the preamp output. The total electronic noise is negligible compared to counting statistics. A null-asymmetry test with a battery-driven current source could be made in one shift at the part per billion level, or 0.1 ppb in 30 days.

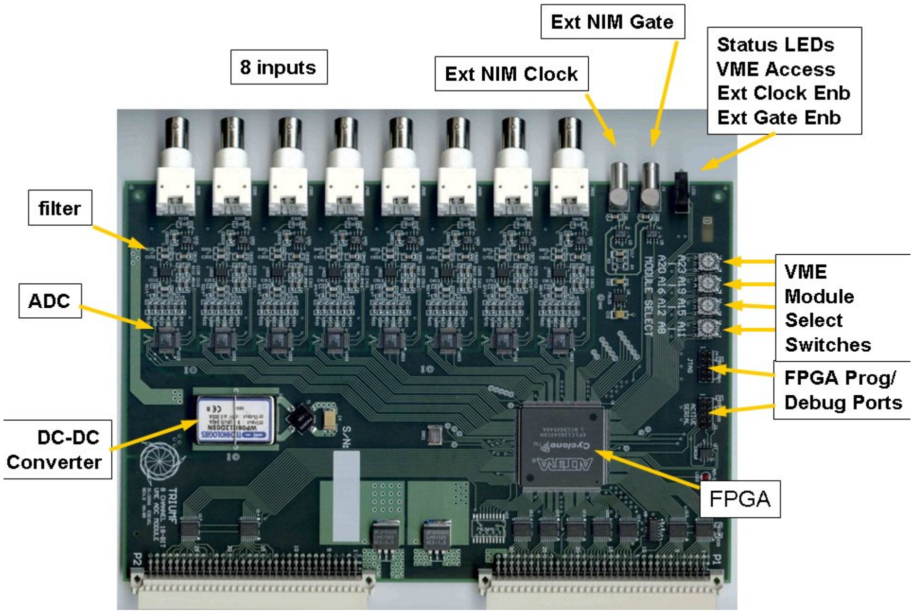

Figure 44: *TRIUMF VME-based digital integrator for the Qweak experiment.*

Table 15: *Comparison of various sources of noise assuming the signals of Figure 42. "Beam on" shot noise is equivalent to counting statistics. The electronic noise is based on tests with TRIUMF electronics built for the Qweak experiment. The electronic noise alone is negligible compared to counting statistics. A null test with a noiseless battery could be made to* $\leq 10^{-9}$ *(one ppb) in a day.*

Type of Noise	charge quantization (e)	Spectral density μV/$\sqrt{Hz}$	RMS Noise in 500 Hz BW (1 ms integral)	RMS Noise in 50 KHz BW (VME input)
"beam on" shot	6800	114	2560 μV	25,600 μV
LED test shot	680	36	800 μV	8,000 μV
battery test shot	1	1.4	31 μV	310 μV
preamp		0.5	11 μV	110 μV
digital integrator		1.3	29 μV	290 μV

F Compton Polarimetry

Compton polarimetry is a very promising technique for high precision polarimetry at beam energies above a few GeV. Beam interactions with a photon target are non-disruptive, so Compton polarimetry can be employed at high currents as a continuous polarization monitor. The photon target polarization can be measured and monitored with a very high precision, and the scattering between a real photon and free electron has no theoretical uncertainty, such as the atomic or nuclear effects which can complicate other measurements. Radiative corrections to the scattering process are at the level of 0.3% and are very precisely known. The SLD collaboration achieved an uncertainty of 0.5%, which demonstrates the feasibility of very high accuracy Compton polarimetry.

F.1 The Hall A Compton Polarimeter Baseline Upgrade

As pictured in Fig. 45, the Hall A Compton polarimeter is located in a chicane, about 15 meters long, just below the beamline. After modification of the bend angle to accommodate 11 GeV running with the existing chicane magnets, the electron-photon interaction point will be 21 cm below the primary (straight-through) beamline. After the interaction point, the electron beam is bent about 3.5 degrees by the third chicane magnet and then restored to the main beamline. The scattered electrons are separated from the primary beam and detected using silicon microstrips, just before the fourth chicane magnet. Scattered photons pass through the bore of the third chicane magnet to be detected in a calorimeter.

For the baseline upgrade, the photon target is planned to be a 0.85 cm long Fabry-Perot cavity containing up to 3 kW of green (532 nm) light. The laser light is polarized using a quarter-wave plate, and can be toggled between opposite polarizations of highly circularly polarized light. The polarization of the transmitted light from the cavity is continuously monitored, and related to the laser polarization at the interaction point through a precisely measured transfer function. The feedback loop which locks the laser to the cavity resonance can be disabled to enable backgrounds from all non-Compton-scattering processes. To reduce overhead from the time required to re-lock the cavity, the transition between laser states is typically performed with a period of 1-2 minutes.

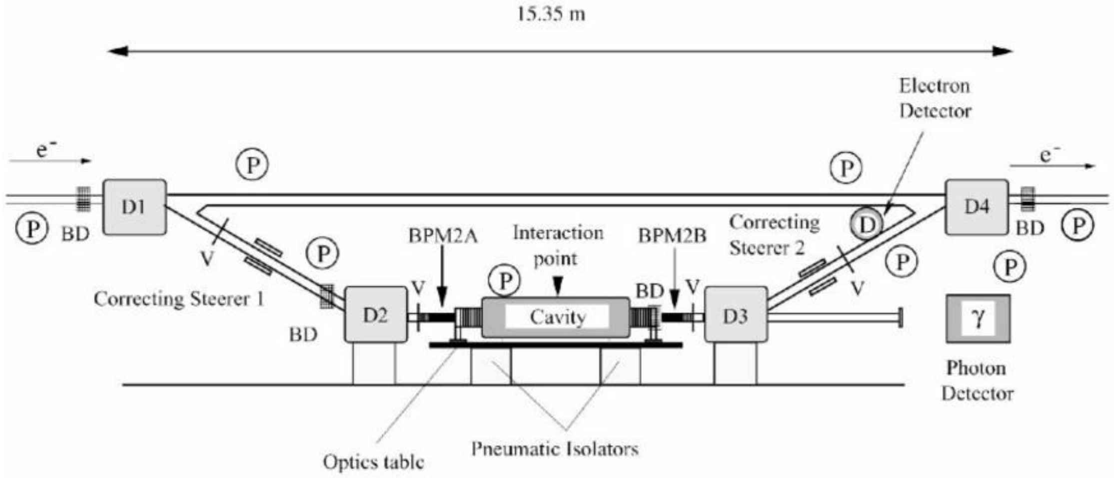

Figure 45: *Schematic of the Hall A Compton polarimeter. Figure from [46].*

The vacuum in the interaction region is at the level of few $\times 10^{-8}$ torr, a level should should keep the rate of Bremsstrahlung from residual gas to around 5 Hz/μA. The dominant source of background in the photon detector is thought to be tails of the beam halo distribution interacting with the apertures in the interaction region. In contrast, for the electron detector the dominant background is thought to be dominated by energy tail or position halo of the primary beam since electrons from aperture scattering would presumably not cleanly transit the third dipole. When well-tuned, the background rates in the photon and electron detectors have been seen to be roughly similar: around < 100 Hz/μA in recent use. At 11 GeV, with the presently planned 3 kW green cavity, the Compton-scattered rates will be approximately 2 kHz/μA and the asymmetry will range from 32% to -7% over the energy spectrum. If backgrounds remain small compared to this rate, statistical precision of 0.4% would be possible in less than 5 minutes, depending on the specific detection and analysis approach which is used.

Electrons are detected in a set of 4 planes of silicon microstrips located just before the 4th dipole. Each microstrip instruments 192 strips with a pitch of 240 μm. Custom readout electronics pre-amplify and discriminate signals from the microstrips, implement a simple tracking algorithm to reduce non-directional backgrounds, and count hits in each strip over specified integration gates corresponding to the helicity pattern of the electron beam. Presently, this system is operating at low efficiency with poor signal size for a minimum ionizing track compared to environmental noise on individual strips. The baseline upgrade would complete work on this system to achieve high efficiency and high signal-over-noise for the microstrip readout.

The calorimeter for detecting scattered photons lies about 7 meters downstream of the interaction point. The strong forward boost of scattered photons leads to a tightly collimated photon beam (< 1 mrad), so the calorimeter size relates only to energy resolution through shower loss. The photon calorimeter is a GSO crystal scintillator of 6 cm diameter and 15 cm length, with a single photomultiplier tube. The PMT signal is split between two parallel data acquisitions: one with a fast-counting, buffered ADC self-triggered on pulses from the photon detector, and the other utilizing a 250MHz flash ADC to record individual pulses and also to integrate the total signal over periods corresponding to the helicity pattern of the electron beam. The detector response function can be calibrated with coincidence electron/photon triggered data, using the electron detector to tag the photon energy. This response function is convoluted with the expected asymmetry distribution to estimate the analyzing power as a function of calorimeter signal for analysis of photon counting data. In an alternative approach, the Hall A Compton now uses an integrating measurement of the photon signal [47]. In such a system, calibration is greatly simplified, and very high systematic precision can be reached only by bounding non-linearities in the the average detector response as a function of photon energies. At 11 GeV, it is reasonable to expect that both analyses will be employed.

F.2 Upgrades Beyond the Baseline

There are several issues which must be addressed, related either to operation at the higher beam energy or to the very high level of precision which is proposed.

- The electron beam halo is expected to be significantly worse at 11 GeV as synchroton light emission in the recirculation arcs will increase the momentum-normalized beam emittance. For Compton polarimetry, the halo is directly responsible for the dominant backgrounds in electron detection, while scattering of beam halo from narrow apertures in the interaction region are thought to dominate backgrounds in photon detection.

- Measurement of the laser polarization must be performed with very high precision.

- The total power of synchrotron radiation emitted by the beam in the chicane arcs will be more than an order of magnitude higher compared to Compton measurements in the 6 GeV era, and this radiation spectrum will be significantly stiffer. Dilution from this radiation will complicate photon and electron detection.

- Photon detection must provide a well-characterized and linear response for photons in an energy range from about 3 GeV to low energies and over a large variation in signal rate, while being radiation hard and also insensitive or shielded from the synchrotron radiation power.

These issues are addressed by several modifications which go beyond the baseline 11 GeV upgrade.

- **Laser system** A larger crossing angle for the photon and electron beams will allow larger electron beam apertures, and reduce backgrounds in the photon detector. This increase in crossing angle comes at the expense of lower luminosity, so the high-precision upgrade must also maintain scattering rates through more laser power.

  We propose a crossing angle of 3.8 degrees, with a high power infrared (1064 nm) resonant optical cavity operating at up to 10 kW of stored power. A system for measuring laser polarization inside this cavity (although not while locked to resonance) must be developed and used, along with a thorough study of all optical components, to improve knowledge of the photon polarization.

  An alternative laser system is also under consideration, centered around a short-pulse laser with a repetition frequency matched to the RF electron beam bunching, with an optional low-gain resonant cavity. Such a system may provide advantages for the determination of laser polarization and for controlling background contributions.

- **Chicane Modification** The synchrotron light power on the photon detector can be significantly reduced by installing shims to increase the fringe fields of the chicane dipole magnets in the interaction region. This would also soften the synchrotron energy spectrum, making shielding more effective. More complete magnetic studies and details of the magnetic design are underway.

- **Photon Detector** The photon detection system used for recent running will be replaced with a detector better matched to the Compton photon energy spectrum for 11 GeV operation. While energy resolution and detection speed are important for response studies, the likelihood is that polarization measurements will utilize the integrating technique which have recently achieved precision better than 1%. To support these detection technique, the detector selection will place a premium on linear response over a range of photon energies and average signal levels.

These upgrades are described in more detail below. Table 16 summarizes the goals for various contributions to systematic uncertainty, to be achieved with the upgrades beyond baseline.

F.2.1 Laser System

As described above, in the current configuration of the Hall A Compton, the electron beam interacts with green (532 nm) light in a resonant optical cavity at a crossing angle of about 1.4°. After accounting for the length of the optical cavity (about 85 cm) and the finite size of the cavity mirror, it is necessary to enforce an aperture on the electron beam of ± 5 mm. It is thought that this narrow aperture is the dominant source of background for 6 GeV running. At higher energies synchrotron light emission in the recirculation arcs will increase the beam emittance and presumably lead to significantly larger backgrounds from this aperture scattering. In present use of the Compton polarimeter, frequent beam tuning is required to maintain operation with the signal-over-background > 10. A large background signal is often associated with large fluctuations in the background, with significant variations over the period of time in the laser on/off cycle used to measure backgrounds. This injects significant noise, and potentially significant systematic error through instability in the phototube under large variations in rate. For this reason, it is desirable to keep the signal-over-background ratio large.

Relative error (%)	electron	photon
Position asymmetries*	-	-
E$_{Beam}$ and λ_{Laser}*	0.03	0.03
Radiative Corrections*	0.05	0.05
Laser polarization*	0.20	0.20
Background / Deadtime / Pileup	0.20	0.20
Analyzing power Calibration / Detector Linearity	0.25	0.35
Total:	0.38	0.45

Table 16: *Goals for systematic errors for the Hall A Compton polarimeter at 11 GeV. Topics marked* * *are a common systematic error between the photon and electron analyses, while the other are largely independent between the detector systems.*

The aperture can be widened only by increasing the laser crossing angle which would also lower the luminosity. Although the baseline upgrade plans do not make provision for changing this crossing angle, operability at 11 GeV may require larger apertures. With a larger crossing angle, an increased luminosity would also be required to maintain the high signal-over-background and high statistical precision. While simulations are being performed which are meant to predict properties of the 12 GeV beam, it is unlikely that any of these will be known to be reliable before the higher energy beam is available in 2013. Without reliable predictions of background levels, it is prudent to design for both large crossing angle and large luminosity.

At a finite crossing angle α, the luminosity for a continuous-wave electron and photon beam with intersecting waists is given by:

$$\mathcal{L} \approx \frac{1+\cos\alpha}{\sqrt{2\pi}} \frac{I_e P_\gamma}{e k_0 c} \frac{1}{\sqrt{\sigma_e^2+\sigma_\gamma^2}} \frac{1}{\sin\alpha} \tag{12}$$

The present baseline upgrade, with 3000 W stored power at 532 nm and a crossing angle of 1.4 degrees, should provide a rate of approximately 2 kHz/μA. Increasing the crossing angle to 3.6° would allow a ± 0.5 inch aperture, which is the maximum aperture allowed by the 1" beam pipe diameter in the bore of the existing dipole magnets in the chicane. At this crossing angle, the baseline cavity would provide a Compton rate of 730 Hz/μA.

We propose the use of an infrared cavity storing 10 kW of optical power at 1064 nm. The primary disadvantages are the reductions in analyzing power and softening of the energy spectrum (17% analyzing power and 1.8 GeV maximum photon energy for IR, compared to 32% and 3 GeV for 532 nm). While the cross-section is very similar between the two photon energies, at 1064 nm there are twice as many photons per unit energy. In addition, significantly more injection laser power is available in the IR, for which a fiber amplifier can be used and frequency doubling is not required. The existing cavity design and drive lasers are likely capable of providing 10 kW of stored IR power; this could be increased further with additional improvements of the cavity mechanics and feedback electronics. This proposed system would provide a rate of 3.5 kHz/μA while allowing the full ± 0.5" electron beam aperture.

Control of systematic error also requires precise determination of the polarization of the photon target. This has proved to be the dominant systematic error contribution in recent Hall A Compton polarimeter measurements, in part because the use of a high-gain resonant cavity significantly complicates this determination. In a resonant cavity, the polarization state of the stored light con not be directly measured without destroying the resonance. For the present Hall A polarimeter, the laser polarization is inferred from measurements of the light that transmits through the cavity. A transfer function, relating the polarization of light in the Compton Interaction Region (CIP) to the polarization measured in the transmitted beam outside the vacuum vessel, is determined from measurements with an un-locked cavity. The highly-reflective cavity mirrors must be removed for these measurement, and the cavity must be open to air, which implies a relaxation of any pressure-induced birefringence of the vacuum entrance and exit windows. Contributions from birefringence in the cavity mirror substrate and stress on the vacuum windows can be characterized separately, but as a practical matter these are difficult to determine with high precision. For the Hall A polarimeter, previous studies have quoted the uncertainty in beam polarization to be 0.35%, but in recent operation the uncertainty could not be bounded to smaller than 0.7%.

In order to facilitate measurement of the laser polarization with a robust 0.2% error bar, it will be necessary to supplement the transfer function techniques with an *in situ* measure of the polarization. Modifications to the interaction region will be made to allow an insertable, vacuum-compatible analysis assembly for measurements of the beam in the CIP. The power level for such measurements will necessarily be very low, as the highly reflective mirrors of the cavity will attenuate incident light, but such a measurement would include all effects of birefringence and depolarization in the injection of optical power into the cavity.

F.2.2 Alternative Laser System

An alternative laser system is also under consideration, based on the use of a short-pulse RF laser synchronized the the electron bunch frequency. Such a system would concentrate laser power on the electron bunches, in effect creating an electron-photon collider. For a laser with narrow pulse structure (≈ 10 ps) and repetition frequency sub-harmonic to the electron beam ($f_{laser} = 499$ MHz / n with integer n), the the ratio of luminosity for the same average power goes as:

$$\frac{\mathcal{L}_{pulsed}}{\mathcal{L}_{CW}} \approx \frac{c}{f_{beam}\sqrt{2\pi}} \frac{1}{\sqrt{\sigma_{e,z}^2 + \sigma_{\gamma,z}^2 + \frac{1}{\sin^2 \alpha/2}\left(\sigma_e^2 + \sigma_\gamma^2\right)}}. \tag{13}$$

Here f_{beam} is the electron repetition rate and $\sigma_{e,z}$ ($\sigma_{\gamma,z}$) is the longitudinal size of the electron (laser) pulse. For the parameters relevant to the proposed system, this corresponds to an enhancement of luminosity per unit power of between 20-50. Commercially available mode-locked laser systems has been identified providing 45 W at 1064 nm, with 100 MHz repetition rates and 10 ps pulse widths. Assuming an average injected power of 30 W at the 3.6° crossing angle, this pulsed laser would provide 330 Hz/μA with a single-pass beam, that is, without the resonant optical cavity required by the default design.

Although the relatively low rates would be expected to be a disadvantage, it may turn out to be operable depending on the characteristics of the 11 GeV electron beam. The statistical precision (0.4% in about 15 minutes) would be sufficient. Such a system provides important advantages. Without the optical cavity, the determination of laser polarization is simplified. In the case of a resonant cavity, if the *in situ* laser polarization measurements, made in the cavity with the leakage through the input mirror, do not match the polarization inferred from measurements outside the cavity using the transfer function, then this could represent any of a number of effects which are each difficult to study. For example, thermal effects might modify the birefringence of elements and change the transfer function or the polarization state of injected light; or a small birefringence in the mirror dielectric layers can compound into a significant change in a beam which is stored through many bounces. Neither effect would exist for the single-pass system, as the laser beam used for polarimetry, rather than a low-power injection beam, is directly measured *in situ*.

There are other advantages as well. Locking and unlocking a cavity takes time, so to maintain a high duty factor for a cavity system the locked and un-locked periods used to determine backgrounds are long (≈ 1 minute) relative to the fluctuations in the background. On the other hand, a laser can be turned off (or deflected to a dump) quickly, so background measurements for such a single pass system could take place quickly, potentially providing superior control of background fluctuations even if the signal-over-background ratio is smaller. Similarly, without the requirement to maintain the delicate balance of signal levels necessary to robustly lock a high-gain cavity, systematic studies varying laser power or position would be potentially simplified.

Should be rate from such a system be unmanageably small relative to backgrounds, it could be roughly doubled using a "butterfly" cavity to recirculate the exit beam through the interaction point. A more powerful option would be a hybrid system in which the RF pulses are stored in a resonant optical cavity. A moderate cavity gain ≈ 20 would double the Compton signal rate compared to the 10 kW, gain ≈ 3000 CW default design. At such a low gain, the cavity lock would be relatively easy to acquire, potentially enabling more rapid background measurements than the high-gain system. The polarization measurement would also likely be simpler than for a high-gain cavity system, as the injection beam in the interaction region would still be similar to the beam stored through relatively few resonant reflections.

Such a cavity would require the dual resonance condition of being both an integral number of optical and RF wavelengths. This is not a particularly difficult condition to maintain. The injection laser must be mode-locked to ensure coherence between pulses. Locking mode-locked lasers to Fabry-Perot cavities has been actively pursued over the last decade in development studies for Compton-based X-ray sources [48, 49] and for a polarized positron source for the ILC [50, 51], with significant technical success beyond the requirements for this proposed system.

The above discussion demonstrates the utility and technical feasibility of the alternative proposal for a 10 ps pulse length, 100 MHz, 1064 nm laser system operating either as an injection laser for a gain ≈ 20 resonant cavity or as a 30 W single-pass system. The default CW alternative utilizes laser systems purchased for 6 GeV operations; this alternative proposal would require new investment for acquisition of the injection laser and high-power optics. If studies of the polarization in the high-gain, CW cavity system can not demonstrate control of the laser polarization at the level of 0.2%, this alternative system would be necessary.

F.2.3 Chicane Magnet Modification

At 11 GeV, significant synchrotron radiation is emitted when the electron beam is bent in a magnetic field. This radiation load will be a significant background in the photon detector and can overwhelm the signal from Compton scattering. Figure 46 shows the energy spectrum of synchrotron light attenuated by lead shielding between 1–5 mm, depending on the beam energy. On the left, the spectrum for 11 GeV with unmodified magnets is compared to calculations for the recent runs of HAPPEX-III (3 GeV) and PV-DIS (6 GeV). On the right, the energy spectrum ("Fringe 2") is shown when iron extensions, 15 cm in length, are added to the dipole magnets in order to provide an extended region of reduced field. This reduced magnetic field produces synchrotron light with at lower energy and with reduced intensity, while bending the electron beam trajectory out of line with the photon detector. With this modification, the bending strength of the magnet remains the same but the synchrotron light radiated into the detector is reduced by a factor of 10^4, to a level comparable to HAPPEX-III. The field was modeled using 2-D field calculation software *Poisson*, both for the magnet as it exists and for the proposed shim.

Further development of this promising idea will continue, including more detailed simulations of the synchrotron radiation interactions in the lead shielding, improved magnetic modeling, and mechanical design to incorporate the magnetic shims into the beamline design.

F.2.4 Photon Detection

The specific calorimeter to be employed is not yet determined. The present calorimeter is a GSO crystal scintillator, which has excellent light yield suitable for measurements at low energies. The crystal is too small to contain most showers at higher energies, and a new calorimeter will be required for precision

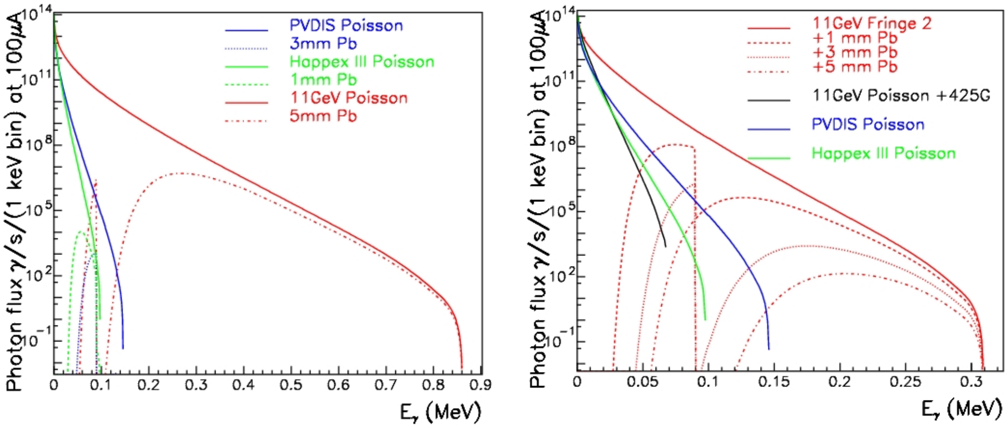

Figure 46: *Energy spectrum of synchrotron radiation penetrating lead shielding of thickness listed. Plot on left shows unmodified chicane magnets, plot on right shows energy spectrum for proposed magnetic shims which reduce the field for the bend radiating into the Compton photon detector acceptance. Note the different horizontal scales between the plots.*

measurements at 11 GeV. In the past, Hall A has used an undoped lead tungstate ($PbWO_4$) array. This may be suitable for 11 GeV operation; the relatively low light yield for $PbWO_4$ is not an issue for higher photon energies of the proposed measurements or for the integrating measurements, and the high speed of this material reduces pile-up issues in counting measurements. Designs for multi-layer sampling calorimeters, using either scintillation or Cherenkov light, will also be considered.

F.3 Systematic Uncertainties

While the proposed system should assure operability and sufficient statistical precision at 11 GeV, the challenge will be achieving an absolute measurement of beam polarization with a precision of 0.4%. Table 16 summarizes the goals for various contributions to systematic uncertainty. The first four rows list sources of uncertainty uncertainty which are highly or completely correlated between the electron and photon analyses. The measurement of laser polarization is the most challenging of these correlated systematic errors and represents the largest improvement over what has been recently achieved.

Other potential systematic errors arise in detector readout or calibration and are mostly or entirely decorrelated between the analyses. Each of these separate categories of potential systematic uncertainty: correlated, electron-only, and photon-only, will be discussed in the following sections.

F.3.1 Sources of Correlated Error

Any error associated with the Compton scattering process will be a common source of systematic error between the electron- and photon-detector analyses. One example lies in the energy normalization of the scattering process. The analyzing power is a function of both electron energy and photon energy, so these must be precisely determined. The photon wavelength will be determined to better than 0.1 nm and the electron energy to 0.05%, which leads to an uncertainty at the level of 0.03%. A similarly small uncertainty will come from radiative corrections, which are calculable [52] with high precision and will contribute at the level of 10^{-3}.

Helicity-correlated changes in luminosity of the laser/electron interaction point can introduce a false asymmetry. Various causes of luminosity variation must be considered, such as electron beam intensity, beam motion or spot-size variation. The control of helicity-correlated beam asymmetries is now a standard technology at Jefferson Lab, and typically achievable results (few part per million intensity, 10's of nanometers beam motion, $< 10^{-3}$ spot size changes) will suitably constrain the electron-photon crossing luminosity variations. Another possible source of false asymmetry would be electronics pickup of the helicity signal, which could potentially impact an integrating photon analysis. However, the demands of the primary experiment for isolation of the helicity signal exceed those for polarimetry by several orders of magnitude. In addition, the laser polarization reversal provides an additional cancellation for asymmetries correlated to the electron beam helicity. Potential effects must be carefully considered, but with due effort, false asymmetries will be a negligible source of uncertainty in this measurement.

A more significant source of error comes from the uncertainty in the photon polarization. As described above, at present the laser polarization at the interaction point is measured directly by opening the vacuum chamber and inserting optical diagnostics. The cavity mirrors must be removed for this measurement, as they do not transmit sufficient light for measurement when the cavity is not resonant. The effect of the mirrors is deduced from the change in the transfer function through the cavity, after the mirrors are replaced and the cavity locked. Based on studies of the mirror substrates conducted during R&D for the original Hall A Compton project, this effect is typically expected to be less than 0.1%. The polarization of the transmitted beam is monitored during production running.

In the present Hall A polarimeter, the uncertainty in beam polarization has been estimated to be as small as 0.35%, but recent determinations have been less certain, at the level of 0.7%. This result can be improved, notably by using an insertable stage in the interaction region of the aligned cavity to measure the polarization of the injection beam *in situ*. The effect of vacuum windows will be studied as well as stability of the polarization transfer when the cavity is locked to resonance. The circular polarization of the laser must be determined with a precision of not less than 0.2%, which represents an error in the combined linear polarization and depolarization of not worse than 4.5%. If studies do not demonstrate that this can be achieved with the high-gain cavity, alternative laser systems will need to be developed.

F.3.2 Systematic Errors for the Electron Detector

The electron detector is composed of 4 planes of silicon microstrips normal to the electron beam and adjustable in position to approach close to the primary beam. Electrons which have given up energy to a scattering process are separated from the primary beam by the third chicane dipole, and the energy of a detected electron is implied by the distance of the track from the primary beam with a resolution of about 0.15%/mm. Models of the chicane magnets are used to calculate the function of energy vs. distance. The use of multiple planes is used to reduce electronics noise in the strips and non-directional backgrounds by triggering on tracks which are restricted to very small angles relative to the beam. The trigger can be adjusted for the range of track angles and number of planes used in the track, including a single plane trigger. The efficiency of individual strips can also be measured using data from the multiple planes.

The silicon detector may also be sensitive to synchrotron light, and while the detector is not in line-of-sight to synchrotron emission in dipole 3, synchrotron photons rescattered in the beam pipe may be a problem. In addition, the electron detector or its support hardware will be line-of-sight to the synchrotron emission in the first chicane dipole, through the straight-through beam pipe. It will likely be necessary to use an insertable synchrotron guard upstream of the electron detector.

The cross-section and asymmetry vs Compton photon energy is plotted in Figure 47 for 11 GeV electron beam and a 1064 nm laser. The Compton edge (the kinematic endpoint of the Compton energy spectrum) is observed in the electron detector and used to calibrate the distance of the detector from the primary beam. In addition, the asymmetry as a function of photon energy k exhibits a zero crossing. Determining the location of this asymmetry zero crossing (0xing) provides a second absolute energy calibration point, so together the Compton edge and 0xing can be used to calibrate two parameters: the detector location relative to the beam

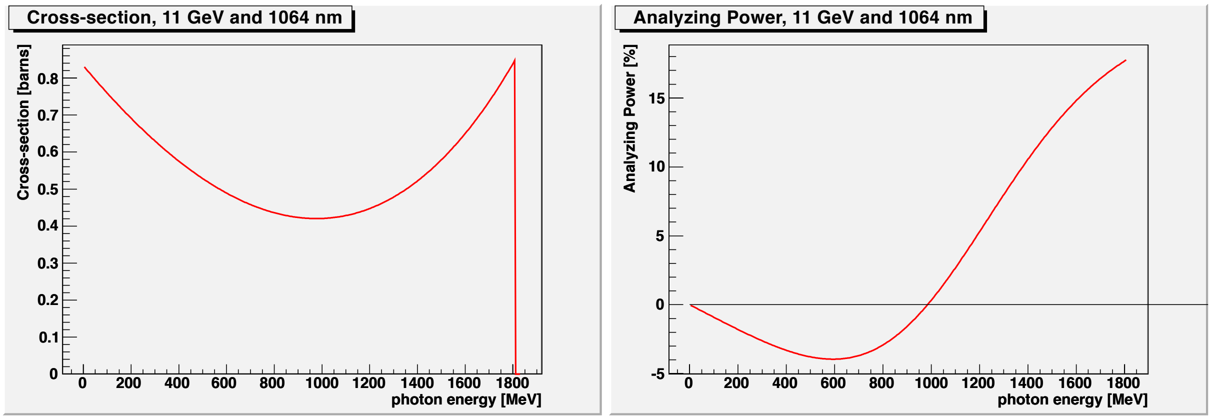

Figure 47: *The cross-section and asymmetry plotted versus Compton scattered photon energy for the Hall A polarimeter at 11 GeV.*

and the strength of the magnetic field in dipole 3. In this way, survey results and magnetic field maps serve as a cross-check to a beam-based self-calibration of the Compton energy spectrum.

In operation at low beam energies, this process was challenging as the 0xing was close to the primary beam: for HAPPEX-II, the separation was approximately 5 mm. At this proximity, background rates were extremely sensitive to beam tuning in the injector and RF phase corrections in the linacs, presumably due to energy tails. At 11 GeV with the IR laser, the 0xing will be around 15mm from the primary beam, which should allow for more robust operation.

The analyzing power for the measured electron distribution can be very accurately determined with use of this self-calibration, with the systematic error dependent upon the specifics of the analysis approach.

- *Integration* The polarization can be determined as a counting asymmetry for the sum of all strips from the Compton edge to the zero crossing.

  Here the error in the analyzing power for a perfect detector would be related to the uncertainty in the energy thresholds. Since there is no Compton-scatter rate above the Compton edge, there is no error introduced for the low-electron energy cut-off. For a high electron-energy cut-off at the 0xing, the asymmetry is near zero so the error in determining the location of the 0xing would act essentially the same as an error in the background dilution.

  The determination of the 0xing will introduce an additional source of statistical noise in the determination of the electron polarization, but a systematic bias in the 0xing is would be a dangerous systematic error. Small variations in the beam deflection by the third dipole and in the location of the electron detector will reduce systematic bias from the discretization of the data into the silicon strips. Errors in the magnetic model or detector non-uniformities could possibly create a bias. It should be possible to avoid a systematic bias to a level better than 10% of the width of a strip, which would correspond to a 0.16% effect.

  An error in the 0-Xing location could also arise from an experimental false asymmetry. The slope near the 0-Xing is such that a 0.1% false asymmetry would result in reduction of 0.7% the estimated analyzing power (and so a +0.7% in the measured electron polarization). The false asymmetry would directly represent an error in the electron polarization of about 1%, so this effect increases the sensitivity to false asymmetry by factor of about 1.7. False asymmetries associated with helicity-correlated position or intensity changes are expected to be negligible, even with this enhancement.

Probably the most significant uncertainty in the analyzing power will arise from efficiency variations among the silicon strips. Strip-by-strip efficiencies can be calculated by comparing track-hit efficiency between the 4 planes of the silicon detector. Inefficiency in previous detector systems has been low, at the level of 1% or less. Comparison of results from the 4 detector planes will provide a cross-check on this effect, since local variations in asymmetries should be independent between the planes. Significant variations in the location of the detector relative to the primary beam, which would also help control this effect, should be possible, depending on the observed beam halo.

- *Asymmetry Fit* The polarization can also be found from the shape of the asymmetry over all strips between the Compton edge and the zero crossing. This technique would share the small uncertainties on determination of the 0-Xing with the integration technique. However, it would not be sensitive to strip-to-strip variations in efficiency, which is the dominant sensitivity for the integration technique.

  This fit would be sensitive to knowledge of the magnetic field uniformity. Deviations from the expected shape would introduce systematic uncertainty. Such an an effect may be bounded by studying fit χ^2 or systematic bias of residuals to the fit. In addition, the region of the fit may be varied to test the robustness of the technique. The preliminary Qweak analysis using this technique has been found to be remarkably robust. With a broad array of possible self-consistency checks, this analysis is likely to provide the most precise analyzing power calibration.

- *Single Strip* The statistical power of the last, single silicon strip at the Compton edge will be significant, capable of 0.5% measurements on time-scales of around 20 minutes. The rate of change of the asymmetry in this region is only 0.74% / mm. Locating this strip, relative to Compton edge, to a little better than half its own width should provide a robust 0.5% accuracy on the analyzing power. This technique would have a greatly reduced sensitivity to the 0-Xing location, dispersion variations or strip efficiency.

  Similarly, if the electron detector can be moved close to the primary beam the asymmetry minimum (about 9 mm from the primary beam) could be detected. Here the asymmetry is not changing with position, so there is minimal calibration error in selecting a strip in this minimum. The statistical power is much lower in this region, with a single strip requiring 12 hours to achieve 0.5% precision.

Cross-checks between techniques, each of which have very different sensitivities to possible sources of error, should provide convincing evidence that the system is well understood. Given these considerations, it seems likely that the calibration of the electron detector will be understood at the level of 0.3% or better.

Regardless of the analysis, contributions from deadtime and pileup will need to be understood. The fast-counting DAQ can take very high rates with low deadtimes, and deterministic deadtime intervals are enforced in readout and acquisition electronics stages. With data rates in the range of 200 kHz, DAQ deadtime corrections may be potentially non-negligible, although rates in individual strips will be reduced by segmentation to only a few kHz. A dedicated effort will be necessary to control the dead-time and pile-up systematic errors at the level of 0.2%. The high statistical power of the measurement is of significant use here; high precision studies can be performed to benchmark models of the readout system against changes the laser power or the parameters of the triggering (preamp levels, logical gate lengths, coincidence levels, etc).

Backgrounds are also a potential but small source of systematic uncertainty. Backgrounds are studied with the laser cavity unlocked, allowing both the background level and asymmetry to be well determined. However, high backgrounds could impact the systematic error due to deadtime or pile-up corrections. There is also the possibility of backgrounds from Compton-scattered electrons, which can produce delta rays when scattering in the detector or in its shielding. These tracks can themselves be sufficiently forward-going to be counted, thus changing the analyzing power as a function of energy. Simulation will be used to avoid such problems, and studies of track distribution and electron-tagged photon energy spectra can be used to identify such effects in the data.

Finally, it is clear, but worth stating, that beam properties at 11 GeV will be important for the precision of the electron detector analysis. If simulations reveal that halo backgrounds for the electron detector are likely to be unacceptably near 15 mm from the primary beam, then this places the 0xing self-calibration in question. In this case, a laser option utilizing green light would be an alternative. Using 532 nm light in a cavity would put the zero-crossing about 27 mm from the primary beam. It is also worth noting that the single-strip analyses would be also improved with the higher resolution and larger asymmetries (and larger distances from the primary beam) available from a green laser.

F.4 Systematic Errors for the Photon Detector

The precise determination of the analyzing power as a function of energy is more difficult for the photon calorimeter than for the electron detector due to the width, and shape, of the detector response function. In order to fit the asymmetry as a function of detected photon energy, the analyzing power must be calculated as a convolution of the response function with the theoretical analyzing power curve. The response function shape and energy calibration can be studied using the photon tagging through coincidence triggers with the electron detector.

In general, determining the effect of a low-energy threshold on the analyzing power depends sensitively on the shape of the response function; at low energies this is a major source of uncertainty. At high energies, the improved resolution and consistency of the response function shape over the range of interest should significantly reduce this problem. As noted above, the photon calorimeter will to be upgraded to better contain showers from high energy photons, with the primary objective to provide a response function which scales linearly over a broad range of energy.

The deadtime correction represents a potential systematic uncertainty. Counting in the photon detector is also sensitive to pile-up, which distorts the asymmetry distribution. Background and rate distributions will serve as inputs to simulation for corrections to the analyzing power. In the current Hall A analysis, pile-up effects are estimated at the level of 1%, and the effect can be controlled at a level better than 10% of itself.

Uncertainties related to the threshold, response function shape, absolute energy calibration, deadtime and pile-up can also be eliminated by integrating al signal, without threshold [47]. These previous problems are then replaced with a requirement on the uniformity of the average response over photon energy. Because the analyzing power integral is energy-weighted, the statistical figure-of-merit in not badly degraded by the negative asymmetry region.

The PREX experiment, with a beam energy near 1 GeV, relied on the integrating photon method for polarimetry at the level of 1% precision. Simulations of the photon response function appear to be sufficient to control the analyzing power uncertainties for those measurements. The dominant uncertainty in the asymmetry measurement arises from instability in the photomultiplier response with changing rate which introduced a systematic error through background subtraction.

At high energies, with the ability to study response function with the tagged photon beam over a large fraction of the energy range, the photon detector analyzing power normalization uncertainty in the range of 0.3% should be achievable. Characterization of the phototube response as a function of rate and pulse-size will also be important. As described above, synchroton light from the chicane magnets and Bremsstrahlung scattering from apertures in the interaction region are potential background problems that will require further study.

F.5 Summary of Compton Polarimetry

The prospects for 0.4% Compton polarimetry are excellent. This ambitious goal will require vigorous and dedicated efforts to reduce sources of systematic uncertainty. It is expected that some significant fraction of data production time wil be used for studies of the Compton polarimeter system which are not disruptive to the experiment, for example, scans of detector positions, laser power and polarization and data acquisition parameters. The scattering asymmetry at 11 GeV is relatively large, which allows precision at the level of $\sim$0.5% in less than 1 minute of data. Given this high statistical power, these studies will be an effective method for constraining many of the possible experimental systematic uncertainties.

The future use of the Hall A polarimeter at 11 GeV will be a very different situation from the recent operation. The dominant systematic errors in recent operation lay in the determination of the analyzing power and laser polarization. Operating at lower energies the asymmetries were significantly lower and therefore the statistical power was worse. In addition, the limits of systematic uncertainty had not been pushed by demands of the experiment precision.

The 0-Xing "integration" analysis was attempted for the first time for the HAPPEX-II and HAPPEX-He measurements. The situation was complicated due to the low beam energy of around 3 GeV, which not only reduced the average asymmetry but also reduced the ratio of Compton-scattered photon energies and the electron energies. At 3 GeV, the zero-crossing was about 5 mm from the primary beam, which was as close as the electron detector could get to the beam. Geometric efficiency at the edge were a significant complication in this approach. In addition, the microstrip detector was damaged and displayed low and uneven efficiency, which complicated the analysis. The estimated systematic errors for that analysis which were not associated with these efficiency issues are consistent with Table 16.

For the photon detector, the integration readout method has been successfully used, with the primary limitations being the characterization of the phototube response over the range of signal levels. And the rapid access to high statistical power, which is so powerful for cross-checking potential sources of systematic uncertainty, has never before been available to the Hall A Compton.

High-precision Compton polarimetry has also been widely applied at storage rings and colliders. Uncertainties in analyzing power determination have typically limited the precision of high-energy collider Compton photo-detectors to typically $\sim 0.8\%$. These measurements typically use the integrating photon technique for production running, since the electron beam currents are so high. However, in these measurements, photon tagging through coincidence with an electron detector is typically not available for study of the detector response function. The ability of the Hall A Compton polarimeter to perform *in situ* tagged photon calibrations will be a significant advantage.

G Møller Polarimetry

G.1 Møller Scattering

Møller polarimeters exploit the properties of the polarized Møller scattering $\vec{e^-} + \vec{e^-} \to e^- + e^-$. Its unpolarized cross section, first calculated by C. Møller [70], in the Born approximation and the ultrarelativistic limit depends on the scattering angle in c.m. $\Theta_{\rm cm}$ and the Mandelstam variable s as:

$$\frac{d\sigma_\circ}{d\Omega_{\rm cm}} = \frac{\alpha^2}{s} \cdot \frac{(4-\sin^2\Theta_{\rm cm})^2}{\sin^4\Theta_{\rm cm}}, \tag{14}$$

where α is the electomagnetic coupling constant, also presentable as $\alpha = r_e \cdot m_e$, where $r_e = 2.817 \cdot 10^{-13}$ cm is the classical electron radius. In the lab frame of the fixed target experiments, the scattering cross section at $\Theta_{\rm cm} = 90^\circ$ doesn not depend on s:

$$\frac{d\sigma_\circ}{d\Omega}\left(\Theta_{\rm cm} = 90^\circ\right) \approx 178\ {\rm mb/ster}. \tag{15}$$

The polarized cross section depends on the beam and target polarizations $\mathcal{P}_{beam}$ and $\mathcal{P}_{target}$ as:

$$\frac{d\sigma}{d\Omega_{\rm cm}} = \frac{d\sigma_\circ}{d\Omega_{\rm cm}} \cdot (1 + \sum_{i=X,Y,Z}(A^M_{ii} \cdot \mathcal{P}_{targ\ i} \cdot \mathcal{P}_{beam\ i})), \tag{16}$$

where $i = X, Y, Z$ defines the projections of the polarizations. The analyzing power A^M, calculated in the same limits as Eq. 14 [71, 72], depends on the angle $\Theta_{\rm cm}$ and does not depend on s. Assuming that the beam direction is along the Z-axis and that the scattering happens in the ZX plane:

$$A^M_{ZZ} = -\frac{\sin^2\Theta_{\rm cm}\cdot(7+\cos^2\Theta_{\rm cm})}{(3+\cos^2\Theta_{\rm cm})^2}, A^M_{XX} = -\frac{\sin^4\Theta_{\rm cm}}{(3+\cos^2\Theta_{\rm cm})^2}, A^M_{YY} = -A^M_{XX} \tag{17}$$

At $\Theta_{\rm cm} = 90^o$ the analyzing power has its maximum $A^M_{ZZ\ max} = 7/9$. A beam transverse polarization in the scattering plane also leads to an asymmetry, though the analyzing power is lower: $A^M_{XX\ max} = A^M_{ZZ}/7$. The main purpose of the polarimeter is to measure the longitudinal component of the beam polarization.

G.2 Ways to Higher Accuracy

In this section we discuss the limitations to the accuracy of of Møller polarimeters, and we introduce our plans to achieve a higher accuracy including the recent progress in Hall A during PREX and DVCS in 2010.

Polarized Møller scattering (described in Section G.1) is a convenient process for measuring the beam polarization. Its counting rate does not depend on the energy, the analyzing power is high (about 80%) and neither depends on the energy, nor changes considerably in the range of the polarimeter acceptance, and two electrons with high energies in the final state make it easy to detect their coincidence and reduce the background to negligible values.

For the polarized electron target only ferromagnetic foils have been used so far [53, 54, 55, 56, 57, 58, 39]. In fully magnetized iron, for instance, about 2.1 electrons from the d-shell are polarized and the average electron polarization is about 8%. This value can not be calculated from first principles, but has to be derived from the measured magnetization. Most polarimeters have used foils tilted at an angle of about 20° to the beam and magnetized by external fields of 10-30 mT directed along the beam. In these conditions the magnetization is not fully saturated and depends on many parameters, including the foil annealing and history. The magnetization can be measured, typically with an accuracy of 2-3%.

In 2010, just prior to PREX the Hall A Møller polarimeter was upgraded as follows: 1) The "brute force" polarization of the target foil using a strong (3T) magnetic field, as has been done in Hall C [59, 39]. The strong longitudinal field saturates the magnetiziation of the foil. In addition, the target has a smaller thickness and lower heating; 2) A segmented aperture detector to accommodate the higher rates; and 3) A new fast DAQ based on Flash ADCs to handle the higher rates with smaller deadtime and to provide more information about the events such as pileup. Table 8 in section 4.2.2 shows the systematic errors achieved by the end of 2010, which totaled 0.86%.

The magnetization of the foils in the strong longitudinal field has not been measured, but is taken from published data on the properties of bulk iron, which claims an accuracy of $\sim 0.1\%$. In both cases, the orbital contributions to the magnetization of about 5% can be evaluated and subtracted using the magneto-mechanical factor, measured by other dedicated experiments [60]. With strong external fields of 3-4 T several additional correction of about 0.5% have to be made to compensate for extra orbital momenta and other complex effects. These corrections are temperature dependent.

The magnetization of ferromagnetic materials depends on the temperature. The beam heats up the foil and the temperature in the beam area is difficult to measure or calculate accurately. This limits the average beam current to 2-3 μA, much lower than the current of > 50 μA to be used in the experiment. Using different beam regimes for experiment and polarimetry may become a source of systematic errors, difficult to evaluate. A possible way to solve this problem is to use a fast "kicker" magnet to move the beam back and forth across the edge of a foil located at a distance of about 1 mm from the regular beam position [61].

Another source of errors is the medium-weight atom used for the target. Møller scattering off electrons from the inner atomic shells has a distorted energy-angle correlation for the secondary electrons, with respect to scattering off electrons from the outer shells. A difference of the polarimeter acceptance for these two classes of events is the source of a systematic bias (the so-called Levchuk effect [62]), typically of about 1-5%. This effect forbids using a tight optical collimation of the secondary particles, which would otherwise be favored for background suppression. In most cases, the background is dominated by electron-nucleus scattering and contains one electron in the final state. It can be efficiently suppressed by detecting both secondary Møller electrons in coincidence, however this background typically doubles the detectors' counting rate.

The counting rate depends on the target thickness and the apparatus acceptance. The acceptance should not be too small, because of the Levchuk effect. The associated dead time is typically not negligible and can be an additional source of systematic errors.

The list of systematic errors for the JLab Møller polarimeters in Hall A and Hall C are presented in Table 8 in section 4.2.2.

Although it is possible to reduce considerably the systematic error of the foil polarization by using a very high magnetization field [39], it is difficult to reduce the other errors, in particular the one associated with the beam current limitations. Also, it is difficult to arrange for continuous measurements since even the thinnest foil used (~ 1 μm) strongly affects the electron beam.

To avoid the shortcomings of the ferromagnetic targets, a proposal was developed to use polarized atomic hydrogen gas, stored in an ultra-cold magnetic trap, as the target [40, 41, 63]. Such a target of practically 100% polarized electrons would remove the errors associated with the ferromagnetic targets, namely knowledge of the target polarization and the Levchuk effect. The other errors as the analyzing power uncertainty and the dead time can be strongly suppressed. Such a target is thin enough to be used continuously with the experiment. The expected systematic error (see Table 8) is below 0.5%. A 1% statistical accuracy can be achieved in less than 30 minutes of running. We propose to develop the novel technique of atomic hydrogen targets for Møller polarimetry. This will require a dedicated R&D project (discussed in section 7.6.2). Although the technique of hydrogen trapping is well established, there is presently no experience in passing a high intensity beam through such a trap. The technical details of this project is described in Section G.3.

For the backup solution we consider the technique, being developed for Hall C [61], which involves a polarized foil and a "kicker" magnet used to move the beam. This option is described in Section G.4. In both cases, the spectrometer for the Hall A Møller polarimeter (see Fig. 48) does not need to be changed.

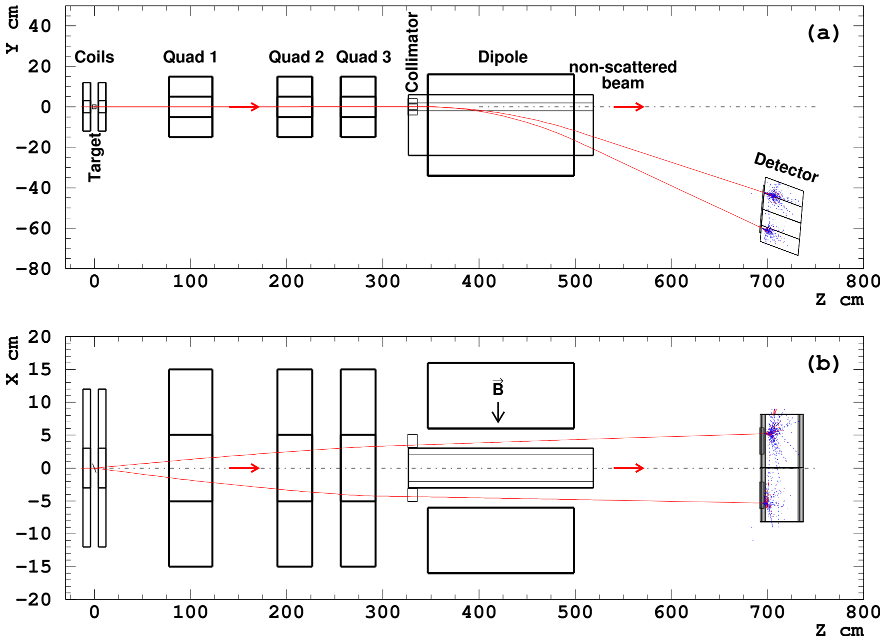

Figure 48: *The layout of the Hall A Møller polarimeter in it present configuration. The planned upgrade for 12 GeV includes lifting of the detector box to compensate for a smaller deflection in the dipole.*

G.3 Atomic Hydrogen Target

A detailed description of the project can be found in [63]. Here, a summary is presented.

G.3.1 Hydrogen Atom in Magnetic Field

The magnetic field B_S and the hyperfine interaction split the ground state of hydrogen into four states with different energies. The low energy states are $|a\rangle = |\downarrow\Uparrow\rangle\cdot\cos\theta - |\uparrow\Downarrow\rangle\cdot\sin\theta$ and $|b\rangle = |\downarrow\Downarrow\rangle$, where the first and second (crossed) arrows in the brackets indicate the electron and proton spin projections on the magnetic field direction. As far as the electron spin is concerned, state $|b\rangle$ is pure, while state $|a\rangle$ is a superposition. The mixing angle θ depends on the magnetic field B_S and temperature T: $tan\ 2\theta \approx 0.05\ \mathrm{T}/B_S$. At B_S =8 T and $T = 0.3$ K the mixing factor is small: $\sin\theta \approx 0.003$. State $|b\rangle$ is 100% polarized. State $|a\rangle$ is polarized in the same direction as $|b\rangle$ and its polarization differs from unity by $\sim 10^{-5}$. In addition, there are high-energy states $|c\rangle$and $|d\rangle$which have the wrong polarization, but which get rapidly rejected from the field region (explained more below).

G.3.2 Storage Cell

In a magnetic field gradient, a force $-\nabla(\vec{\mu_H}\vec{B})$, where μ_H is the atom's magnetic moment, separates the lower and the higher energy states. The lower energy states are pulled into the stronger field, while the higher energy states are repelled from the stronger field. The 0.3 K cylindrical storage cell, made usually of pure copper, is located in the bore of a superconducting ~8 T solenoid. The polarized hydrogen, consisting of the low energy states, is confined along the cell axis by the magnetic field gradient, and laterally by the wall of the cell (Fig 49).

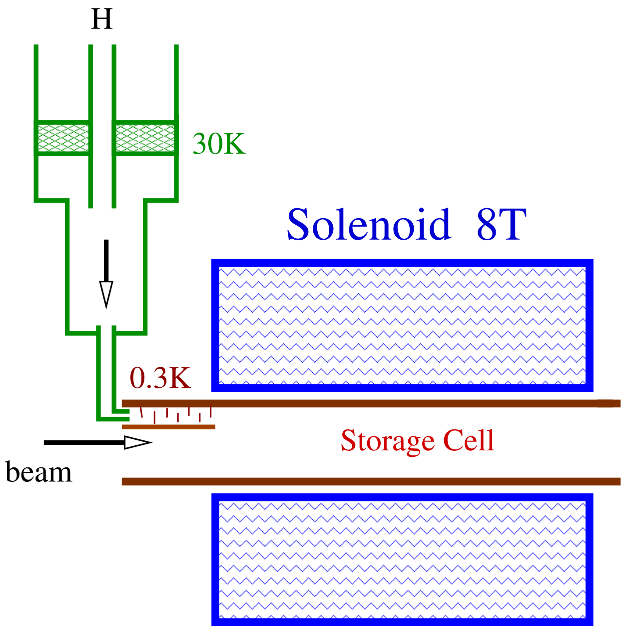

Figure 49: *A sketch of the storage cell.*

At the point of statistical equilibrium, the state population, p follows the Boltzmann distribution:

$$p \propto \exp\left(\mu_e B/kT\right), \tag{18}$$

where μ_e is the electron's magnetic moment ($\mu_H \approx \mu_e$) and $k = k_B$ is the Boltzmann constant. The cell is mainly populated with states $|a\rangle$ and $|b\rangle$, with an admixture of states $|c\rangle$ and $|d\rangle$ of $\exp\left(-2\mu_e B/kT\right) \approx 3 \cdot 10^{-16}$. In the absence of other processes, states $|a\rangle$ and $|b\rangle$ are populated nearly equally. The gas is practically 100% polarized, a small ($\sim 10^{-5}$) oppositely polarized contribution comes from the $|\uparrow\Downarrow\rangle$ component of state $|a\rangle$.

The atomic hydrogen density is limited mainly by the process of recombination into H_2 molecules (releasing ∼4.5 eV). The recombination rate is higher at lower temperatures. In gas, recombination by collisions of two atoms is kinematically forbidden but it is allowed in collisions of three atoms. On the walls, which play the role of a third body, there is no kinematic limitation for two atom recombination. At moderate gas densities only the surface recombination matters. In case of polarized atoms, the cross section for recombination is strongly suppressed, because two hydrogen atoms in the triplet electron spin state have no bound states. This fact leads to the possibility of reaching relatively high gas densities for polarized atoms in the traps.

A way to reduce the surface recombination on the walls of the storage cell is coating them with a thin film (∼50 nm) of superfluid ^{4}He. The helium film has a very small sticking coefficient[4] for hydrogen atoms.In contrast, hydrogen molecules in thermal equilibrium with the film are absorbed after a few collisions and are frozen in clusters on the metal surface of the trap [64].

The higher energy states are repelled from the storage cell by the magnetic field gradient and leave the cell. Outside of the helium-covered cell, the atoms promptly recombine on surfaces into hydrogen

---

[4] The sticking coefficient defines the atom's adsorption probability per a collision with a surface.

molecules which are either pumped away or are frozen on the walls. Some of the higher energy states recombine within the cell and the molecules eventually are either frozen on the helium-coated wall, or leave the cell by diffusion.

The cell is filled with atomic hydrogen from an RF dissociator. Hydrogen, at 80 K, passes through a Teflon[5] pipe to a nozzle, which is kept at ∼30 K. From the nozzle hydrogen enters into a system of helium-coated baffles, where it is cooled down to ∼0.3 K. At 30 K and above, the recombination is suppressed because of the high temperature, while at 0.3 K it is suppressed by helium coating. In the input flow, the atoms and molecules are mixed in comparable amounts, but most of the molecules are frozen out in the baffles and do not enter the cell.

The gas arrives at the region of a strong field gradient, which separates very efficiently the lower and higher atomic energy states, therefore a constant feeding of the cell does not affect the average electron polarization. This technique was first successfully applied in 1980 [65], and later a density[6] as high as $3 \cdot 10^{17}$ atoms/cm^3 was achieved [66] in a small volume. So far, the storage cell itself has not been put in a high-intensity particle beam.

For the project being discussed a normal storage cell design can be used, with the beam passing along the solenoid axis (Fig. 49). The double walls of the cylindrical copper cell form a dilution refrigerator mixing chamber. The cell is connected to the beam pipe with no separating windows. The tentative cell parameters are (similar to a working cell [67]): solenoid maximum field of $B_S = 8$ T , solenoid length of $L_S = 30$ cm, cell internal radius of $r_\circ = 2$ cm, cell length of $L_C = 35$ cm and temperature of $T = 0.3$ K. The effective length of such a target is about 20 cm. For the guideline, we will consider a gas density of $3 \cdot 10^{15}$ cm^{-3}, obtained experimentally [68], for a similar design.

G.3.3 Gas Properties

Important parameters of the target gas are the diffusion speed. At 300 mK the RMS speed of the atoms is ∼80 m/s. For these studies we used a calculated value [69] of the hydrogen atoms cross section $\sigma = 42.3 \cdot 10^{-16}$ cm^2, ignoring the difference between the spin triplet and singlet cross sections. This provided the mean free path $\ell = 0.57$ mm at density of $3 \cdot 10^{15}$ cm^{-3}.

The average time, τ_d for a "low field seeking" atom to travel to the edge of the cell, assuming its starting point is distributed according to the gas density, is[7]: $\tau_d \approx 0.7$ s. This is the cleaning time for an atom with opposite electron spin, should it emerge in the cell and if it does not recombine before. The escape time depends on the initial position of the atom, going from ~ 1 s at $z = 0$ to 0.1 s at $z = 8$ cm. The average wall collision time is about 0.5 ms.

G.3.4 Gas Lifetime in the Cell

For the moment we consider the gas behavior with no beam passing through it. Several processes lead to losses of hydrogen atoms from the cell: thermal escape through the magnetic field gradient, recombination in the volume of gas and recombination on the surface of the cell. The volume recombination can be neglected up to densities of $\sim 10^{17}$ cm^{-3} [66].

The dominant process, limiting the gas density, is the surface recombination. In order to keep the gas density constant the losses have to be compensated by constantly feeding the cell with atomic hydrogen. Our calculations, based on the theory of such cells [66], show, that a very moderate feed rate of $\Phi \sim 1 \cdot 10^{15}$ atoms/s would provide a gas density of $7 \cdot 10^{15}$ cm^{-3}.

---

[5] Teflon has a relatively small sticking coefficient for hydrogen atoms.

[6] This parameter is called concentration, but we will use the word density in the text; mass of the gas is not important here.

[7] This time was estimated using simulation, taking into account the gas density distribution along z and the repelling force in the magnetic field gradient.

This can be compared with the measurement [68] of $3 \cdot 10^{15}$ cm^{-3}. The average lifetime of a "high field seeking" atom in the cell is $\sim$1 h.

G.3.5 Unpolarized Contamination

The most important sources of unpolarized contamination in the target gas in absence of beam are:

1) hydrogen molecules: $\sim 10^{-5}$;

2) high energy atomic states $|c\rangle$ and $|d\rangle$: $\sim 10^{-5}$;

3) excited atomic states $< 10^{-10}$;

4) other gasses, like helium and the residual gas in the cell: $\sim 10^{-3}$

The contributions 1)-3) are present when the cell is filled with hydrogen. They are difficult to measure directly and we have to rely on calculations. Nevertheless, the behavior of such storage cells has been extensively studied and is well understood [66]. The general parameters, like the gas lifetime, or the gas density are predicted with an accuracy better than a factor of 3. The estimates 1)-3) are about 100 times below the level of contamination of about 0.1% which may become important for polarimetry. In contrast, the contribution 4) can be easily measured with beam by taking an empty target measurement. Atomic hydrogen can be completely removed from the cell by heating a small bolometer inside the cell, which would remove the helium coating on this element, and catalyze a fast recombination of hydrogen on its surface. However, it is important to keep this contamination below several percent in order to reduce the systematic error associated with the background subtraction.

G.3.6 Beam Impact on Storage Cell

We have considered various impacts the $\mathcal{I}_b = 100\ \mu$A CEBAF beam can inflict on the storage cell [63]. The beam consists of short bunches with $\tau = \sigma_T \approx 0.5$ ps at a $\mathcal{F} = 499$ MHz repetition rate. The beam spot has a size of about $\sigma_X \approx \sigma_Y \sim 0.1$ mm. The most important depolarization effects we found are:

A) gas depolarization by the RF electromagnetic radiation of the beam: $\sim 3 \cdot 10^{-5}$;

B) contamination from free electrons and ions: $\sim 10^{-5}$;

C) gas excitation and depolarization by the ionization losses: $\sim 10^{-5}$;

D) gas heating by ionization losses: $\sim 10^{-10}$ depolarization and a $\sim$30% density reduction.

The effects A) and B) are described below.

G.3.7 Beam RF Generated Depolarization

The electromagnetic field of the beam has a circular magnetic field component, which couples to the $|a\rangle \rightarrow |d\rangle$ and $|b\rangle \rightarrow |c\rangle$ transitions. The transition frequency depends on the value of the local magnetic field in the solenoid and for the bulk of the gas ranges from 215 to 225 GHz. The spectral density function of the magnetic field can be presented in the form of Fourier series with the characteristic frequency of $\omega_\circ = 2\pi\mathcal{F}$. The Fourier coefficients are basically the Fourier transforms of the magnetic field created by a single bunch. The bunch length is short in comparison with the typical transition frequency ($\omega_{trans}\tau \sim 0.1$). The resonance lines of the spectrum (a reflection of the 499 MHz repetition rate) populate densely the transition range (see Fig. 50). The induced transition rate depends on the gas density at a given transition frequency. This rate was calculated taking into account the beam parameters and the field map of a realistic solenoid. Provided that the field of the solenoid is fine tuned to avoid the transition resonances for the bulk of the gas in the cell (see Fig. 50), the depolarization described has the following features:

- the transition rate is proportional to $\mathcal{I}_b^2$;
- the average rate of each of the two transitions is about $0.5 \cdot 10^{-4}$ of the target density per second;
- at the center around the beam the full transition rate is about 6% of the density per second.

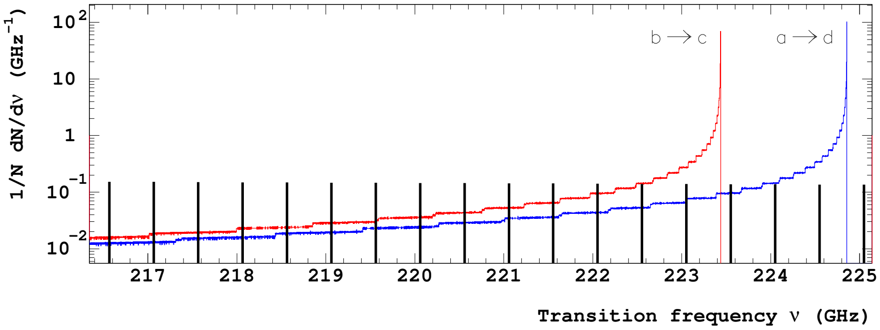

Figure 50: *Simulated spectra of the transitions on the axis of the hydrogen trap with the maximum field of 8.0 T. The density of atoms depends on the field as $exp(-\mu_e B/kT)$. The two curves show $\frac{1}{N}dN/d\nu_{ad}$ and $\frac{1}{N}dN/d\nu_{bc}$ - the relative number of atoms which can undergo $|a\rangle \rightarrow |d\rangle$ and $|b\rangle \rightarrow |c\rangle$ transitions at the given frequency, per one GHz. The resonant structure of the spectral function of the beam-induced electromagnetic field is shown as a set of vertical bars, 499 MHz apart.*

In order to estimate the average contamination we take into account that each resonance line presented in Fig. 50 corresponds to a certain value of the solenoid field and, therefore, affects the gas at a certain z. Using a realistic field map of the solenoid we obtained that the average depolarization in the beam area will be reduced to about $\sim 0.3 \cdot 10^{-4}$ by the lateral gas diffusion and by the escape of the "low field seeking" atoms from the storage cell.

In order to study experimentally the depolarization effect discussed, one can tune the solenoid magnetic field to overlap a resonance line with the transition frequency of the gas at the cell center. This would increase the transition rate by a factor of ~70.

G.3.8 Contamination by Free Electrons and Ions

The beam would ionize per second about 20% of the atoms in the cylinder around the beam spot. The charged particles would not escape the beam area due to diffusion, as the neutral atoms would do, but will follow the magnetic field lines, parallel to the beam. An elegant way to remove them is to apply a relatively weak ~1 V/cm electric field perpendicular to the beam. The charged particles will drift at a speed of $v = \vec{E} \times \vec{B}/B^2 \sim 12$ m/s perpendicular to the beam and leave the beam area in about 20 μs. This will reduce the average contamination to a 10^{-5} level.

G.3.9 Application of the Atomic Target to Møller Polarimetry

This feasibility study was done for the possible application of the target discussed to the existing Møller polarimeter in Hall A at JLab.

The beam polarization at JLab is normally about 80%, at beam currents below 100 μA. Scaling the results of the existing polarimeter to the hydrogen target discussed we estimated that at 30 μA a 1% statistical accuracy will be achieved in about 30 min. This is an acceptable time, in particular if the measurements are done in parallel with the main experiment.

There is no obvious way to measure directly the polarization of the hydrogen atoms in the beam area. The contamination from the residual gas is measurable. The rest relies on calculations. All calculations show that the polarization is nearly 100%, with a possible contamination of $<$0.01%, coming from several contributions. The impact of the most important of these contributions can be studied, at least their upper limits, by deliberately increasing the effect. For example, the beam RF induced transitions can be increased by a factor of $\sim$70, by fine tuning of the solenoid magnetic field. The contribution from the charged particles in the beam area can be varied by a factor up to $\sim 10^4$, by changing the cleaning electric field.

The systematic errors, associated with the present Hall A polarimeter, when added in quadrature give a total systematic error of about 3%. Scaling these errors to the design with the hydrogen target reduces the total error to about 0.3%. If we scale the accuracy of the Hall C polarimeter (see Table 8), the projected total error would be better than 0.2%. There is no doubt that achieving such an accuracy is a major challenge and will require re-evaluation of the error budget for including smaller effects, so far neglected. However, the technique described has a potential to deliver an accuracy of 0.4% required for the experiment proposed.

G.4 Møller Polarimeter in Hall C

The Hall C Møller polarimeter was originally designed and constructed by the Basel Nuclear Physics group to overcome what has been to date, the most significant systematic uncertainty in the Møller polarimetry technique - namely the knowledge of the polarization of the "target" used in the measurement of the double–spin Møller scattering asymmetry. In 2010, the concepts were applied in Hall A, as described in section G.2 and table 8.

As described in Sec. G, the Hall C Møller polarimeter makes use of a pure iron foil, typically 1 to 10 μm thick oriented perpendicular to the electron beam direction and brute–force polarized out of plane using a 3–4 T superconducting solenoid. In principle, such a target results in kowledge of the target polarization to better than 0.25% [73].

One drawback of this saturated foil target, however, is the need to avoid significant temperature changes due to beam heating. As seen in Fig. 51, a temperature increase of 60–70 degrees C results in a reduction of the target polarization of $\approx 1\%$. The need to avoid such temperature changes typically limits the beam current used in Møller measurements to 1-2μA. Higher currents can and have been used in Hall C using a circular raster of $\approx$1 mm radius to limit beam heating. However, even with a large raster, practical beam currents are limited to 20 μA before beam heating becomes significant. This is still well away from the nominal current ($> 50\mu$A) to be used in this experiment. In principle, measurements using the Kerr effect may be used to monitor the relative target polarization, but this requires that the laser impinge on the iron foil at precisely the same point (and perhaps with the same shape) as the electron beam.

One can attempt to mitigate foil heating effects using a fast beam kicker system combined with a thin strip or wire target. In this system, the electron beam is kicked at some low duty cycle onto or across a pure iron target. The beam is only impinging on the target for timescales on the order of μs such that the target does not have much opportunity to heat up, while the relatively long time between kicks allows the target to cool.

A series of tests have been performed in Hall C with two prototype kicker magnets and two different target configurations [61]. Initial tests were performed with 25 μm diameter iron wires replacing the iron foil at the Møller target. While these tests were moderately successful, it was found that the high instantaneous current combined with the relatively thick profile of the target lead to a high rate of random coincidences. The second generation prototype target replaced the iron wires with a 1 μm strip target, reducing the instantaneous rate.

Results from the second generation tests are shown in Fig. 52. In this case, the duration of the beam "kick" was about 10 μs at a repetition rate between 5 and 10 kHz. Data were taken using the kicker and iron strip target up to 40 μA. In general, the results were consistent with there being no effect from target

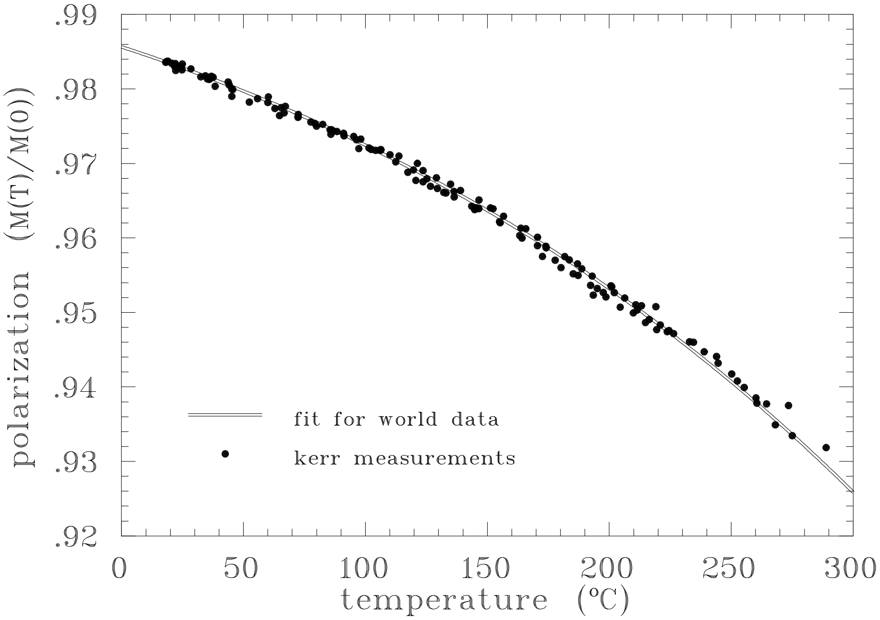

Figure 51: *Relative magnetization vs. temperature for a pure iron foil driven to magnetic saturation (from [73]). The iron foil used in the Hall C Møller polarimeter is normally at room temperature with no active cooling.*

heating, albeit with relatively low precision. Problems with beam transport precluded the use of higher beam currents. Finally, it should be noted that apparent instabilities with either the source or Hall C Møller polarimeter itself (found by taking "calibration" data at 2 μA from a normal iron foil) made it difficult to conclude that target heating effects were completely avoided.

An improved kicker magnet capable of scanning the beam across an iron strip target in $\approx 1\mu$s has been constructed and was installed for the QWeak experiment in Hall C. In addition to the improved kick speed, the new kicker has the ability to hold the electron beam at a nearly fixed position on the foil (see Fig. 53) such that one can gate off the datataking during periods in which the beam is in transit. We estimate that allowing the beam to dwell on the iron strip target for periods of $\approx 1\mu$s with a frequency of 2.5 kHZ will keep target depolarization due to heating effects to the 1% level. Unfortunately, larger than expected backgrounds and beam steering issues have prevented the testing of this kicker magnet during the QWeak running thus far. Both of the above should problems should be smaller at the higher energy of the Møller experiment, so should not preclude its potential use.

Application of a similar technique for this experiment requires consideration of several issues. First, the fastest kicker magnet developed for Hall C will only operate up to a beam energy of $\approx$2 GeV. Given that the currents will likely be about a factor of three smaller, a slower kicker is likely acceptable. For example, a kick duration of 8 μs is sufficiently fast to keep target depolarization effects at the 1% level. Space in the beamline would need to be found, preferably far from the Møller target region to maximize deflection for a given $\int \vec{B} \cdot d\vec{l}$. Also, it should be noted that for the Hall C system, up to 1% effects are deemed acceptable, assuming that we can estimate the correction to the target polarization with a precision of something like 50% of the size of the effect. Since the goal here is 0.5% polarimetry, the allowed effects from target heating will need to be smaller. A kicker capable of kick durations of $\approx$4 μs yielding 1-2 mm deflection at the Møller target at 11 GeV would need to be designed and built.

Another option that one can use to at least partially overcome the low current constraint imposed by the

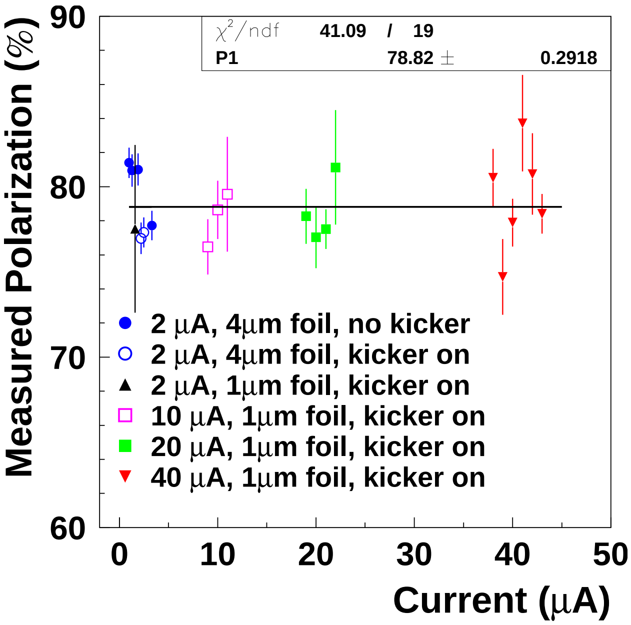

Figure 52: *Results of polarization measurements taken in Hall C using the second generation kicker magnet impinging on a 1 μm thick iron foil strip target. Measurements were made at beam currents up to 40 μA. Higher currents were not accessible to due to beam losses from the deflected electron beam. Control measurements at 2 μA were not stable, so these measurements cannot be used to prove 1% precision at high currents.*

use of saturated pure iron foils is to operate the electron beam in a lower duty-cycle mode, such that the average current impinging on the target is relatively small, while the instantaneous current of a particular electron beam pulse is much larger. In particular, one can operate the polarized electron source in a so-called "beat-frequency" mode in which the source laser frequency is slightly different from that of the RF (chopper) system used to clean-up, and potentially adjust the intensity of the electron beam pulses for each hall independently. When an appropriate laser frequency is chosen, the majority of the electron pulses are out of phase with the opening of the acceptance defining slit in the chopper, and only the Nth pulse, where $N = f_{cavity}/(f_{cavity} - f_{laser})$, is accepted.

This technique was first tested in 2006, when it was used in a variety of applications in Halls A and C [74]. A test using the Hall C Møller polarimeter was performed with the laser frequency set to

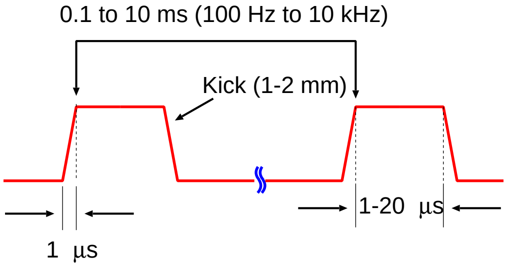

Figure 53: *Schematic of the operating mode of the new kicker magnet to be installed for Q_{Weak}. The beam is kicked 1-2 mm in about 1 μs and remains stationary on the Møller target for 1 to several μs.*

467.8125 MHz (RF cavity frequency 499 MHz) such that the nominal current of the electron beam reaching Hall C was reduced by a factor of 16 due to the loss of bunches on the aperture defining slits.

The results of the Hall C test are shown in Figure 54, where three scenarios are illustrated. The bottom plot shows the electron beam polarization as measured with the beam current being reduced using the photocathode laser power. In this case, the current from the photocathode is the same as the current arriving in Hall C. In the middle plot, high current ($\approx 60\ \mu$A) is generated from the photocathode, but the electron beam current is reduced to a few μ A using the chopper slit. In this case, the edges of the electron beam pulse are thrown away, so one is potentially sensitive to any changes of polarization across the electron beam pulse duration. The top plot shows the polarization as measured using the beat-frequency technique. In this case, the current from the photocathode was reduced by a factor of 16, such that measurements made at an average current of $\approx 3\ \mu$A in Hall C corresponded to a current of about 48 μA at the source. In this particular test, all measurements agreed very well, regardless of beam current, or technique used to reduce current sent to the hall.

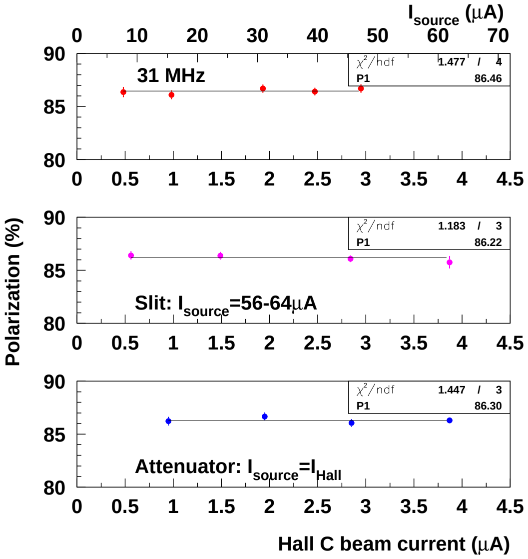

Figure 54: Results of 2006 electron source beat-frequency mode tests. The bottom plot shows the polarization measurements with the beam current controlled using the laser power directly; in the middle plot, the current was reduced using the chopper slit (high current from the photocathode); the top plot shows the current reduced using the beat-frequency technique described in the text.

Use of this beat-frequency mode allows measurements of the beam polarization in a mode that mimics high current running at the source, without any modification of the electron beam pulse itself. Use of this technique could be easily implemented for the Møller experiment at 11 GeV.

References

[1] P. L. Anthony *et al.* [SLAC E158 Collaboration], Phys. Rev. Lett. **95**, 081601 (2005) [arXiv:hep-ex/0504049].

[2] Nuclear Science Advisory Committee Long Range Planning Document (2007): http://www.sc.doe.gov/np/nsac/nsac.html

[3] Ya.B. Zel'dovich, Sov. Phys. JETP **94**, 262 (1959).

[4] E. Derman and W. J. Marciano, Annals Phys. **121**, 147 (1979).

[5] A. Czarnecki and W. J. Marciano, Phys. Rev. D **53**, 1066 (1996) [arXiv:hep-ph/9507420].

[6] A. Czarnecki and W. J. Marciano, Int. J. Mod. Phys. A **15**, 2365 (2000) [arXiv:hep-ph/0003049].

[7] J. Erler and M. J. Ramsey-Musolf, Phys. Rev. D **72**, 073003 (2005) [arXiv:hep-ph/0409169].

[8] A. Aleksejevs, S. Barkanova, A. Ilyichev and V. Zykunov, Phys. Rev. D **82**, 093013 (2010) [arXiv:1008.3355 [hep-ph]].

[9] E. Eichten, K. D. Lane and M. E. Peskin, Phys. Rev. Lett. **50**, 811 (1983).

[10] M. J. Ramsey-Musolf, Phys. Rev. C **60**, 015501 (1999) [arXiv:hep-ph/9903264].

[11] W. F. Chang, J. N. Ng and J. M. S. Wu, Phys. Rev. D **79**, 055016 (2009) [arXiv:0901.0613 [hep-ph]].

[12] A. Kurylov, M. J. Ramsey-Musolf and S. Su, Phys. Rev. D **68**, 035008 (2003) [arXiv:hep-ph/0303026].

[13] M. J. Ramsey-Musolf and S. Su, Phys. Rept. **456**, 1 (2008) [arXiv:hep-ph/0612057].

[14] J. Erler and P. Langacker, Phys. Lett. B **456**, 68 (1999) [arXiv:hep-ph/9903476].

[15] F. Petriello and S. Quackenbush, Phys. Rev. D **77**, 115004 (2008) [arXiv:0801.4389 [hep-ph]].

[16] Y. Li, F. Petriello and S. Quackenbush, Phys. Rev. D **80**, 055018 (2009) [arXiv:0906.4132 [hep-ph]].

[17] J. Erler, P. Langacker, S. Munir and E. Rojas, arXiv:1108.0685v1 [hep-ph].

[18] J. Erler, Nucl. Phys. B **586**, 73 (2000) [arXiv:hep-ph/0006051].

[19] D. Suematsu and Y. Yamagishi, Int. J. Mod. Phys. A **10**, 4521 (1995) [arXiv:hep-ph/9411239].

[20] M. Cvetic and P. Langacker, Phys. Rev. D **54**, 3570 (1996) [arXiv:hep-ph/9511378].

[21] J. E. Kim and H. P. Nilles, Phys. Lett. B **138**, 150 (1984).

[22] V. Cirigliano, A. Kurylov, M. J. Ramsey-Musolf and P. Vogel, Phys. Rev. D **70**, 075007 (2004) [arXiv:hep-ph/0404233].

[23] G. P. Zeller *et al.* [NuTeV Collaboration], Phys. Rev. Lett. **88**, 091802 (2002) [Erratum-ibid. **90**, 239902 (2003)] [arXiv:hep-ex/0110059].

[24] C. Amsler *et al.* [Particle Data Group], Phys. Lett. B **667**, 1 (2008).

[25] R. Barate *et al.* [LEP Working Group for Higgs boson searches and ALEPH Collaboration and and], Phys. Lett. B **565**, 61 (2003) [arXiv:hep-ex/0306033].

[26] T. Aaltonen *et al.* [CDF and D0 Collaboration], arXiv:1103.3233 [hep-ex].

[27] [ALEPH Collaboration and DELPHI Collaboration and L3 Collaboration and OPAL Collaboration and SLD Collaboration and LEP Electroweak Working Group and SLD Electroweak Group and SLD Heavy Flavour Group], Phys. Rept. **427**, 257 (2006) [arXiv:hep-ex/0509008].

[28] W. J. Marciano, AIP Conf. Proc. **870**, 236 (2006).

[29] P. A. Souder *et al.*, Phys. Rev. Lett. **65**, 694 (1990).

[30] D. T. Spayde *et al.* [SAMPLE Collaboration], Phys. Lett. B **583**, 79 (2004) [arXiv:nucl-ex/0312016].

[31] A. Acha *et al.* [HAPPEX collaboration], Phys. Rev. Lett. **98**, 032301 (2007) [arXiv:nucl-ex/0609002].

[32] The Lead Radius Experiment PREX, E06002, K. Kumar, R. Michaels, P. Souder, G. Urciuoli spokespersons, http://hallaweb.jlab.org/parity/prex/ .

[33] The Qweak Experiment, http://www.jlab.org/Hall-C/Qweak/index.html, , R. Carlini Principal Investigator.

[34] C. Y. Prescott *et al.*, Phys. Lett. B **77**, 347 (1978).

[35] M. Gericke, “Excess Noise as a Function of Detector Thickness”, September 1, 2005, a Qweak technical note available at http://qweak.jlab.org/doc-public/ShowDocument?docid=532 .

[36] R.S. Hicks *et al.*, “Flux Profile Scanners for Scattered High-Energy Electrons”, NIM **A553** (2005), pp 470-482.

[37] K. D. Paschke, Eur. Phys. J. A **32**, 549 (2007).

[38] K. Abe *et al.* [SLD Collaboration], Phys. Rev. Lett. **84**, 5945 (2000) [arXiv:hep-ex/0004026].

[39] M. Hauger *et al.*, “A high-precision polarimeter,” *Nucl. Instrum. Meth.*, vol. A462, pp. 382–392, 2001, nucl-ex/9910013.

[40] E. Chudakov and V. Luppov, “Møller polarimetry with atomic hydrogen targets,” *IEEE Trans. Nucl. Sci.*, vol. 51, pp. 1533–1540, 2004.

[41] E. Chudakov and V. Luppov, “Moeller polarimetry with atomic hydrogen targets,” *Eur. Phys. J.*, vol. A24S2, pp. 123–126, 2005.

[42] E. G. Brentari et al., 1965, *Boiling Heat Transfer for Oxygen, Nitrogen, Hidrogen, and Helium*, National Bureau of Standards, TN 317

[43] S. D. Covrig et al., 2005, *The cryogenic target for the G0 experiment at Jefferson Lab*, Nucl. Instr. and Meth. **A 551**, 218-235

[44] J. Gao et al., 2003, *A liquid hydrogen target for the precision measurement of the weak mixing angle in Møller scattering at SLAC*, Nucl. Instr. and Meth. **A 498**, 90-100

[45] S. Agostinelli *et al.* [GEANT4 Collaboration], Nucl. Instrum. Meth. A **506**, 250 (2003).

[46] N. Falletto *et al*, “Compton scattering off polarized electrons with a high finesse Fabry-Perot cavity at JLab,”, *”Nucl. Instrum. Meth.”*, A459, 212-425, 2001.

[47] M. Friend *et al*, “Upgraded photon calorimeter with integrating readout for Hall A Compton Polarimeter at Jefferson Lab”, [arXiv:1108.3116 [physics.ins-det]].

[48] R.J. Loewen, “A compact light source: Design and technical feasibility study of a laser-electron storage ring X-ray source,” SLAC-R-0632 (2003).

[49] S. Miyoshi *et al.*, Photon generation by laser-Compton scattering at the KEK-ATF, NIM A623 (2010) 576.

[50] A. Variola *et al.*, The LAL Compton Program,, NIM A608 (2009) S83.

[51] V. Brisson *et al.*, High finesse Fabry-Perot cavities in the picosecond regime, NIM A608 (2009) S75.

[52] A. Denner and S. Dittmaier, “Complete o() QED cor- rections to polarized Compton scattering”, Nucl. Phys. B **540** 58 (1999).

[53] P. S. Cooper *et al.*, “Polarized electron Electron Scattering at GeV Energies,” *Phys. Rev. Lett.*, vol. 34, p. 1589, 1975.

[54] B. Wagner *et al.*, “A Møller polarimeter for CW and pulsed intermediate-energy electron beams,” *Nucl. Instrum. Meth.*, vol. A294, pp. 541–548, 1990.

[55] J. Arrington *et al.*, “A Variable energy Møller polarimeter at the MIT Bates Linear Accelerator Center,” *Nucl. Instrum. Meth.*, vol. A311, pp. 39–48, 1992.

[56] K. B. Beard *et al.*, “Measurement of the polarization of a pulsed electron beam with a Møller polarimeter in the coincidence mode,” *Nucl. Instrum. Meth.*, vol. A361, pp. 46–52, 1995.

[57] H. R. Band, G. Mitchell, R. Prepost, and T. Wright, “A Møller polarimeter for high energy electron beams,” *Nucl. Instrum. Meth.*, vol. A400, pp. 24–33, 1997.

[58] A. V. Glamazdin *et al.*, “Electron beam Moeller polarimeter at JLAB Hall A,” *Fizika*, vol. B8, pp. 91–95, 1999, hep-ex/9912063.

[59] P. Steiner, A. Feltham, I. Sick, M. Zeier, and B. Zihlmann, “A high-rate coincidence Møller polarimeter,” *Nucl. Instrum. Meth.*, vol. A419, pp. 105–120, 1998.

[60] G. G. Scott, “Review of gyromagnetic ratio experiments,” *Rev. Mod. Phys.*, vol. 34, pp. 102–109, Jan 1962.

[61] D. Gaskell, D. G. Meekins, and C. Yan, “New methods for precision Møller polarimetry,” *Eur. Phys. J.*, vol. A32, pp. 561–564, 2007.

[62] L. G. Levchuk, “The Intraatomic motion of bound electrons as a possible source of a systematic error in electron beam polarization measurements by means of a Møller polarimeter,” *Nucl. Instrum. Meth.*, vol. A345, pp. 496–499, 1994.

[63] E. Chudakov and V. Luppov, “Møller polarimetry with atomic hydrogen targets,” tech. rep., JLab, 2005. `http://www.jlab.org/~gen/hyd/loi_3.pdf`.

[64] I. F. Silvera, “Ultimate fate of a gas of atomic hydrogen in a liquid-helium chamber: Recombination and burial,” *Phys. Rev. B*, vol. 29, pp. 3899–3904, Apr 1984.

[65] I. F. Silvera and J. T. M. Walraven, “Stabilization of atomic hydrogen at low temperature,” *Phys. Rev. Lett.*, vol. 44, pp. 164–168, Jan 1980.

[66] I. F. Silvera and J. T. M. Walraven, “Spin polarized atomic hydrogen,” *Progress in Low Temperature Physics, vol. X*, pp. 139–370, 1986.

[67] T. Roser *et al.*, “Microwave driven extraction of stabilized spin polarized atomic hydrogen,” *Nucl. Instrum. Meth.*, vol. A301, pp. 42–46, 1991.

[68] M. Mertig, V. G. Luppov, T. Roser, and B. Vuaridel, “Continuous density measurement of atomic hydrogen by means of a bolometer,” *Rev. Sci. Instrum.*, vol. 62, pp. 251–252, 1991.

[69] M. D. Miller and L. H. Nosanow, “Possible ”new” quantum systems. ii. properties of the isotopes of spin-aligned hydrogen,” *Phys. Rev. B*, vol. 15, pp. 4376–4385, May 1977.

[70] C. Møller, “Zur Theorie des Durchgangs schneller Elektronen durch Materie,” *Annalen der Physik*, vol. 406, pp. 531–585, 1932.

[71] A. A. Kresnin and L. N. Rosentsveig, “Polarization asymmetry of møller scattering,” *Soviet JETP*, vol. 5, pp. 288–292, 1957.

[72] A. M. Bincer, “Scattering of longitudinally polarized fermions,” *Phys. Rev.*, vol. 107, pp. 1434–1438, Sep 1957.

[73] L. V. de Bever, J. Jourdan, M. Loppacher, S. Robinson, I. Sick and J. Zhao, “A target for precise Mller polarimetry,” *Nucl. Instrum. Meth.*, vol. A400, pp. 379–386, 1997.

[74] M. Poelker, J. Grames, J. Hansknecht, R. Kazimi, J. Musson, Phys. Rev. ST Accel. Beams **10**, 053502 (2007).